

Universidade Estadual Paulista “Júlio de Mesquita Filho”
Faculdade de Engenharia de Ilha Solteira
Campus de Ilha Solteira

Vander Teixeira Prado

Ultrasonic non-destructive testing of plate-like structures using
piezoelectric array transducers

Portuguese title: Ensaio não-destrutivo por ultrassom de estruturas tipo placa utilizando arrays de
transdutores piezelétricos

Ilha Solteira
2014

Vander Teixeira Prado

Ultrasonic non-destructive testing of plate-like structures using piezoelectric array transducers

Portuguese title: Ensaaios não-destrutivos por ultrassom de estruturas tipo placa utilizando arrays de transdutores piezelétricos

Doctorate thesis submitted to Faculdade de Engenharia de Ilha Solteira - UNESP to obtain the Ph.D. grade in Electrical Engineering.

Area: Automation.

Tese apresentada à Faculdade de Engenharia de Ilha Solteira - UNESP para obtenção do título de Doutor em Engenharia Elétrica.

Área: Automação.

Professor Ricardo Tokio Higuti

Orientador

Dr. Oscar Martinez-Graullera

Co-orientador

Instituto de Tecnologías Físicas y de la Información Torres Quevedo (ITEFI)

Consejo Superior de Investigaciones Científicas (CSIC)

Ilha Solteira

2014

FICHA CATALOGRÁFICA

Desenvolvido pelo Serviço Técnico de Biblioteca e Documentação

P896e Prado, Vander Teixeira.
Ensaio não-destrutivo por ultrassom de estruturas tipo placa utilizando arrays de transdutores piezoelétricos / Vander Teixeira Prado. -- Ilha Solteira: [s.n.], 2014
124 f. : il.

Tese (doutorado) - Universidade Estadual Paulista. Faculdade de Engenharia de Ilha Solteira. Área de conhecimento: Automação, 2014

Orientador: Ricardo Tokio Higuti
Co-orientador: Oscar Martinez-Graullera
Inclui bibliografia

1. Ultrassom. 2. Ensaio não-destrutivo. 3. Arrays. 4. Imagem. 5. Defeitos.



CERTIFICADO DE APROVAÇÃO

TÍTULO: Ensaios não-destrutivos por ultrassom de estruturas tipo placa utilizando arrays de transdutores piezelétricos

AUTOR: VANDER TEIXEIRA PRADO

ORIENTADOR: Prof. Dr. RICARDO TOKIO HIGUTI

CO-ORIENTADOR: Prof. Dr. OSCAR MARTINEZ-GRAULLERA

Aprovado como parte das exigências para obtenção do Título de DOUTOR EM ENGENHARIA ELÉTRICA, Área: AUTOMAÇÃO, pela Comissão Examinadora:

Prof. Dr. RICARDO TOKIO HIGUTI
Departamento de Engenharia Elétrica / Faculdade de Engenharia de Ilha Solteira

Prof. Dr. CLAUDIO KITANO
Departamento de Engenharia Elétrica / Faculdade de Engenharia de Ilha Solteira

Prof. Dr. SAMUEL DA SILVA
Departamento de Engenharia Mecânica / Faculdade de Engenharia de Ilha Solteira

Prof. Dr. NICOLÁS LEONARDO PÉREZ ALVAREZ
Centro Universitario de Paysandú / Universidad de La República

Prof. Dr. JOAQUIM MIGUEL MAIA
Departamento Acadêmico de Eletrônica - DAELN / Universidade Tecnológica Federal do Parana

Data da realização: 15 de setembro de 2014.

To my parents

ACKNOWLEDGEMENTS

I would like to thank God for each new day, for each new opportunity to learn.

I sincerely would like to thank my advisor, Prof. Ricardo Tokio Higuti, who has been providing invaluable guidance throughout this study with patience and effort to teach me. Thank you for believing in my potential, for keeping me motivated and for friendship.

I would like to thank all my family, especially my parents Hiram and Dercí, who always fought to give me the best conditions to strive for my goals. They are the models that I have to follow and the reason I am who I am today.

I do not mention the names of my other friends, because they are many. Some closer, others more distant, but all in one way or another contributed and were essential to this work. So, thank you my friends.

None of the work presented here would have been accomplished without the help of Prof. Cláudio Kitano and my co-advisor Dr. Óscar Martínez-Graullera.

This work was totally supported by Fundação de Amparo à Pesquisa do Estado de São Paulo (FAPESP), process 2010/02240-0, 2010/16400-0 and 2013/00330-0.

Finally, my deepest thoughts go to Nayara Maria and Ana Laura for companionship and moral learning.

“The man constantly chooses his own destiny; he may shorten or prolong his anguish indefinitely; his happiness or unhappiness depends on his will to do goodness.” Allan Kardec.

“O homem é o árbitro de sua própria sorte; pertence-lhe abreviar ou prolongar indefinidamente o seu suplício; a sua felicidade ou a sua desgraça depende da vontade que tenha de praticar o bem.” Allan Kardec.

RESUMO

Esta tese apresenta o estudo e implementação de técnicas de inspeção de estruturas delgadas tipo placa utilizando *arrays* de transdutores piezelétricos e ondas acústicas guiadas, associados a métodos de formação e composição de imagens. A detecção de danos em estruturas através de ondas guiadas e *arrays* de transdutores é um campo de pesquisa de grande importância, principalmente em áreas como a aeroespacial e de geração de energia, que utilizam estruturas delgadas e que exigem inspeção eficaz e completa, visando confiabilidade e segurança. O emprego de ondas acústicas guiadas permite inspecionar grandes áreas utilizando sensores sem a necessidade de realizar varreduras pela peça, de maneira não-destrutiva. Além disso, apresenta sensibilidade a diversos tipos de defeitos, como furos, corrosão, variação de espessura e defeitos superficiais. São estudados aspectos de propagação de ondas, diferentes modos de propagação e dispersão, assim como as principais características dos *arrays* e a formação de imagens. Os estudos teóricos são acompanhados por simulações usando os *softwares* MATLAB e PZFlex para obtenção dos modos de propagação das ondas, interação com defeitos e diagramas de radiação dos transdutores, cujos resultados são validados por meio da análise experimental em placas de materiais isotrópicos (alumínio). Montou-se um *array* linear de transdutores piezelétricos com 16 elementos na borda de uma placa de alumínio com defeitos artificiais. Os sinais provenientes de todas as possíveis combinações dos pares transmissor-receptor foram adquiridos para a utilização de técnicas de abertura sintética. A primeira contribuição deste trabalho é um método para detecção dos defeitos baseado na fase instantânea dos sinais. Substituindo-se a informação de amplitude dos sinais pela fase instantânea (IP) no método de formação de imagem, obtém-se a imagem IP. A partir da análise desta imagem, propôs-se um limiar em função do número de sinais utilizados, o qual é aplicado à imagem IP, resultando em uma imagem binária, a qual contém a indicação se os *pixels* de uma certa região da imagem estão relacionados a defeitos ou ruído/artefatos. O limiar também pode ser utilizado para a criação de um fator de coerência a ser multiplicado pela imagem de amplitude. O método proposto aumentou a detectabilidade dos defeitos para longas distâncias, mesmo sem o conhecimento prévio da atenuação do meio de propagação. Também se obteve redução da zona morta e da falsa indicação dos defeitos. Outra contribuição é um método de composição de imagens considerando diferentes modos de propagação de ondas de Lamb (diversidade de modos). Duas imagens de abertura sintética são obtidas para cada modo, utilizando-se as informações de amplitude e fase dos sinais. O limiar proposto é aplicado à imagem IP e a informação é utilizada para selecionar uma das imagens de amplitude (após multiplicação pelo fator de coerência), para cada *pixel*, obtendo-se a imagem final. Como resultado, obtiveram-se redução da zona morta e dos artefatos e aumento do contraste, melhorando a detecção dos defeitos quando comparado ao resultado obtido utilizando-se apenas um modo de propagação.

Palavras-chave: Ultrassom. Ensaio não-destrutivo. Arrays. Imagem. Defeitos.

ABSTRACT

This thesis presents the study and implementation of non-destructive testing techniques of plate-like structures using piezoelectric array transducers and guided acoustic waves, associated with beamforming techniques and image compounding methods. Damage detection in structures using guided waves and arrays is a promising research area, especially in the aerospace and energy fields, where the use of plate-like structures demands thorough inspection due to the high safety levels of operation. Guided acoustic waves techniques can be used to inspect relatively large areas without the necessity of moving the transducers, in a non-destructive way. There are different propagation modes that can be coupled to the plate, and each mode is sensitive to specific types of defects, like notches, delamination and surface defects. Wave propagation, different propagation modes and dispersion characteristics, as well as arrays characteristics and imaging algorithms, are studied. MATLAB and PZFlex simulations are used to get further insight in the theoretical aspects, to obtain dispersion curves, interaction with defects and array response. Experimental results validate the simulations with isotropic materials (aluminum). A 16-elements piezoelectric linear array is mounted at the border of an aluminum plate with artificial defects. The signals related to all combinations of transmit-receive pairs are obtained with burst excitation, for use with synthetic aperture (SA) techniques. The first contribution of this work is a method for defect detection based on the instantaneous phase of the aperture data. The instantaneous phase (IP) image is obtained by replacing the amplitude information by the instantaneous phase in the conventional SA beamforming. From the analysis of the IP image, a threshold level is proposed in terms of the number of signals used for imaging. This threshold is applied to the IP image, resulting in a two-level image which gives a statistical indication of whether the pixels of a region in the image are related to a reflector or noise/artifacts. In order to improve contrast and reduce dead zone, the threshold can also be used to create a coherence factor to weight the amplitude images. The proposed method using the phase resulted in improvements in reflector detectability for larger distances without previous knowledge of attenuation characteristics of the propagation medium. There was also significant reduction in dead zone and false indication of defects. The second main contribution is an image compounding technique that uses the information obtained from different propagation modes of Lamb waves (Lamb mode diversity). For each mode, two synthetic aperture images are obtained from amplitude and phase information. The proposed threshold is applied to the IP image and the information is used to select one of the amplitude images (after the multiplication by the proposed coherence method), at each pixel, to obtain the compounded image. As a result, dead zone is reduced, resolution and contrast are improved, enhancing damage detection when compared to the use of only one mode.

Keywords: Ultrasound. Non-destructive testing. Arrays. Image. Defects.

LIST OF FIGURES

1	2 <i>h</i> -thickness plate with infinite dimensions in <i>x</i> and <i>y</i> directions.	40
2	Lamb wave displacements in the plate for (a) symmetric and (b) antisymmetric propagation modes.	42
3	Wavenumber dispersion curves for an aluminum plate.	46
4	Phase velocity dispersion curves for an aluminum plate.	46
5	Group velocity dispersion curves for an aluminum plate.	47
6	Out-of-plane displacement at 20 cm from the excitation point before and after the dispersion compensation for A0 and S0 mode at 100 kHz and 360 kHz, respectively.	49
7	Different wave fronts: plane wave, focused beam and beam steering.	52
8	Linear array.	52
9	Two-dimensional rectangular, square and sparse arrays.	52
10	Two point sources spaced by <i>d</i> with same intensity and phase shift between them equal to δ . Point <i>P</i> is at the far field.	53
11	Two point sources spaced by <i>d</i> , considering \vec{R}_1 and \vec{R}_2 parallel to each other.	54
12	Linear array with <i>M</i> elements spaced by <i>d</i> and a point <i>P</i> at the far field.	55
13	Linear array radiation pattern in transmission for point elements and different number of elements (<i>M</i>).	56
14	20 elements linear array radiation pattern in transmission and different pitch values.	57
15	Apodization function and radiation pattern in transmission for a 20 elements array with $\lambda/2$ -pitch using uniform, triangular and Blackman apodizations.	58
16	Linear <i>L</i> -length elements array.	59
17	Radiation pattern of a PZ26 ceramic with 0.5 mm thickness, 7 mm width and 6 mm length, attached to an aluminum plate at 360 kHz, simulated in <i>PZFlex</i>	60

18	Radiation pattern of a 20 elements array by considering point sources and the simulated ceramic, for pitches equal to $\lambda/2$ and 2λ	60
19	Coarray for 5-elements rectangular apertures.	61
20	Simulated two-way radiation pattern of a 20 elements array with pitch equal to $\lambda/2$ and λ with continuous and pulsed excitation.	62
21	Linear array with M elements, pitch d and coordinate system.	66
22	Simulated 360 kHz 4-cycles amplitude signal with a Gaussian envelope without noise.	68
23	PSFs for configuration I described in Table 1	68
24	PSFs for all configurations described in Table 1.	69
25	Phasor diagram of $v(t)$	76
26	Position and propagation vectors of a pressure wavefront generated in the point (x_e, z_e) , reflected in (x_0, z_0) and measured in (x_r, z_r)	77
27	Instantaneous phase of a simulated 360 kHz 4-cycles amplitude signal with a Gaussian envelope without noise.	78
28	IP PSF for configuration I described in Table 1: (a) 3D view of RF IP image and (b) axial view at $x = 0$ cm. Linear scales in rad.	79
29	Phasor diagram of $v(t)$ for $\text{SNR} \ll 1$	80
30	Values of ϵ and $(1 - P_E)$ as functions of the number of signals M_s	82
31	Obtained width L_x , length L_z and area of the reflector representation as functions of SNR.	83
32	Amplitude, IP and thresholded IP images considering $\text{SNR} = 10$ dB for configurations I , III and IV	84
33	Amplitude, IP and thresholded IP images for configuration I with SNR equal to 0 dB and -25 dB.	85
34	Polarity and normalized (sample by sampe) signals of a simulated 360 kHz 4-cycles amplitude signal with a Gaussian envelope without noise	86
35	Amplitude image, SCF, CFM and IPWF and weighted amplitude image for PSF configuration IV and SNR equal to -20 dB.	87
36	Block diagram of the proposed Lamb mode diversity compounding technique.	89
37	Frequency response setup.	91

38	Ceramic: thicknes, width and length.	92
39	Block diagram of the experimental setup.	92
40	(a) Experimental setup, (b) waveform generator, digital oscilloscope and multiplexer, (c) array and (d) aluminum plate.	93
41	Aluminum plate with defects.	94
42	Plate-piezoceramics frequency response.	95
43	Radiation pattern of the array for the A0 and S0 modes.	96
44	A0 amplitude images before andafter dispersion compensation.	97
45	A0 amplitude image after dispersion compensation with indications of dead zone, lateral plate ends reflections, defects, artifacts and background noise.	97
46	Echo signals received by one array element: (a) transmission, (b) echoes related to defects and edges, (c) direct propagation and (d) multiple reflections between the elements.	98
47	A0 and S0 amplitude and IP images.	99
48	Axial view for $x = -13.9$ cm passing by defects <i>II</i> and <i>III</i> of the amplitude and instantaneous phase images.	100
49	A0 and S0 amplitude images multiplied by the SCF, CFM and IPWF cohrence factors.	101
50	Defects representations before and after the multiplication of the amplitude images by the IPWF.	103
51	Compounded image. Actual defects positions and sizes are indicated in green. Scale in dB.	104
52	Defects representations before and after the image compounding procedure.	105
53	Thresholded images.	106

LIST OF TABLES

1	PSFs configuratons.	67
2	Artificial defects produced in the aluminum plate.	93
3	Defects contrasts before and after the multiplication of the amplitude images by the coherence factors. Values in dB.	101
4	Defects contrasts before and after the image compounding technique. Values in dB.	102

LIST OF ACRONYMS

1D	one-dimensional;
2D	two-dimensional;
3D	three-dimensional;
S ₀	fundamental symmetric mode or zero order symmetric mode;
A ₀	fundamental antisymmetric mode or zero order antisymmetric mode;
AWGN	additive white Gaussian noise;
CFM	Coherence Factor MAP;
DAS	delay-and-sum;
DTFT	Discrete-Time Fourier Transform;
FEM	finite element modeling;
IP	instantaneous phase;
IPWF	Instantaneous Phase Weighting Factor;
NDT	non-destructive testing;
PA	phased array;
PSF	Point Spread Function;
PZT	lead zirconate titanate;
SA	synthetic aperture;
SAFT	Synthetic Aperture Focusing Method;
SCF	Sign Coherence Factor;
SHM	Structural Health Monitoring;
SNR	signal-to-noise ratio;
TFM	Total Focusing Method.

LIST OF SYMBOLS

c_{wedge}	propagation velocity in the wedge material;
θ_{wedge}	angle of incidence;
h	plate half-thickness;
x, y, z	Cartesian coordinates;
$\hat{x}, \hat{y}, \hat{z}$	orthonormal basis of the Cartesian coordinate system;
u_i	displacement in i direction, for $i = x, y$ and z ;
∇	mathematical operator ($\nabla = \frac{\partial}{\partial x}\hat{x} + \frac{\partial}{\partial y}\hat{y} + \frac{\partial}{\partial z}\hat{z}$);
$\Phi, \vec{\Psi}$	scalar and vector potential functions;
t	time;
c_L	longitudinal propagation velocity;
c_T	shear propagation velocity;
Λ, μ	Lamé constants;
E	Young's elastic modulus;
ν	Poisson coefficient;
ρ	material density;
F, H	auxiliary functions for the development of the equations;
k	wavenumber;
ω	angular frequency;
f	frequency;
λ	wavelength;
j	imaginary unit ($j^2 = -1$);

c	phase velocity;
a_L, a_T	variables;
A, B, C, D	constants;
$T_{i_1 i_2}$	stress relating force in i_1 direction in the cross-sectional which normal is in i_2 direction, for $i_1, i_2 = x, y$ and z ;
$S_{i_1 i_2}$	strain;
c_g	group velocity;
f_c	cutoff frequency;
$g(t)$	dispersive signal;
$g_{\text{comp}}(x)$	signal after dispersion compensation;
$G_{\text{comp}}(k)$	Fourier transform of $g_{\text{comp}}(x)$;
$G(\omega)$	Fourier transform of $g(t)$;
ω_0	central frequency of operation;
$k_{\text{linear}}(\omega)$	linear wavenumber, as function of ω ;
d	pitch;
p	pressure;
A_p	pressure magnitude;
\vec{R}	position vector respect to the origin;
\vec{k}	wavenumber vector;
\hat{k}	propagation direction;
P	point;
δ	phase shift between two neighboring array elements;
p_i	pressure at point P due to the source i , for $i = 1, 2$;
\vec{R}_i	position vector respect to the source i , for $i = 1, 2$;
γ_i	angle between \vec{R}_i and P , for $i = 1, 2$;
γ	angle between array axis and \vec{R} ;

θ	complementary angle to γ ;
ω_a	variable;
M	number of elements of the array;
$w[i]$	apodization function for the i^{th} element of the array;
p_{norm}	normalized pressure;
τ_e	excitation delay for element e ;
(x_f, z_f)	coordinate of the focal point;
(x_a, z_a)	coordinate of the center of the array;
(x_e, z_e)	coordinate of the emitter e ;
(x_r, z_r)	coordinate of the receiver r ;
$w_f(x)$	array aperture considering non-point elements;
$w_i(x)$	rectangular window of width L ;
W_f	array radiation pattern considering non-point elements;
W_i	one-element radiation pattern;
W	array radiation pattern considering point elements;
W_{TR}	array radiation pattern in pulse-echo;
W_T	array radiation pattern in transmission;
W_R	array radiation pattern in reception;
w_{TR}	array aperture in pulse-echo;
w_T	array aperture in transmission;
w_R	array aperture in reception;
M_T	number of elements in the transmission array aperture;
M_R	number of elements in the reception array aperture;
$v_{er}(t)$	transmitted signal by element e and received by element r ;
$I_{\text{amp}}(x, z)$	amplitude image at (x, z) ;

$\tau_{er}(x, z)$	time of flight between the transmitter e , the point (x, z) and the receiver r ;
M_s	number of signal used for imaging;
$I_{\text{amp-envelope}}(x, z)$	envelope of the amplitude image at (x, z) ;
$\hat{v}_{er}(t)$	Hilbert transform of $v_{er}(t)$;
$\varphi_{er}(t)$	instantaneous phase of $v_{er}(t)$;
$I_\varphi(x, z)$	instantaneous phase image at (x, z) ;
$\hat{\varphi}_{er}(t)$	instantaneous phase of $\hat{v}_{er}(t)$;
$s(t)$	echo signal without noise;
$n(t)$	additive white Gaussian noise;
$\Re \{ \cdot \}$	real operator;
$S(t)$	envelope of $s(t)$;
$\phi(t)$	instantaneous phase of $s(t)$;
$N(t)$	envelope of $n(t)$;
$N_i(t)$	in-phase component of $n(t)$ respect to $s(t)$;
$N_q(t)$	quadrature component of $n(t)$ respect to $s(t)$;
$V(t)$	envelope of $v(t)$;
$\Delta\phi(t)$	difference between $\varphi(t)$ and $\phi(t)$;
$\phi_0(t)$	initial phase;
(x_0, z_0)	coordinate of the reflector;
\vec{R}_0	reflector position vector respect to the origin;
\vec{R}_e	emitter position vector respect to the origin;
\vec{R}_r	receiver position vector respect to the origin;
\vec{k}_r	wavenumber vector from the transmitter to the reflector direction;
\vec{k}_e	wavenumber vector from the reflector to the receiver direction;
$I_{\Delta\phi}(x, z)$	image at (x, z) by using $\Delta\phi(t)$ in the beamforming;

$\phi_n(t)$	instantaneous phase of noise;
$I_{\text{noise}}(x, z)$	noise instantaneous phase image at (x, z) ;
$S_i(t)$	in-phase component of $s(t)$ respect to $n(t)$;
$S_q(t)$	quadrature component of $s(t)$ respect to $n(t)$;
X	random variable;
$X_1, X_2 \dots, X_{M_s}$	sample values obtained from M_s independent observations of X ;
m_X	mean value of X ;
σ_X^2	variance of X ;
Z	sum of M_s independent observations of X ;
μ	mean value of Z ;
ϵ	threshold;
σ_0	standard deviation of an uniform distribution;
P_E	probability of error;
L_x	reflector width;
L_z	reflector length;
$I_{\text{SCF}}(x, z)$	Sign Coherence Factor at (x, z) ;
$b_{er}(t)$	algebraic sign of $v_{er}(t)$;
$I_{\text{CFM}}(x, z)$	Coherence Factor MAP at (x, z) ;
$\text{IPWF}(x, z)$	Instantaneous Phase Weighting Factor at (x, z) ;
I_A	result of multiplication between A0 mode amplitude image and A0 IPWF;
I_S	result of multiplication between S0 mode amplitude image and S0 IPWF;
I_A	compounded image.

CONTENTS

1	INTRODUCTION	31
1.1	LITERATURE REVIEW	33
1.2	OBJECTIVE	37
1.3	DEVELOPMENT OF THE STUDY	37
1.4	OUTLINE OF THESIS	37
2	LAMB WAVES	39
2.1	SYMMETRIC AND ANTISYMMETRIC MODES	40
2.2	DISPERSION CURVES	44
2.3	CUTOFF FREQUENCY	46
2.4	DISPERSION COMPENSATION	48
2.5	COMMENTS	50
3	ARRAYS	51
3.1	TYPES OF ARRAYS	51
3.2	LINEAR ARRAY	53
3.3	APODIZATION	58
3.4	FOCUSING AND BEAM STEERING	58
3.5	FINITE DIMENSIONS OF THE ELEMENTS	59
3.6	COARRAY	60
3.7	PULSED EXCITATION	61
3.8	TWO-DIMENSIONAL ARRAYS	62
3.9	COMMENTS	63
4	SYNTHETIC APERTURE IMAGES	65

4.1	POINT SPREAD FUNCTION	67
4.2	COMMENTS	70
5	PROPOSED TECHNIQUES	73
5.1	INSTANTANEOUS PHASE IMAGE	75
5.1.1	<i>Analysis of the instantaneous phase image</i>	75
5.1.2	<i>Signal-to-noise ratio analysis</i>	79
5.1.3	<i>Threshold based on the instantaneous phase image</i>	80
5.1.4	<i>Instantaneous phase weighting factor</i>	84
5.2	LAMB MODE DIVERSITY COMPOUNDING TECHNIQUE	87
5.3	COMMENTS	89
6	EXPERIMENTAL RESULTS	91
6.1	EXPERIMENTAL SETUP	91
6.2	FREQUENCY RESPONSE	94
6.3	DISPERSION COMPENSATION	96
6.4	AMPLITUDE AND INSTANTANEOUS PHASE IMAGES	96
6.5	COHERENCE FACTORS	100
6.6	LAMB MODE DIVERSITY	102
6.7	THRESHOLD	104
6.8	COMMENTS	106
7	FINAL REMARKS AND FUTURE WORK	109
7.1	DISCUSSIONS	109
7.2	CONCLUSIONS	111
7.3	CONTRIBUTIONS	112
7.4	PUBLICATIONS	112
7.5	FUTURE WORK	113
	REFERENCES	115

1 INTRODUCTION

Non-destructive testing (NDT) consists of the analysis of materials/products to check the possible existence of defects without producing changes to the object under inspection. Ultrasound is widely used in NDT in areas such as aerospace and power generation, which require thorough inspection due to the high safety levels of operation. It has several advantages: ease and speed of the test, low cost, high sensitivity, it does not produce ionizing radiation and can propagate in solids, liquids and gases. Ultrasonic NDT involves the use of bulk waves (longitudinal or shear), surface or guided waves. They can be used to detect internal and external defects such as cracks, corrosion, delamination and holes, and to measure material properties, such as elastic constants, for example.

NDT and structural health monitoring (SHM) differ in some ways. SHM is the process of implementing a damage identification strategy for the structure under analysis. This process involves the observation of a structure or mechanical system over time using periodically spaced measurements, the extraction of damage-sensitive features from these measurements and the statistical analysis of these features to determine the current state of system health (WORDEN; DULIEU-BARTON, 2004). The damage state of a system can be described as a five-step process along the lines of the process: (i) the existence, (ii) the location, (iii) the type and (iv) the severity of the damage, and (v) what is the prognosis, or how much useful life remains (FARRAR; WORDEN, 2007). Then, based on this definition, NDT can be used in SHM on steps (i) to (iv).

When one of the dimensions of the structure is smaller than the others, for example in plate-like structures, Lamb waves can propagate, which are possible due to the superposition of longitudinal and shear waves, taking into account also the boundary conditions at the interfaces (CAWLEY; ALLEYNE, 1996; CHIMENTI, 1997; LOWE; ALLEYNE; CAWLEY, 1998).

Due to the relatively low attenuation of Lamb waves, it is possible to test relatively large areas without the need to move the transducers. There are several propagation modes, with different sensitivities to each type of defect (ALLEYNE; CAWLEY, 1992a; ROSE, 2000; SU; YE; LU, 2006). Additionally, each propagation mode has its own dispersion characteristic, which should be considered for proper analysis of the results (WILCOX; CAWLEY, 2001; XU; YU; GIURGIUTIU, 2009).

Conventional ultrasonic NDT instruments generally consist of a single element working in pulse-echo or a pair of elements operating in transmit-receive mode. In this case, the inspection of the structure requires mechanical scans of the sensor across the region of interest. An array is a set of transducers geometrically arranged (linear or two-dimensional, for example),

whose acoustic beam can be electronically controlled (DRINKWATER; WILCOX, 2006). Arrays have been widely applied in NDT due to characteristics as beam control (beam focusing and deflection, lateral resolution, apodization) and speed of test, allowing to obtain images of the structure and its defects (YU; GIURGIUTIU, 2008; VELICHKO; WILCOX, 2008).

The quality of the image is mainly limited by the lateral resolution, the ratio between main and side lobe levels, and the presence of grating lobe artifacts. Lateral resolution is determined by the main lobe width, which is inversely proportional to the aperture size. The aperture size increases by increasing the number of elements (and consequently increases the number of transmission and reception channels as well as the processing cost) or the element spacing (pitch). Side lobes levels can be reduced by the use of apodization functions, in trade-off with lateral resolution.

Arrays whose elements are spaced by more than half-wavelength ($\lambda/2$) are often called sparse arrays (LOCKWOOD et al., 1996). Sparse arrays are usually associated with the presence of grating lobes, which reduce the image dynamic range and may hide some reflectors (defects) or image details (STEINBERG, 1976). In many cases as with 2D arrays for 3D imaging, the pitch is above $\lambda/2$ to keep the system complexity at reasonable levels (SCHWARTZ; STEINBERG, 1998; ULLATE et al., 2006). The use of sparse arrays is interesting as there are less elements, reducing costs in hardware, data processing and storage.

In addition to the array configuration, other factors that influence the quality of the image are: the image beamforming algorithm; the simultaneous propagation modes with different dispersion characteristics, in the case of acoustic guided waves; and signal-to-noise ratio (SNR). Some alternatives are related to the use of coherence factors (CAMACHO; PARRILLA; FRITSCH, 2009; MARTÍNEZ-GRAULLERA et al., 2011) and compounding techniques (MICHAELS; MICHAELS, 2007; HIGUTI et al., 2010).

In this work, ultrasonic NDT techniques of plate-like structures using piezoelectric array transducers and guided acoustic waves, associated with beamforming techniques are proposed, which could be applied to aircraft structures, as the wing, for example, as well as tank walls and pipes of oil industries and plates in magnetic cores of rotors and other structures in the power generation field, where the existence of a defect can result in financial and environmental risks and endanger people lives. Then, Lamb waves propagation in isotropic plate-like structures with different propagation modes and dispersion characteristics, arrays characteristics and imaging algorithms are studied. Two image techniques are proposed to improve the quality of the images and defects detection, using the instantaneous phase of signals and considering the Lamb mode diversity.

1.1 LITERATURE REVIEW

Lamb waves were first described by Horace Lamb in 1917 and defined as guided waves that propagate between two parallel free surfaces, as in plates whose stresses are null in the upper and lower surfaces (VIKTOROV, 1967), as an aircraft wing, for example. However, in practice it has been shown that they propagate even in structures with non-zero stresses on surfaces, by the contact with other media, such as in immersed plates (WU; ZHU, 1992; SCHMITT et al., 2013; GAO et al., 2014), or due to structural reinforcements in the object under inspection (DIAMANTI; SOUTIS; HODGKINSON, 2007; ZHAO et al., 2007; HIGUTI et al., 2010; SHARIF-KHODAEI; ALIABADI, 2014).

Despite its discovering in 1917, the advantages of using Lamb waves as a tool for defects detection in plates and other applications in NDT became clear only in 1960 with the study of Worlton (*General Electric Company*). Currently, the theory of Lamb waves is well documented in several works (VIKTOROV, 1967; GRAFF, 1975; CAWLEY; ALLEYNE, 1996; CHIMENTI, 1997; LOWE; ALLEYNE; CAWLEY, 1998; ROSE, 1999; SU; YE; LU, 2006).

At first Lamb waves were generated (and still are in some cases) from an obliquely incident bulk wave using a wedge, according to Snell's law (ALLEYNE; CAWLEY, 1992b; GUO; CAWLEY, 1994; GHOSH; KUNDU; KARPUR, 1998). The modes that can propagate in the plate have phase velocity equal to $c_{\text{wedge}} / \sin(\theta_{\text{wedge}})$, where c_{wedge} is the propagation velocity in the wedge material and θ_{wedge} is the angle of incidence, which is the angle that the transmitted wave makes with the normal of the plate surface. By selecting this angle and the band of frequencies of the signals, a single mode can be generated/received. However, the non-negligible mass/volume of the probe and limited access to complex geometry structures often reduce the practical applications of this kind of approach (SU; YE; LU, 2006).

Non-contact excitation of Lamb waves via laser-based ultrasonics and acquisition using laser interferometer are reputable methods for high precision, but the cost can limit broad application (GUO; ACHENBACH; KRISHNASWAMY, 1997; NIETHAMMER et al., 2001; VALLE; LITTLES JR., 2002). Optical fibre sensors have been increasingly used, ensuring immunity to electromagnetic interference, wide bandwidth and low power consumption (BOLLER, 2001). However they are more suitable for measurements of static characteristics, due to the low sampling rate of the conventional optical spectrum analyzers (GACHAGAN et al., 1999). One solution is the use of a fibre Bragg grating filter connected with a photodetector (TSUDA et al., 2004). However, better results are obtained when the fibre is embedded in the material, which, on the other hand, complicate its repair and replacement (ZHOU; SIM, 2002).

Alternatively, piezoelectric lead zirconate titanate (PZT) ceramics can be used (GIURGIUTIU, 2005; KONSTANTINIDIS; WILCOX; DRINKWATER, 2007; STASZEWSKI; MAHZAN; TRAYNOR, 2009; SHELKE et al., 2011; SU et al., 2009; LI; PENG; MENG, 2014), which may have excellent

mechanical strength, wide bandwidth, low power consumption and low acoustic impedance, as well as low cost. Due to the small mass (and volume), they can be attached to the surface or even be embedded in the structure, between different layers of a composite material, for example. The addition of polymers has enabled the development of flexible arrays, which can conform around the test structure and change the radiation pattern, reducing the mechanical coupling between the array elements, related to dead zone in the image (DRINKWATER; WILCOX, 2006).

Linear arrays using piezoelectric ceramics for low frequency guided wave applications (up to 1 MHz) are easy to manufacture and can be used to control the acoustic beam. This control can be done in real time by exciting all elements simultaneously (GIURGIUTIU, 2005; OSTACHOWICZ et al., 2009) or exciting one element each time and post-processing the acquired signals (HIGUTI et al., 2010). Two-dimensional (2D) arrays allows to image a 3D volume in front of it, in the case of bulk waves propagation, which is widely used in medical applications and NDT. In the case of plates, the resulting image is still a 2D image of the structure. However, 2D arrays are usually related to a larger number of elements (YU; GIURGIUTIU, 2008). An alternative is the use of sparse 2D arrays, which may follow a distribution pattern (QIANG; SHENFANG, 2009; STEPINSKI; AMBROZINSKI; UHL, 2013; LEVINE; MICHAELS, 2014) or be randomly distributed (MICHAELS, 2008; HARLEY; MOURA, 2013). Besides the grating lobes and high side lobes levels, the direct signal between transmitter and receiver (due to the 2D layout) results in many artifacts throughout the image, reducing the quality of images and defect detection. To overcome this effect, baseline techniques can be used, by subtracting the measured signals from a reference data recorded from the undamaged plate (MICHAELS; MICHAELS, 2007; LEVINE; MICHAELS, 2013), which is not always possible in practice. Furthermore, variations in experimental conditions such as temperature and sensors coupling, for example, modify the propagation velocity, the magnitude of the signals, SNR, among other parameters, and a different baseline for each new test or a compensation of those effects is necessary (CLARKE et al., 2009; PUTKIS; CROXFORD, 2013).

There are several sparse array design optimization projects. Steinberg (1976) proposed the use of random arrays, avoiding grating lobes by breaking the periodicity in the elements distribution. On the other hand, side lobes levels are significantly increased. Lockwood et al. (1996) and Lockwood and Foster (1996) used different apertures in transmission and reception. The transmit and receive grating lobes could be moved to different positions in the two-way radiation pattern where their contributions would destructively interfere. Each aperture (transmission and reception) has different pitches and the effective aperture presents a $\lambda/2$ -pitch. The side lobes levels reduction is obtained by the use of apodization functions. The optimization variables are the apodization, the elements distribution (HOLM; ELGETUN; DAHL, 1997) and elements geometry (BAVARO; CALIANO; PAPPALARDO, 2008). Different methods can be applied as linear and dynamic programming (SKOLNIK; NEMHAUSER; SHERMAN, 1964), genetic algorithms (HAUPT,

1994), and others for minimizing the maximum error and side lobes levels (AUSTENG et al., 1997), for example.

Since the search space for layout/apodization optimization for arrays is so vast, the comparison between the methods to obtain the best array configuration is impractical, and the comparison should be done for each parameter (main lobe width, maximum and average side and grating lobes levels). An alternative to improve performance is the extraction of additional information from the data set by signal processing, as the use of the phase of the signals (OPPENHEIM; LIM, 1981), which has been shown a good alternative to improve defect detection and image quality without increasing the cost and complexity of the system.

Camacho, Parrilla and Fritsch (2009) presented a method based on the analysis of the variance of the phase at the aperture data and Martínez-Graullera et al. (2011) proposed a spectral analysis of the phase distribution. Both works result in coherence factors that are used to weight the amplitude images, reducing side and grating lobes artifacts and improving contrast and dynamic range. The optimization methods, as well as the coherence factors, were originally developed to be applied in medical applications and NDT using bulk waves in single mode propagation. However they can also be used in inspections with Lamb waves, generated by PZT ceramics for both full-populated and sparse arrays. The phase is addressed in this work to improve reflectors detectability and image quality.

PZT-generated Lamb waves unavoidably contain multiple modes, which depend on its geometry and dimensions, plate properties, frequency of excitation and other parameters (SANTONI et al., 2007). Each propagation mode has its own dispersion characteristic, making difficult the analyze of the signals. For this reason, single mode operation is desirable.

In general, the fundamental symmetric (S_0) or antisymmetric (A_0) modes at low frequencies are used. Michaels and Michaels (2007) excited the array with broadband pulses and Michaels et al. (2013) with chirp signals, which were followed by post-processing to operate with certain propagation modes and frequencies. Giurgiutiu (2005) excited only one mode by selecting the operational frequency for a given transducer geometry and Grondel et al. (2002) made the mode selection by matching different transducers. To minimize the dispersion effects, narrowband signals can be used. On the other hand, it may limit the axial resolution of the system, due to the pulse duration (ROSE, 2000; SU; YE; LU, 2006). An alternative is to compensate the dispersion from the knowledge of the signals features and the dispersion characteristics (WILCOX; CAWLEY, 2001; WILCOX, 2003a; XU; YU; GIURGIUTIU, 2009).

Each propagation mode is sensitive to a different type of defect (notches, delamination, surface) (ROSE, 2000). Alleyne and Cawley (1992a) observed that the defect sensitivity depends on the defect geometry, the propagation mode and frequency. Michaels et al. (2011) obtained different images by considering the A_0 and S_0 modes at different frequencies and concluded that these parameters change defects representation.

Michaels and Michaels (2007) excited a sparse array with broadband pulses and one image was produced for each frequency. An image fusion was made by taking the minimum value of all images for a given pixel. As a result, damages were detected and image artifacts were reduced by using a small number of sensors. The authors used the propagation velocity of the dominant mode, but did not consider the possible presence of more than one mode simultaneously, neither the dispersion characteristics, which may result in artifacts in the image. In this work, mode diversity is also explored to improve image quality.

The use of minimum value for pixel selection in an image compounding procedure can result in non-detection of a reflector if it is not represented in at least one image. By the use of the maximum of all images, artifacts in some of them would be considered reflectors in the final image. Davies and Cawley (2007) obtained a compounded image by summing all images. An intermediate approach related to the selection of the minimum and maximum of two or more images was proposed by Higuti et al. (2010), using a coherence image to select the maximum or the minimum of the amplitude images obtained with two arrays with different apodizations, resulting in a high-resolution image. The selection is done by applying a 70% threshold to a coherence image, pixel by pixel, and if the pixel intensity is above threshold it is considered a reflector, and the maximum between the images is taken. If it is below threshold, the minimum is selected.

Although there are many applications of Lamb waves propagation in isotropic plates and studies in defect detection and imaging of plates using piezoelectric ceramics and different propagation modes, the limited quality of the results obtained by conventional methods (HOLMES; DRINKWATER; WILCOX, 2005) opens opportunities for researches in different fields of application. Coherence factors (CAMACHO; PARRILLA; FRITSCH, 2009; MARTÍNEZ-GRAULLERA et al., 2011) and image compounding techniques (MICHAELS; MICHAELS, 2007; HIGUTI et al., 2010) by the processing of data signals are important and promising areas, since they use different sources of information (the amplitude and phase for the first, frequencies and spatial and apodization diversities for the second) to improve image quality without increasing the cost of the system. Although coherence images used as weighting factors result in improvements in quality of images, they contain more information that could be used to improve the original weighting factors, as well as to indicate the presence of reflectors. Furthermore, some methods use parameters, such as thresholds for damage detection and selection of images in compounding procedures. For example, Higuti et al. (2010) applied a 70% threshold to a coherence image to indicate the presence of defects to select the maximum or the minimum of different amplitude images obtained with two arrays using uniform and Blackman apodizations. Yu and Giurgiutiu (2008) used a 80% threshold that was applied to an amplitude image, resulting in a binary image, which in turn is multiplied by the original image to reduce side lobes influence and background noise. The threshold value controls the sensitivity of the techniques and then must be properly designed, since it influences directly in the quality of the results.

1.2 OBJECTIVE

The aim of this work is to explore coherence methods and image compounding techniques, by considering the information contained in the phase of the signals and the Lamb mode diversity in ultrasonic NDT of plate-like structures, in order to develop methods to improve the quality of the images and defects detectability compared to those obtained with conventional techniques.

1.3 DEVELOPMENT OF THE STUDY

This work was totally supported by Fundação de Amparo à Pesquisa do Estado de São Paulo (FAPESP - process 2010/16400-0), performed at the Ultrasound Laboratory of the Department of Electrical Engineering, Faculdade de Engenharia de Ilha Solteira, Universidade Estadual Paulista “Júlio de Mesquita Filho” (UNESP), and has the contribution of the Ultrasound Laboratory of the Department of Mechatronics and Mechanical Systems of Escola Politécnica da Universidade de São Paulo. A research project (FAPESP - process 2010/02240-0) was conducted together with the studies, since they were in the same area, which was important to lead the initial studies and experiments. A five-months research internship (June - October 2013) was done at the Ultrasonic Non-Destructive Testing group of the Consejo Superior de Investigaciones Científicas (Madrid, Spain) to develop some of the topics described in this work (FAPESP/BEPE - process 2013/00330-0).

1.4 OUTLINE OF THESIS

Chapter 2 presents the main characteristics of Lamb waves propagation in isotropic plates: propagation modes, dispersion curves (respect to phase and group velocities and wavenumber), cutoff frequencies and dispersion compensation.

The study of arrays characteristics is presented in chapter 3, which considers the radiation pattern of linear full-populated and sparse arrays, apodization functions, effect of the finite size of the transducer, focusing and beam steering, coarray, the excitation pulse duration and characteristics of two-dimensional arrays.

Chapter 4 introduces a technique for synthetic aperture imaging using the TFM (Total Focusing Method) method, which is the more widely used since its proposal. Simulated images for point reflectors with different arrays configurations, apodizations and propagation modes are also presented.

The two proposed techniques are detailed in chapter 5: (i) instantaneous phase image, which

uses only the instantaneous phase of signals in beamforming. From a statistical analysis of the proposed image, which depends on the number of signals (which in turn depends on the number of elements of the array) and the noise, a threshold is defined, as a function only of the system parameters, which can be used as an indicator of defects, as a selection parameter in image compounding techniques and to create a coherence factor; (ii) Lamb mode diversity compounding technique, which uses the threshold and coherence factor proposed in (i) to combine the different representations of defects obtained with different propagation modes.

Chapter 6 presents the experimental setup, as well as the results and discussions. As a result of applying the techniques (i) and (ii), dead zone and artifacts are reduced, and contrast is increased.

The final chapter presents conclusions and reviews of all work, considerations and proposals for improvements of the results, a list of publications as result of this study, and suggestions for future work.

2 LAMB WAVES

The first studies on wave propagation in plates were conducted by Rayleigh (1885) and Lamb (1917). The Rayleigh-Lamb theory is related to waves that can propagate in infinite and traction-free plates.

Bulk waves propagate in materials whose dimensions are much larger than the wavelength, such as waves propagating in the deep ocean, for example in sonar applications. However, in cases as plate-like structures, often there are interactions with boundaries by way of reflection and refraction, and mode conversion occurs between longitudinal and shear waves. Although guided and bulk waves are fundamentally different, both of them are governed by the same set of partial differential wave equations. Mathematically, the main difference is that, for bulk waves propagation, there are no boundary conditions that need to be satisfied. On the other hand, the solution to a guided wave must satisfy the governing equations as well as some physical boundary conditions, which makes difficult to obtain analytical solutions (ROSE, 1999).

Some examples of guided waves are:

- Rayleigh waves: free waves that propagate on the surface of a semi-infinite solid. The amplitude of the waves decays rapidly with depth. These waves comprise the main type of wave observed in earthquakes;
- Stoneley waves: high-amplitude surface waves (or interface waves) that typically propagate along a solid-solid interface. When found at a liquid-solid interface, this wave is referred to as Scholte waves. The wave is of maximum intensity at the interface and decreases exponentially away from it;
- Lamb waves: waves that propagate in traction-free plates.

With high susceptibility to interference along the propagation medium, either with a defect or the boundaries of the plate, Lamb waves propagate over long distances with low attenuation. The entire thickness of a plate can be inspected by different propagation modes, allowing the detection of internal and surface defects.

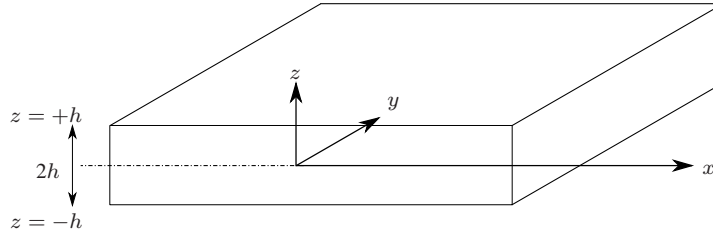
There are two different types of particle displacements, which are related to two sets of propagation modes: symmetric and antisymmetric. Other characteristic is the dispersion, which means that the phase and group velocities vary as function of frequency.

2.1 SYMMETRIC AND ANTISYMMETRIC MODES

Figure 1 illustrates the problem geometry: elastic guided wave propagation in a traction-free homogeneous and isotropic plate. The initial considerations are:

- i Plate thickness equal to $2h$ (z direction);
- ii Infinite dimensions in x and y directions;
- iii Wave propagation in x direction;
- iv Due to the problem symmetry, there are displacements only in the x and z directions ($\vec{u} = u_x\hat{x} + u_z\hat{z}$ and $u_y = 0$) and $\partial/\partial y = 0$.

Figure 1 – $2h$ -thickness plate with infinite dimensions in x and y directions.



Source: Elaborated by the author.

According to Kino (1987) the displacement vector is given by:

$$\vec{u} = \nabla\Phi + \nabla \times \vec{\Psi}, \quad (1)$$

where Φ and $\vec{\Psi}$ are scalar and vector potential functions, respectively. The potential Φ express the strains, related to dilatation, which causes changes in volume, and the potential $\vec{\Psi}$ express the shear strains, associated with rotational elements.

From (1) and considering that $\vec{u} = u_x\hat{x} + u_z\hat{z}$ and $u_y = 0$ (item iv):

- $\Phi = \Phi(x, z, t)$

$$\nabla\Phi = \frac{\partial\Phi}{\partial x}\hat{x} + \frac{\partial\Phi}{\partial z}\hat{z}; \quad (2)$$

- $\vec{\Psi} = \Psi(x, z, t)\hat{y}$

$$\nabla \times \vec{\Psi} = -\frac{\partial\Psi}{\partial z}\hat{x} + \frac{\partial\Psi}{\partial x}\hat{z}. \quad (3)$$

By replacing (2) and (3) in (1):

$$u_x = \frac{\partial\Phi}{\partial x} - \frac{\partial\Psi}{\partial z} \quad (4)$$

$$u_z = \frac{\partial \Phi}{\partial z} + \frac{\partial \Psi}{\partial x} . \quad (5)$$

According to Rose (1999), the wave equations can be written as:

$$\begin{aligned} \nabla^2 \Phi - \frac{1}{c_L^2} \frac{\partial^2 \Phi}{\partial t^2} &= 0 \\ \nabla^2 \vec{\Psi} - \frac{1}{c_T^2} \frac{\partial^2 \vec{\Psi}}{\partial t^2} &= 0, \end{aligned} \quad (6)$$

where $c_L = \sqrt{(\Lambda + 2\mu)/\rho}$ and $c_T = \sqrt{\mu/\rho}$ are the longitudinal and shear velocities, respectively. $\Lambda = \frac{\nu E}{(1+\nu)(1-2\nu)}$ and $\mu = \frac{E}{2(1+\nu)}$ are the Lamé constants, E is the Young's elastic modulus, ν is the Poisson coefficient and ρ is the material density.

By considering a harmonic time dependence and propagation in the x direction, the solution of (6) can be given by:

$$\begin{aligned} \Phi &= F(z)e^{j(\omega t - kx)} \\ \vec{\Psi} &= jH(z)e^{j(\omega t - kx)}\hat{y}, \end{aligned} \quad (7)$$

where k is the wavenumber, given by $k = \omega/c = 2\pi/\lambda$, ω is the angular frequency ($\omega = 2\pi f$), c is the phase velocity and λ is the wavelength, considering $j^2 = -1$, where j is the imaginary unit. F and H are auxiliary functions for mathematical development of the equations. By substituting (7) in (6):

$$\begin{aligned} \frac{d^2 F(z)}{dz^2} + a_L^2 F(z) &= 0 \\ \frac{d^2 H(z)}{dz^2} + a_T^2 H(z) &= 0. \end{aligned} \quad (8)$$

The variables a_L and a_T are given by:

$$a_L^2 = \frac{\omega^2}{c_L^2} - \frac{\omega^2}{c^2} \quad (9)$$

$$a_T^2 = \frac{\omega^2}{c_T^2} - \frac{\omega^2}{c^2}. \quad (10)$$

Solving (8), F and H are written as:

$$\begin{aligned} F(z) &= A \sin(a_L z) + B \cos(a_L z) \\ H(z) &= C \sin(a_T z) + D \cos(a_T z). \end{aligned} \quad (11)$$

Then:

$$\begin{aligned} \Phi &= [A \sin(a_L z) + B \cos(a_L z)] e^{j(\omega t - kx)} \\ \vec{\Psi} &= j [C \sin(a_T z) + D \cos(a_T z)] e^{j(\omega t - kx)} \hat{y}. \end{aligned} \quad (12)$$

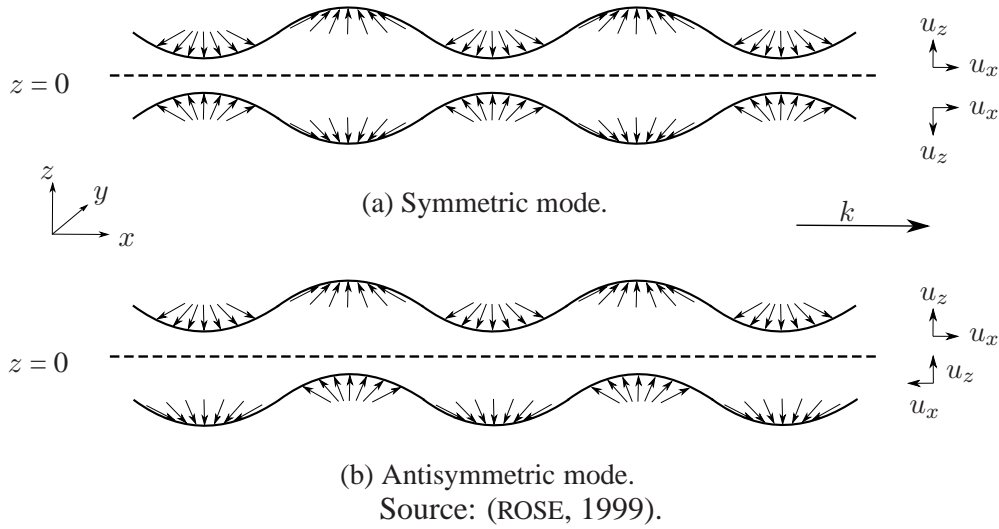
By replacing (12) in (4) and (5), the displacements are:

$$\begin{aligned} u_x &= -j [(kB \cos(a_L z) + a_T C \cos(a_T z)) + (kA \sin(a_L z) - a_T D \sin(a_T z))] e^{j(\omega t - kx)} \\ u_z &= [- (a_L B \sin(a_L z) - kC \sin(a_T z)) + (a_L A \cos(a_L z) + kD \cos(a_T z))] e^{j(\omega t - kx)}, \end{aligned} \quad (13)$$

where A , B , C and D are constants, whose values depend on the excitation procedure.

The sine terms of u_z and cosine terms of u_x are related to symmetric motion respect to the midplane of the plate and the cosine terms of u_z and sine terms of u_x are related to antisymmetric motion respect to the axis z , which gives rise to the separation into two propagation modes: symmetric and antisymmetric, as illustrated in Figure 2.

Figure 2 – Lamb wave displacements in the plate for (a) symmetric and (b) antisymmetric propagation modes.



Thereby, the symmetric displacement respect to the midplane of the plate is:

$$\begin{aligned} u_x &= -j [kB \cos(a_L z) + a_T C \cos(a_T z)] e^{j(\omega t - kx)} \\ u_z &= - [a_L B \sin(a_L z) - kC \sin(a_T z)] e^{j(\omega t - kx)}, \end{aligned} \quad (14)$$

and the antisymmetric is:

$$\begin{aligned} u_x &= -j [kA \sin(a_L z) - a_T D \sin(a_T z)] e^{j(\omega t - kx)} \\ u_z &= [a_L A \cos(a_L z) + kD \cos(a_T z)] e^{j(\omega t - kx)}. \end{aligned} \quad (15)$$

By considering a traction-free plate, the boundary conditions are: $T_{xz} = T_{yz} = T_{zz} = 0$, for $z = \pm h$, where $T_{i_1 i_2}$ is the stress relating force in i_1 direction in the cross-sectional whose normal is in i_2 direction, for $i_1, i_2 = x, y$ and z , and $T_{i_1 i_2} = T_{i_2 i_1}$. For isotropic media, the

Hooke's law, which relates stress and strain in the region of elastic linearity is (GRAFF, 1975):

$$\begin{bmatrix} T_{xx} \\ T_{yy} \\ T_{zz} \\ T_{yz} \\ T_{xz} \\ T_{xy} \end{bmatrix} = \begin{bmatrix} \Lambda + 2\mu & \Lambda & \Lambda & 0 & 0 & 0 \\ \Lambda & \Lambda + 2\mu & \Lambda & 0 & 0 & 0 \\ \Lambda & \Lambda & \Lambda + 2\mu & 0 & 0 & 0 \\ 0 & 0 & 0 & \mu & 0 & 0 \\ 0 & 0 & 0 & 0 & \mu & 0 \\ 0 & 0 & 0 & 0 & 0 & \mu \end{bmatrix} \begin{bmatrix} S_{xx} \\ S_{yy} \\ S_{zz} \\ 2S_{yz} \\ 2S_{xz} \\ 2S_{xy} \end{bmatrix}, \quad (16)$$

where $S_{i_1 i_2}$ is the strain given by $S_{i_1 i_2} = \frac{1}{2} \left(\frac{\partial u_{i_1}}{\partial i_2} + \frac{\partial u_{i_2}}{\partial i_1} \right)$, for $i_1, i_2 = x, y$ and z , and $S_{i_1 i_2} = S_{i_2 i_1}$.

Then:

$$\begin{aligned} T_{xz} &= \mu \left(\frac{\partial u_x}{\partial z} + \frac{\partial u_z}{\partial x} \right) = 0 \\ T_{yz} &= \mu \left(\frac{\partial u_y}{\partial z} + \frac{\partial u_z}{\partial y} \right) = 0 \\ T_{zz} &= \Lambda \left(\frac{\partial u_x}{\partial x} + \frac{\partial u_y}{\partial y} \right) + (\Lambda + 2\mu) \left(\frac{\partial u_z}{\partial z} \right) \\ &= \Lambda \left(\frac{\partial u_x}{\partial x} \right) + (\Lambda + 2\mu) \left(\frac{\partial u_z}{\partial z} \right) = 0. \end{aligned} \quad (17)$$

By replacing the symmetric mode displacement equation (14) in (17) and applying the boundary conditions at $z = h$:

$$\begin{aligned} T_{xz} &= j\mu [2ka_L B \sin(a_L h) - (k^2 - a_T^2) C \sin(a_T h)] e^{j(\omega t - kx)} = 0 \\ T_{zz} &= \{ -[(\Lambda + 2\mu) a_L^2 + \Lambda k^2] B \cos(a_L h) + 2\mu k a_T C \cos(a_T h) \} e^{j(\omega t - kx)} = 0. \end{aligned} \quad (18)$$

Using (9), (10) and the velocities relations $c_L^2 = (\Lambda + 2\mu)/\rho$ and $c_T^2 = \mu/\rho$, (18) is rewritten as:

$$\begin{cases} -2ka_L B \sin(a_L h) + (k^2 - a_T^2) C \sin(a_T h) = 0 \\ (k^2 - a_T^2) B \cos(a_L h) + 2ka_T C \cos(a_T h) = 0. \end{cases} \quad (19)$$

The B and C constants values depend on the excitation and can be related as:

$$\frac{B}{C} = -\frac{2ka_T \cos(a_T h)}{(k^2 - a_T^2) \cos(a_L h)} = \frac{(k^2 - a_T^2) \sin(a_T h)}{2ka_L \sin(a_L h)}. \quad (20)$$

The matrix notation for (19) is:

$$\begin{bmatrix} -2ka_L \sin(a_L h) & (k^2 - a_T^2) \sin(a_T h) \\ (k^2 - a_T^2) \cos(a_L h) & 2ka_T \cos(a_T h) \end{bmatrix} \begin{bmatrix} B \\ C \end{bmatrix} = \begin{bmatrix} 0 \\ 0 \end{bmatrix}. \quad (21)$$

The same procedure can be done for $z = -h$, resulting in (21). The determinant of the coefficient matrix vanishes in order to ensure solutions other than the trivial one. From this, the Rayleigh-Lamb frequency relation for symmetric modes is:

$$\frac{\tan(a_T h)}{\tan(a_L h)} = \frac{-4k^2 a_L a_T}{(k^2 - a_T^2)^2}. \quad (22)$$

Proceeding analogously, by replacing (15) in (17) and applying the boundary conditions for $z = \pm h$, A and D constants can be related from:

$$\frac{A}{D} = -\frac{2ka_T \sin(a_T h)}{(k^2 - a_T^2) \sin(a_L h)} = \frac{(k^2 - a_T^2) \cos(\beta h)}{2ka_L \cos(a_L h)}, \quad (23)$$

and the Rayleigh-Lamb frequency relation for antisymmetric modes is:

$$\frac{\tan(a_T h)}{\tan(a_L h)} = \frac{-(k^2 - a_T^2)^2}{4k^2 a_L a_T}. \quad (24)$$

Since a_L and a_T depend on the frequency non-linearly, the solutions k_i for $i = 1, 2, 3, \dots$ are also non-linearly frequency dependent. Consequently, the phase velocities given by $c_i = \omega/k_i$ are also dependent on frequency, which is the dispersion phenomenon.

The solutions of (22) and (24) relate frequency with wavenumber, and consequently, with phase and group velocities. The graphical view of the solutions is known as dispersion curves (ROSE, 1999).

2.2 DISPERSION CURVES

Although (22) and (24) look simple, they can be solved only by numerical methods. They present complex roots, whose real part is related to the propagation and imaginary part to the attenuation. If the imaginary part is equal to zero, it is associated with no attenuation propagation. If it is greater than zero, the waves grow exponentially with distance, and if it is less than zero the waves decay exponentially with distance. The second case has not been physically observed. The decaying waves are presented in loaded plates, in water-immersed plates, for example, where the out-of-plane displacement at the surface of the plate produces normal loading on the fluid and hence leakage into the fluid. Other case of decaying waves is the propagating in viscoelastic materials. Therefore, for Lamb propagation in the unloaded plate problem, an approximation can be used considering only real values for k .

In order to avoid sine and cosine terms at denominator, to prevent singularities, (22) and

(24) can be rewritten as:

$$\frac{\sin(a_T h) \cos(a_L h)}{a_T} + \frac{4k^2 a_L}{(k^2 - a_T^2)^2} \cos(a_T h) \sin(a_L h) = 0, \quad (25)$$

for symmetric modes and

$$\frac{\sin(a_T h) \cos(a_L h)}{a_T} + \frac{(k^2 - a_T^2)^2}{4k^2 a_T^2 a_L} \cos(a_T h) \sin(a_L h) = 0, \quad (26)$$

for antisymmetric modes.

The dispersion curves are usually presented as a 2D plot relating the phase velocity (or group velocity or wavenumber) as a function of the frequency-half-thickness product ($f.h$). The solutions of (25) and (26) were obtained by performing the following steps in MATLAB:

1. choose a range (initial, step and end values) for the frequency-half-thickness product ($f.h$);
2. determine the maximum wavenumber (ordinate axis);
3. for each frequency-half-thickness product value, find the roots of (25) and (26). Each zero crossing is related to a propagation mode.

Figure 3 presents the wavenumber dispersion curves for an aluminum plate ($c_L = 6400$ m/s and $c_T = 3100$ m/s). From this result and considering that $k = \omega/c$, the phase velocity dispersion curves were obtained, as illustrated in Figure 4. Some typical characteristics can be observed:

- for low $f.h$ values there are two fundamental propagation modes, the antisymmetric A0 and the symmetric S0;
- in this case, the S0 mode presents low dispersion characteristic, unlike the A0 mode;
- at high $f.h$ values other modes can be coupled;
- for large $f.h$ values the A0 and S0 modes converge to the Rayleigh wave velocity (2850 m/s) and the other modes converge to the shear velocity (3100 m/s).

The group velocity (c_g) can be found from the phase velocity by use of (ROSE, 1999):

$$c_g = \frac{d\omega}{dk} = \left[\frac{d\left(\frac{\omega}{c}\right)}{d\omega} \right]^{-1} = \left[\frac{c - \omega \frac{dc}{d\omega}}{c^2} \right]^{-1} = \frac{c}{1 - \frac{\omega}{c} \frac{dc}{d\omega}}. \quad (27)$$

The group velocity calculation requires high resolution in the frequency-half-thickness product range due to the term $dc/d\omega$, resulting in high computational cost (time and memory).

Figure 3 – Wavenumber dispersion curves for an aluminum plate. Symmetric modes in solid lines and antisymmetric modes in dashed lines.

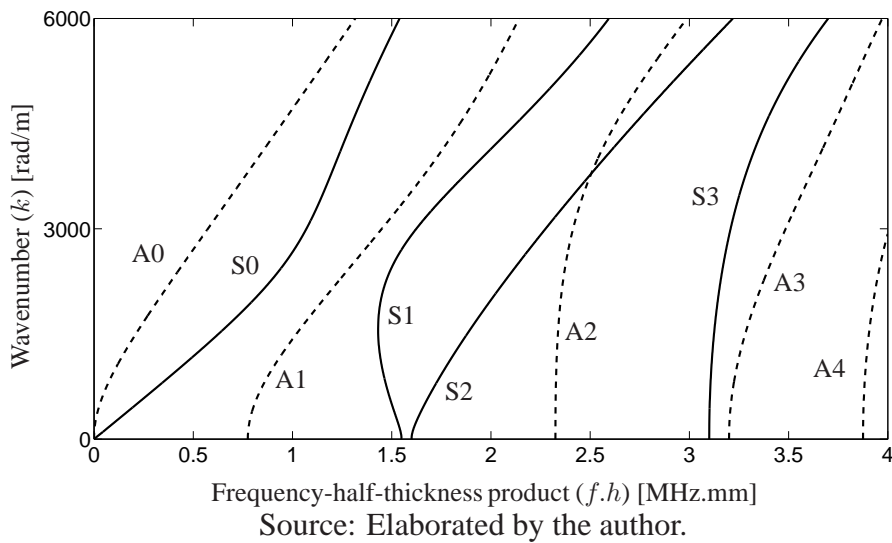
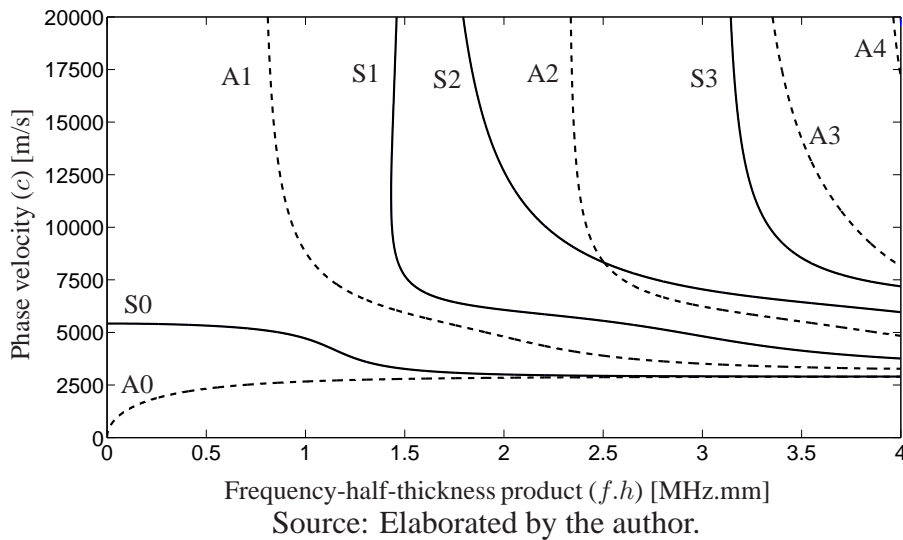


Figure 4 – Phase velocity dispersion curves for an aluminum plate. Symmetric modes in solid lines and antisymmetric modes in dashed lines.

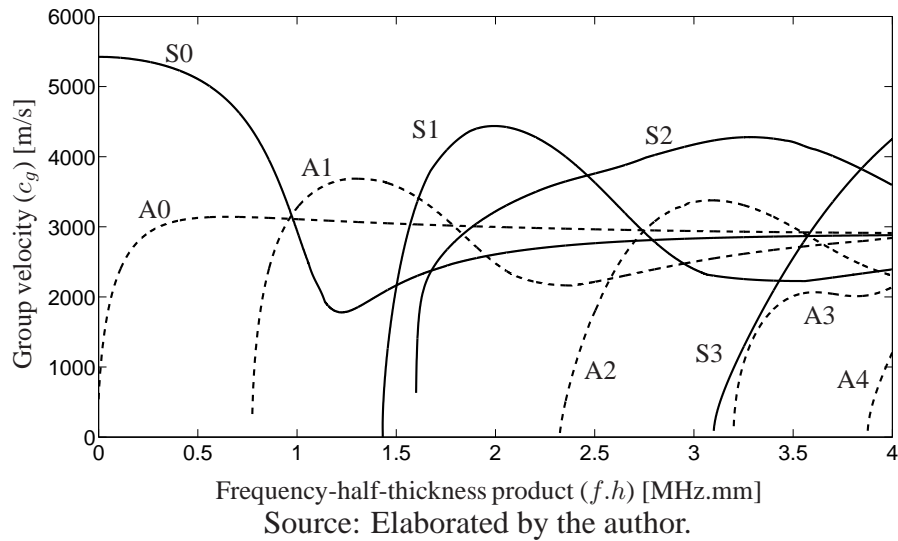


However, this term can be obtained analytically from the phase velocity (MAYSENHOLDER, 1992). The group velocity dispersion curves for an aluminum plate are illustrated in Figure 5.

2.3 CUTOFF FREQUENCY

In a $2h$ -thickness plate, for a given frequency value, several propagation modes can be coupled with different phase and group velocities (VIKTOROV, 1967), as can be observed in Figures 3, 4 and 5. For each mode type, symmetric and antisymmetric, there are the fundamental modes (zero order), which can be excited even at low frequencies, and there are other that can

Figure 5 – Group velocity dispersion curves for an aluminum plate. Symmetric modes in solid lines and antisymmetric modes in dashed lines.



only be coupled for frequencies higher than a specific value, called cutoff frequency.

At these points the phase velocity approaches infinity as the group velocity and wavenumber approach zero. Then, mode cutoff values can be calculated by examining a limiting condition $k \rightarrow 0$ ($c \rightarrow \infty$). By considering these conditions in (22):

$$\begin{aligned} \tan(a_T h) &\rightarrow 0 \\ \tan(a_L h) &\rightarrow \infty, \end{aligned} \quad (28)$$

and replacing (9) and (10) in (28), for $\omega = \omega_c$, then:

$$\begin{aligned} \tan\left(\frac{\omega_c}{c_T} h\right) &\rightarrow 0 \\ \tan\left(\frac{\omega_c}{c_L} h\right) &\rightarrow \infty. \end{aligned} \quad (29)$$

From (29), the cutoff frequencies values for the symmetric modes are:

$$f_c = \begin{cases} \frac{c_T}{2h}, \frac{2c_T}{2h}, \frac{3c_T}{2h}, \frac{4c_T}{2h}, \dots \\ \frac{c_L}{4h}, \frac{3c_L}{4h}, \frac{5c_L}{4h}, \frac{7c_L}{4h}, \dots \end{cases} \quad (30)$$

Proceeding along analogous lines for the antisymmetric mode, by considering $k \rightarrow 0$ ($c \rightarrow$

∞) in (24), the cutoff frequencies values for the antisymmetric modes are:

$$f_c = \begin{cases} \frac{c_T}{4h}, \frac{3c_T}{4h}, \frac{5c_T}{4h}, \frac{7c_T}{4h}, \dots \\ \frac{c_L}{2h}, \frac{2c_L}{2h}, \frac{3c_L}{2h}, \frac{4c_L}{2h}, \dots \end{cases} \quad (31)$$

2.4 DISPERSION COMPENSATION

At low values of the frequency-half-thickness product the A0 mode presents high dispersion, resulting in changes in shape of the signal as it propagates. However, when the dispersion curves are known this effect can be compensated. Wilcox (2003a) presents a technique that maps the signals from the time-domain to the spatial-domain (propagated distance). Considering $g(t)$ the signal with dispersion, the compensated signal is given by:

$$g_{\text{comp}}(x) = \int_{-\infty}^{\infty} G_{\text{comp}}(k) e^{-jkx} dk, \quad (32)$$

where:

$$G_{\text{comp}}(k) = G(\omega) c_g(\omega), \quad \omega = \omega(k), \quad (33)$$

and $G(\omega)$ is the Fourier transform of $g(t)$.

According to Xu, Yu and Giurgiutiu (2009), the Lamb wave nonlinear wavenumber $k(\omega)$ causes phase distortions and results in a still dispersed waveform. The authors propose the use of the linear wavenumber, which is approximated by using the Taylor expansion of the wavenumber at the excitation central frequency ω_0 up to the first order as:

$$k_{\text{linear}}(\omega) = k(\omega_0) + \frac{\omega - \omega_0}{c_g(\omega_0)}. \quad (34)$$

The time information from the compensated signal is extract by using:

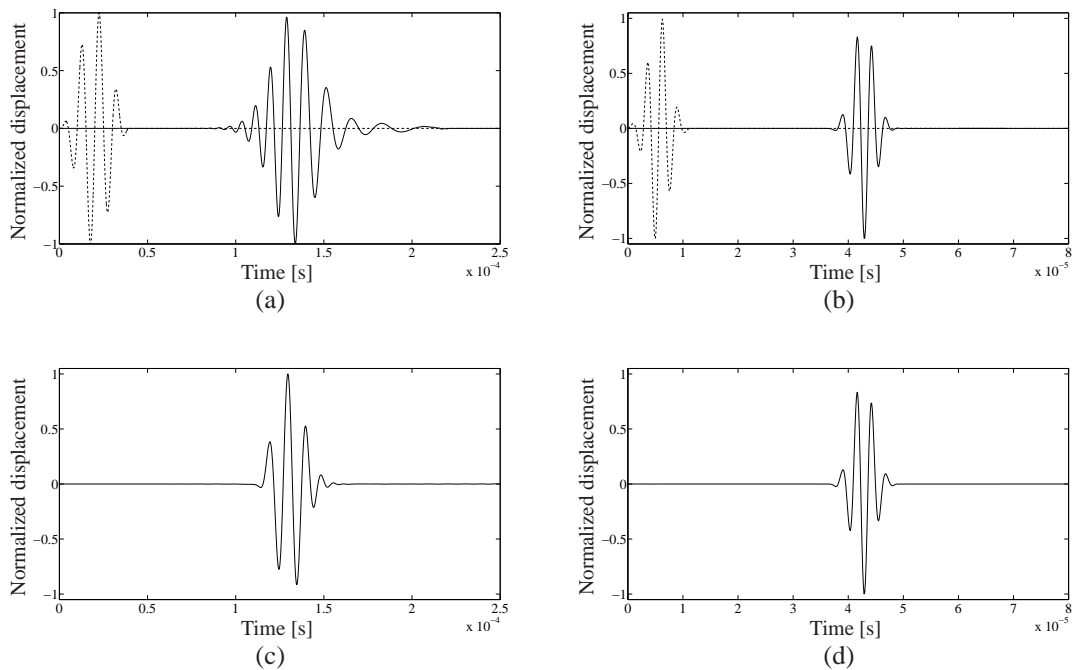
$$t = \frac{x}{c_g(\omega_0)}. \quad (35)$$

A 1 mm thickness isotropic aluminum plate (1 m \times 1 m) was simulated in *PZFlex*, which is a finite element modeling (FEM) software to simulate the static and dynamic response of an object to certain loading conditions, such as force, pressure, electric field (WEIDLINGER ASSOCIATES INC, 2009. 200 p). The basic concept of FEM is the division of the structure into a set of small pieces, which are called finite elements, and the set of finite elements, in turn, is named grid. FEM is a search by local solutions (each element separately) that can be generalized for the entire domain. Then, force, pressure, stress, displacement and other variables are calculated for a single element, and these values are proportionally transferred to the neighboring elements.

For this simulation, squared elements and 12 elements per wavelength were considered.

A point pressure was applied at the center of the plate in order to obtain a single mode propagation, which was achieved by applying the same point pressure waveform to the top and bottom surfaces for the S0 mode and with opposite sign for the A0 mode. A 4-cycles Gaussian envelope RF signal was considered at 100 kHz and 360 kHz for A0 and S0 modes, respectively. The out-of-plane displacement was recorded at 20 cm from the excitation point and the dispersion compensation method was applied. The result is shown in Figure 6.

Figure 6 – Out-of-plane displacement at 20 cm from the excitation point. (a) A0 and (b) S0 modes before and (c) A0 and (d) S0 modes after the dispersion compensation. Excitation signal in dashed line.



Source: Elaborated by the author.

For small $f.h$ values the S0 mode has low dispersion, unlike the A0 mode, whose signal has the initial shape changed. After the dispersion compensation the shape of the excitation signal is recovered for the A0 mode. The S0 mode presents low dispersive characteristic with no significant improvements after dispersion compensation.

According to Wilcox (2003a), the accuracy of the dispersion compensation procedure is determined by the accuracy of the dispersion data. There are certain extreme situations where the dispersion compensation could yield worse results than processing without it, for example if longitudinal or shear velocities values different from the original ones are used to obtain the dispersion curves. In general, it can be concluded that the dispersion compensation procedure is a stable technique that usually will give superior results to processing without dispersion compensation.

2.5 COMMENTS

In a plate there are several possible propagation modes, which can be coupled simultaneously according to the excitation system and signal parameters, with different dispersion characteristics. The effect of dispersion should be considered, since it changes the original signal shape, which may result in inaccurate interpretations of the results, such as false defects or even wrong sizes and positions respect to real ones in ultrasonic images, as shown in chapters 4 and 6. Thus, a study of Lamb waves propagation in an isotropic plate (achievement and interpretation of dispersion curves), cutoff frequencies, dispersion characteristics and a compensation procedure from each propagation mode knowledge were presented in this chapter.

3 ARRAYS

An array is a set of transducers geometrically arranged according to some patterns (linear or two-dimensional, for example), whose acoustic beam can be electronically controlled. Thus an image of a plane or volume of interest can be obtained without the necessity of moving the transducers (DRINKWATER; WILCOX, 2006).

By considering the array characteristics as well as its geometry and acoustic properties of the material, the time delay for each element excitation is calculated to generate individual wave fronts, which combine to each other constructively and destructively, resulting in a unique wave front that propagates through the material. The radiation pattern can be changed, scanning different angles and depths in short time.

An ideal array would have an infinite number of infinitesimally spaced elements, each one able to independently generate an arbitrary waveform and receive the reflected signals. Although this configuration is still far from achievable, the increased performance and reduced size of electronics, as well as the yearly increase in computing power, means that this aim is getting closer. Therefore, the system is limited by the electrical instrumentation (number of independent channels in transmission and reception) and the array characteristics.

The element spacing is called pitch (d). The aperture is the subset of elements used in the inspection, which can be electronically changed, increasing or decreasing the number of elements, moving the active elements along the total available aperture, depending on the application.

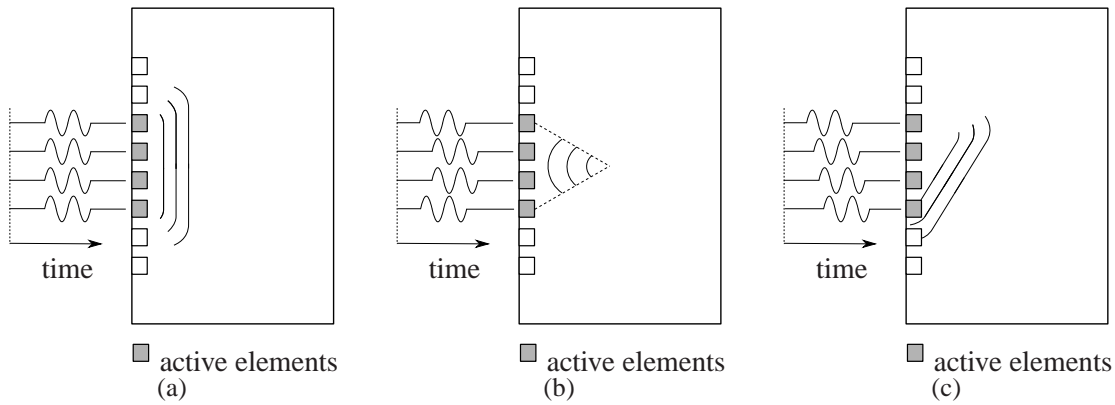
A plane wave is obtained by exciting the elements in phase, as presented in Figure 7a. Figures 7b and 7c illustrate a focused and steered beam, respectively, which can be produced with different delays, i.e. by exciting the elements at different times.

3.1 TYPES OF ARRAYS

In general an array can be classified as one-dimensional (1D or linear) or two-dimensional (2D). A linear array consists of elements distributed in a line. Despite the easy construction, its aperture size is proportional to the focusing depth, the beam divergence increases with the angle and distance, and the inspection is limited by a plane. Even so it is the most used array. An 8-elements linear array with pitch d can be observed in Figure 8.

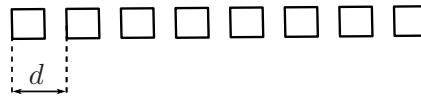
Two-dimensional arrays consists of elements arranged in an area and then allow to obtain 3D images (using bulk waves) and greater control of the beam. Traditionally the array lay-

Figure 7 – Different wave fronts: (a) plane wave, (b) focused beam and (c) beam steering.



Source: Elaborated by the author.

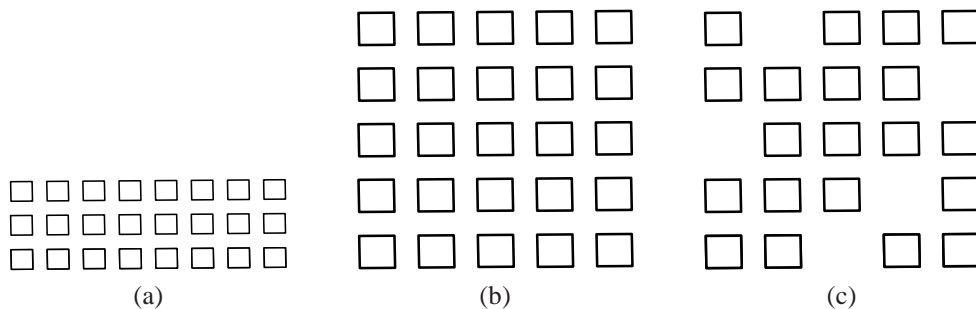
Figure 8 – Linear array.



Source: Elaborated by the author.

out was based on a square or rectangular (1.5D) grids. Furthermore it can also be arranged in the form of concentric circles (MARTÍNEZ; AKHNAK; ESPINOSA, 2003) or circular elements distributed around a circular area (NORTON, 1992). Cross-shaped, stars and spirals layouts are also used (YU; GIURGIUTIU, 2008; STEPINSKI; AMBROZINSKI; UHL, 2013). The use of fewer elements randomly distributed (sparse) enhances the array performance in imaging applications when compared to other distribution patterns, even when the distance between the elements is larger (DRINKWATER; WILCOX, 2006). Figure 9 illustrates some configurations.

Figure 9 – Two-dimensional arrays: (a) rectangular, (b) square and (c) sparse grids.



Source: Elaborated by the author.

3.2 LINEAR ARRAY

By considering a harmonic point acoustic pressure source at the origin of the coordinate system, the wave expression at a given point is:

$$p(R, t) = A_p(\vec{R})e^{j(\omega t - \vec{k} \cdot \vec{R})}, \quad (36)$$

where $A_p(\vec{R})$ is the pressure magnitude, \vec{R} is the position vector respect to the origin, $\vec{k} = k\hat{k}$ is the wavenumber vector and \hat{k} is the propagation direction. For isotropic media $\vec{k} \cdot \vec{R} = kR$.

Then:

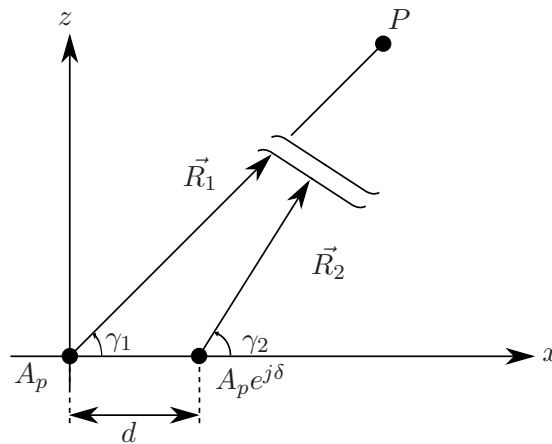
$$p(R, t) = A_p(\vec{R})e^{j(\omega t - kR)}. \quad (37)$$

The magnitude of Lamb waves in a plate decays at a rate that is proportional to the inverse square root of the propagation distance (SU; YE, 2009). Then, for a qualitative analysis of the beam generated by an array in a plate, the pressure magnitude is $A_p(\vec{R}) = A_p/\sqrt{R}$.

By considering two point sources spaced by d with same intensity and phase shift between them equal to δ , and a point P sufficiently distant from the sources (at the far field, $d \ll R$), as illustrated in Figure 10, the pressure at P due to each source is:

$$\begin{aligned} p_1(R_1, t) &= \frac{A_p}{\sqrt{R_1}} e^{j(\omega t - kR_1)} \\ p_2(R_2, t) &= \frac{A_p}{\sqrt{R_2}} e^{j(\omega t - kR_2 + \delta)}. \end{aligned} \quad (38)$$

Figure 10 – Two point sources spaced by d with same intensity and phase shift between them equal to δ . Point P is at the far field.



Source: Elaborated by the author.

In Figure 10, γ_1 and γ_2 are the angles between array axis (x) and \vec{R}_1 and \vec{R}_2 , respectively. By superposition, the pressure waves combine to each other constructively and destructively

and the resulting pressure at P is the sum of the pressure for each source:

$$\begin{aligned}
 p(R, t) &= p_1(R_1, t) + p_2(R_2, t) \\
 &= \frac{A_p}{\sqrt{R_1}} e^{j(\omega t - kR_1)} + \frac{A_p}{\sqrt{R_2}} e^{j(\omega t - kR_2 + \delta)} \\
 &= p_1(R_1, t) \left[1 + \left(\sqrt{\frac{R_1}{R_2}} \right) e^{j(kR_1 - kR_2 + \delta)} \right].
 \end{aligned} \tag{39}$$

For $d \ll R$, \vec{R}_1 and \vec{R}_2 can be considered parallel to each other, which means that:

$$\gamma_1 \approx \gamma_2 = \gamma, \tag{40}$$

where γ is the angle between array axis (x) and point P direction, and the follow approximations can be used (RUSSELL; TITLOW; BEMMEN, 1999):

$$R_2 \approx R_1, \tag{41}$$

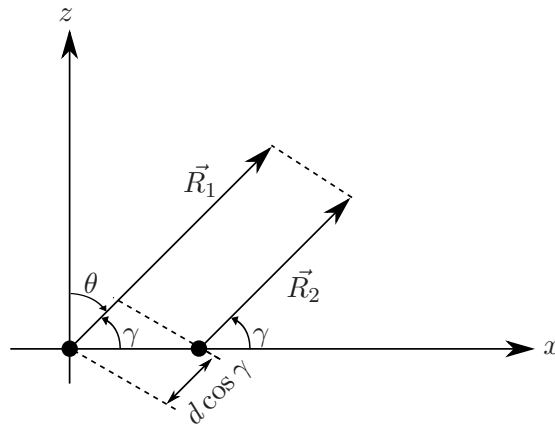
for amplitude and

$$R_2 \approx R_1 - d \cos \gamma = R_1 - d \sin \theta, \tag{42}$$

for phase argument, where θ is the complementary angle to γ , as illustrated in Figure 11. By replacing (41) and (42) in (39), the pressure is:

$$p(R, t) = p(R, t, \theta) = p_1(R, t) [1 + e^{j(kd \sin \theta + \delta)}]. \tag{43}$$

Figure 11 – Two point sources spaced by d , considering \vec{R}_1 and \vec{R}_2 parallel to each other.



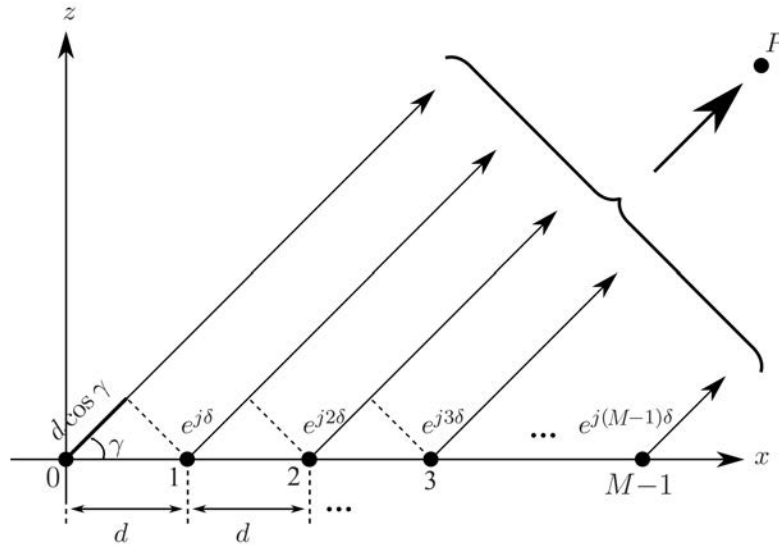
Source: Elaborated by the author.

By considering M point sources spaced by d with same intensity and phase shift between two neighboring elements equal to δ , and a point P at the far field, as illustrated in Figure 12,

the pressure at P is:

$$p(R, t, \theta) = p_1(R, t) \left[1 + e^{j(kd \sin \theta + \delta)} + e^{j2(kd \sin \theta + \delta)} + e^{j3(kd \sin \theta + \delta)} + \dots + e^{j(M-1)(kd \sin \theta + \delta)} \right], \quad (44)$$

Figure 12 – Linear array with M elements spaced by d and a point P at the far field.



Source: Elaborated by the author.

which can be written as:

$$p(R, t, \theta) = p_1(R, t) \sum_{i=0}^{M-1} e^{ji(kd \sin \theta + \delta)} = p_1(R, t) \sum_{i=0}^{M-1} e^{-j\omega_a i}, \quad \omega_a = -kd \sin \theta - \delta. \quad (45)$$

By considering different vibration intensities for each array element, (45) is rewritten as:

$$p(R, t, \theta) = p_1(R, t) \sum_{i=0}^{M-1} w[i] e^{-j\omega_a i}, \quad (46)$$

where $w[i]$ is a weight function, also known as apodization.

For $\omega_a \rightarrow 0$ and $w[i] = 1$, where $i \in [0 \ M - 1]$, the pressure wave radiated by each element arrives at P in phase and the phasor sum tends to an algebraic sum: $p(R, t, \theta) \rightarrow Mp_1(R, t)$, which represents its maximum value. By normalizing (46) respect to the maximum, the normalized pressure at P is:

$$p_{\text{norm}}(\theta) = \frac{1}{M} \sum_{i=0}^{M-1} w[i] e^{-j\omega_a i}. \quad (47)$$

By considering $w[i] = 0$ for $i \notin [0 \ M - 1]$, (47) can be written as:

$$p_{\text{norm}}(\theta) = \frac{1}{M} \sum_{i=-\infty}^{\infty} w[i] e^{-j\omega_a i}, \quad \omega_a = -kd \sin \theta - \delta, \quad (48)$$

which refers to a Discrete-Time Fourier Transform (DTFT) of $w[i]$ multiplied by $1/M$. Thus, qualitatively, the DTFT of the apodization function is equal to the radiation pattern of the linear array at the far field.

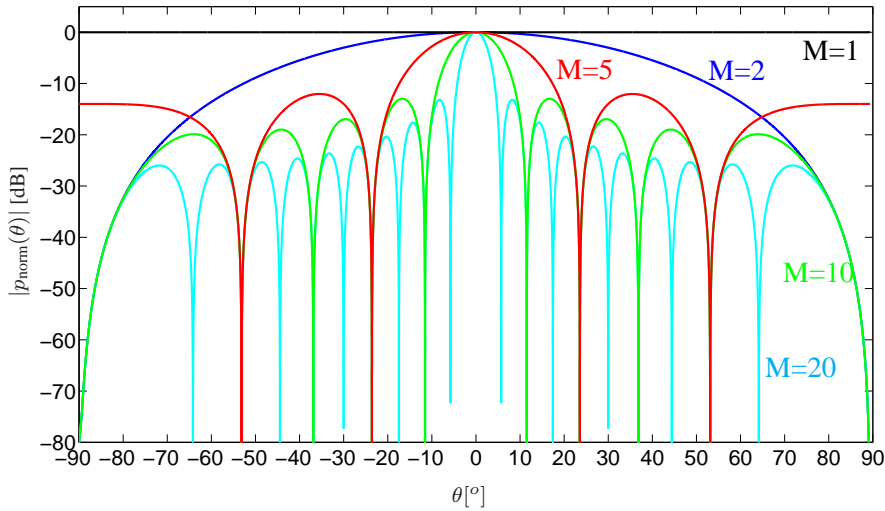
Figure 13 illustrates the radiation pattern in transmission for a linear array with M elements excited in phase ($\delta = 0 \rightarrow \omega_a = -kd \sin \theta$), spaced by $\lambda/2$, and with uniform apodization ($w[i] = 1$ for $i \in [0 \ M - 1]$). In this case:

$$p_{\text{norm}}(\theta) = \frac{e^{j[(\frac{M-1}{2})kd \sin \theta]} \sin\left(\frac{Mkd \sin \theta}{2}\right)}{M \sin\left(\frac{kd \sin \theta}{2}\right)}, \quad (49)$$

and

$$|p_{\text{norm}}(\theta)| = \left| \frac{1}{M} \frac{\sin\left(\frac{Mkd \sin \theta}{2}\right)}{\sin\left(\frac{kd \sin \theta}{2}\right)} \right|. \quad (50)$$

Figure 13 – Linear array radiation pattern in transmission for point elements and different number of elements (M).



Source: Elaborated by the author.

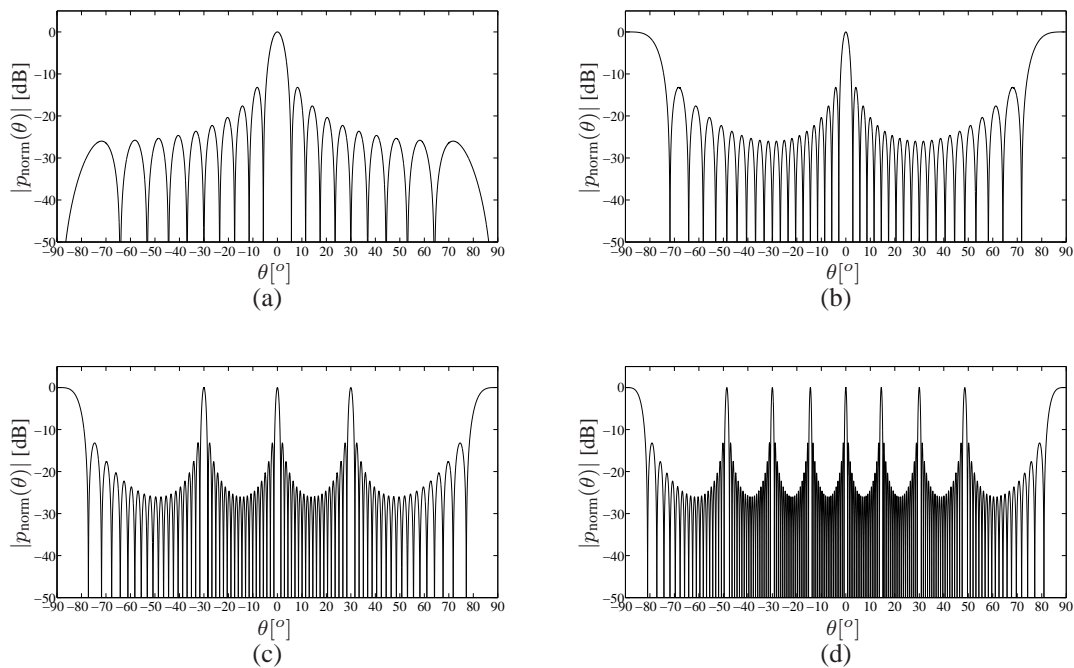
For $M = 1$ the pressure is equally transmitted in all directions, i.e. there is an isotropic source. As M increases, there is a direction that the transmission is concentrated ($\theta = 0^\circ$). For $M > 2$ there are the main and side lobes. The array directivity is higher as narrower is the main lobe, which is achieved by increasing the aperture size. The aperture size is increased by the increment of the number of elements. On the other hand the number of side lobes is also increased.

The maximum and minimum of main and side lobes are obtained by comparing the deriva-

tive of $|p_{\text{norm}}(\theta)|$ to zero. $|p_{\text{norm}}(\theta)|$ is equal to zero if its numerator is zero. In (50) there are $(M - 1)$ zeros, and then $(M - 2)$ side lobes.

Other alternative to change the aperture size is modifying the pitch value. Figure 14 presents the radiation pattern in transmission of a 20 elements linear array with different pitch values and $\delta = 0$.

Figure 14 – 20 elements linear array radiation pattern in transmission and different pitch values: (a) $d = \lambda/2$, (b) $d = \lambda$, (c) $d = 2\lambda$ and (d) $d = 4\lambda$.



Source: Elaborated by the author.

By keeping the number of elements the same and increasing the pitch, the radiation is more directive, observed by the narrow main lobe width, since the aperture size is increased. However, from a determined value, high intensities lobes appear in directions different from 0° , called grating lobes. As well as the Nyquist temporal sample theory, in which the sample frequency should be greater than twice the higher significant component of the signal, a spatial undersampling ($d > \lambda/2$) results in aliasing, normally referred as grating lobes, related to energy irradiation in directions out of the interest, which can generate wrong interpretations of inspection results.

Arrays whose elements spaced by more than $\lambda/2$ are often called sparse arrays (LOCKWOOD et al., 1996). The use of sparse arrays is interesting as the number of elements is reduced, decreasing costs in hardware, data processing and storage.

Side lobes are presented in any array configuration, since the aperture has a finite size. Grating lobes are related to the discrete and periodic nature of the element distribution and are presented in some sparse arrays configurations. Breaking the periodicity by randomly

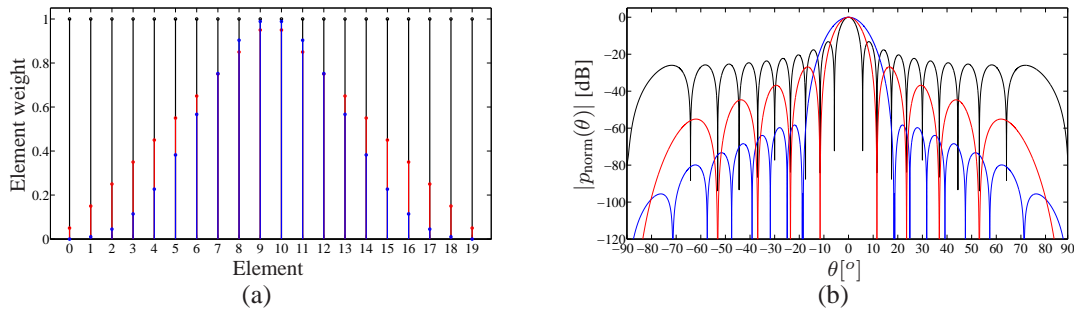
removing elements avoids the grating lobe levels (STEINBERG, 1976). Different apertures in transmission and reception (LOCKWOOD et al., 1996; LOCKWOOD; FOSTER, 1996), optimization techniques applied to elements distribution and weight (HOLM; ELGETUN; DAHL, 1997) and coherence methods (CAMACHO; PARRILLA; FRITSCH, 2009; MARTÍNEZ-GRAULLERA et al., 2011) are used to reduce the effects of grating lobes.

3.3 APODIZATION

The function $w[i]$, also known as apodization, is a weight function to change the vibration amplitudes of each element. As the DTFT of the apodization function is equal to the radiation pattern of the array, the use of different apodizations results in different radiation patterns. The apodization can be applied in the post-processing step, which means that different functions can be used for the same data set to extract the best characteristics from each one, with trade-off between main lobe width and side lobes levels (STANKWITZ; DALLAIRE; FIENUP, 1995).

Figure 15 illustrates the apodization function and the radiation pattern in transmission for a 20 elements array with $\lambda/2$ -pitch using uniform, triangular and Blackman apodizations. The uniform apodization results in the most directive radiation pattern and the Blackman results in low side lobes levels. The triangular apodization results in intermediate values between them.

Figure 15 – (a) Apodization function and (b) radiation pattern in transmission for a 20 elements array with $\lambda/2$ -pitch using uniform (black), triangular (red) and Blackman (blue) apodizations.



Source: Elaborated by the author.

3.4 FOCUSING AND BEAM STEERING

The radiation pattern has the maximum value for $\omega_a = 0$ ($\omega_a = -kd \sin \theta - \delta$), as observed in Figure 13, where $|p_{\text{norm}}(\theta)|$ is maximum for $\theta = 0^\circ$, since in phase excitation was considered ($\delta = 0$). Then, for $|p_{\text{norm}}(\theta)|$ maximum at $\theta = \theta_0$, the phase shift between two neighboring array elements should be:

$$\delta = -kd \sin \theta_0, \quad (51)$$

which can also be achieved by exciting the elements at different times.

To focus at a given point in space, the relative delay between the elements is not constant. In this case the excitation delay for each element is given by:

$$\tau_e = \frac{\sqrt{(x_f - x_a)^2 + (z_f - z_a)^2} - \sqrt{(x_f - x_e)^2 + (z_f - z_e)^2}}{c}, \quad 0 \leq e \leq M - 1, \quad (52)$$

where (x_f, z_f) is the focal point coordinate, (x_a, z_a) is the center of the array and (x_e, z_e) is the coordinate of the emitter e . This equation is valid only for an isotropic propagating medium. For anisotropic materials, the velocity value depends on the propagation direction and it must be considered.

The focus will not be a point but a region with certain depth and width, as well as single element focused transducers. The advantage of using arrays is that the focus can be dynamically modified.

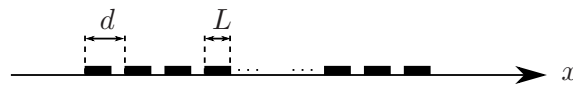
3.5 FINITE DIMENSIONS OF THE ELEMENTS

In practice the array elements are not point sources and their finite dimensions change the radiation pattern. By considering linear elements in a two-dimensional analysis, the aperture illustrated in Figure 16 can be represented by:

$$w_f(x) = w_i(x) * \sum_{i=0}^{M-1} w(x) \delta(x - id), \quad (53)$$

where $w_i(x)$ is an L -length rectangular window, representing each individual element i .

Figure 16 – Linear L -length elements array.



Source: Elaborated by the author.

By using the Fourier relation (48) and the convolution property, the radiation pattern is given by:

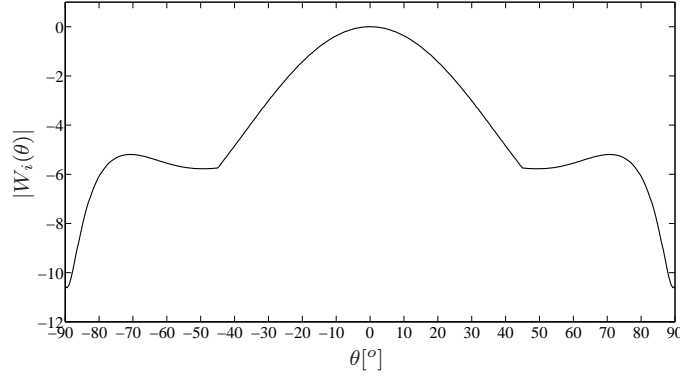
$$W_f(\theta) = W_i(\theta) \cdot W(\theta), \quad (54)$$

where $W_f(\theta)$ is the radiation pattern for a non-point elements array, $W_i(\theta)$ is the radiation pattern for a single element (non-point) and $W(\theta)$ for a point elements array. Therefore, the radiation pattern for a non-point elements array is equal to the single element radiation pattern multiplied by the one of an array composed by point elements (SCHMITZ; CHAKHLOV; MULLER, 2000).

Figure 17 illustrates the radiation pattern of a PZ26 ceramic with 0.5 mm thickness, 7 mm

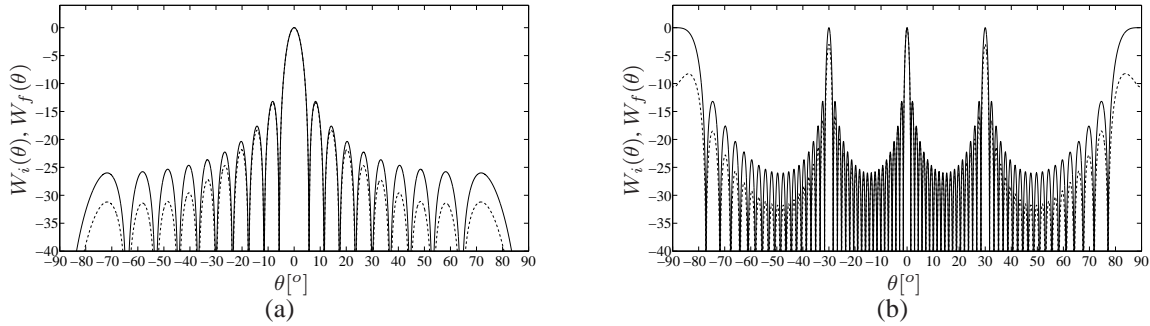
width and 6 mm length, attached to an aluminum plate at 360 kHz, which was simulated in *PZFlex*. Figures 18a and 18b present the radiation pattern by considering point sources and the simulated ceramic for a 20 elements array and pitches equal to $\lambda/2$ and 2λ . In practice (non-point elements) the side and grating lobes levels are reduced.

Figure 17 – Radiation pattern of a PZ26 ceramic with 0.5 mm thickness, 7 mm width and 6 mm length, attached to an aluminum plate at 360 kHz, simulated in *PZFlex*.



Source: Elaborated by the author.

Figure 18 – Radiation pattern of a 20 elements array by considering point sources (solid line) and the simulated ceramic (dashed line), for pitches equal to (a) $\lambda/2$ and (b) 2λ .



Source: Elaborated by the author.

3.6 COARRAY

In general the same aperture is used in transmission and reception. The two-way radiation pattern is given by the multiplication between the radiation patterns in transmission and reception (LOCKWOOD et al., 1996):

$$W_{TR}(\theta) = W_T(\theta) \cdot W_R(\theta). \quad (55)$$

By considering w_T and w_R the apertures in transmission and reception ($w_T \longleftrightarrow W_T(\theta)$ and $w_R \longleftrightarrow W_R(\theta)$), respectively, the inverse DTFT of $W_{TR}(\theta)$ is the effective aperture, or

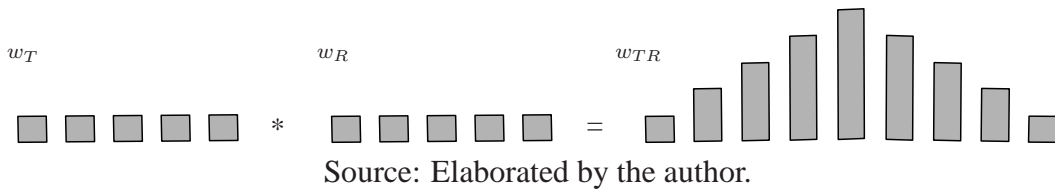
coarray, obtained by the linear convolution between transmission and reception apertures:

$$w_{TR} = w_T * w_R. \quad (56)$$

If the transmit aperture has M_T elements and the receive aperture has M_R elements, the number of elements in the coarray will be $M_T + M_R - 1$. The effective aperture of an array is simply the receive aperture that would produce an identical two-way radiation pattern if the transmit aperture were a point source (GEHLBACH; ALVAREZ, 1981; HOCTOR; KASSAM, 1990).

For an aperture with uniform apodization the coarray is the linear convolution between two rectangular apertures, resulting in an effective aperture with triangular apodization, as illustrated in Figure 19. This apodization can be further controlled by changing the weights $w[i]$ in order to obtain another radiation pattern

Figure 19 – Coarray for 5-elements rectangular apertures.



The coarray concept is very useful in image systems in many steps as the design of the system, excitation/acquisition procedure and post-processing. Lockwood et al. (1996) and Lockwood and Foster (1996), for example, avoid grating lobes in sparse arrays configurations using different element spacing in transmission and reception. Each aperture (transmission and reception) has different pitches and the coarray presents a $\lambda/2$ -pitch.

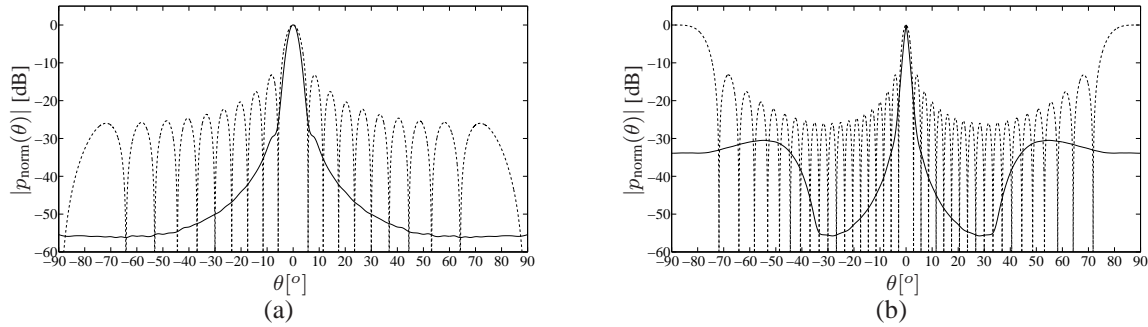
3.7 PULSED EXCITATION

An important observation is that when using harmonic signals, the time of flight as well as the excitation time can not be measured. In practice, pulsed signals are used instead of harmonic waves. The pulse duration is inversely proportional to axial resolution (SU; YE; LU, 2006). However, the shorter is the pulse duration, the higher is the bandwidth of the signal, which may be associated with increase of dispersion effects and coupling of more than one propagation mode in the case of Lamb waves.

By considering a pulsed excitation, the radiation pattern is changed, as can be observed in Figure 20, which illustrates a two-way radiation pattern for two arrays of 20 elements and pitches equal to $\lambda/2$ and λ , with continuous and pulsed excitation, considering 4-cycles with Gaussian envelope. Due to the different constructive/destructive interference for the continuous and pulsed excitation, the results in the pulsed case present side and grating lobes with lower

intensities than the lobes peaks obtained with continuous one.

Figure 20 – Two-way radiation pattern of a 20 elements array with pitch equal to (a) $\lambda/2$ and (b) λ , with continuous (dashed line) and pulsed (solid line) excitation, considering 4-cycles with Gaussian envelope.



Source: Elaborated by the author.

3.8 TWO-DIMENSIONAL ARRAYS

A two-dimensional array consists of an array with elements arranged in an area. Using bulk waves, 2D arrays are able to image the three-dimensional volume in front of it, which is used in medical applications (FENSTER; DOWNEY, 1996; BUREAU; STEICHEN; LEBAIL, 1998; TAMANO et al., 2004; SEO; YEN, 2009) and NDT (YU; GIURGIUTIU, 2008; WILCOX, 2003b; MARTÍNEZ; AKHNAK; ESPINOSA, 2003; BROTHERHOOD; DRINKWATER; FREEMANTLE, 2003; MARTÍNEZ-GRAULLERA et al., 2010). In the case of plates, the resulting image is still a 2D image of the structure. Planar arrays have the advantages of not only providing more control but also being able to improve the array beamforming with better performance, being more versatile, and being able to provide much finer beam with lower side lobes (YU; GIURGIUTIU, 2008).

In the cross-shaped array layout the elements are linearly distributed along two orthogonal directions crossing each other at the center of each axis. For the directions along the array alignments, such as 0° , $\pm 90^\circ$ and 180° , duplicated beams appear. For other directions, unique directional beams in 360° are possible, with significant side lobes levels.

Rectangular grid array allows unique directional beams at all desired directions with relatively low side lobes, when compared to the cross-shaped scheme. However, a large number of elements is needed, which is related to system complexity for data acquisition, and higher costs of processing and storage. An alternative is the use of rectangular ring array, where only the elements at the borders are used. By comparing to a rectangular array with $M_l \times M_l$ elements, there is a reduction in the number of elements from M_l^2 to $4(M_l - 1)$. Directional beamforming within 360° range can still be obtained. On the other hand, side lobes levels are significantly increased.

Circular arrays may be formed by a ring of uniformly spaced elements or by concentric rings. An array formed by a circular ring with M elements presents a radiation pattern with narrow main lobe width compared to a rectangular array with the same number of elements, since the diameter of the array is bigger than the diagonal of the rectangular one. However, the side lobes levels are higher.

The main disadvantage of 2D arrays is the large number of elements and, consequently, the electronic system complexity required to achieve an acceptable level of quality in the images (contrast, resolution, artifacts). According to Drinkwater and Wilcox (2006), the use of fewer elements randomly distributed improves the performance of the array in image formation when compared to other distribution patterns, even when the distance between the elements is increased.

Traditionally, sparse arrays have been based on the matrix distribution and there are several solutions, like periodic and random distributions (AUSTENG; HOLM, 2002; HENDRICKS, 1991), Vernier models (LOCKWOOD; FOSTER, 1996) and optimised distributions (AUSTENG et al., 1997; HOLM; ELGETUN; DAHL, 1997). Other solutions based on curved distribution of the elements, like circular or spiral (ULLATE et al., 2006; FRIDMAN, 2001; MARTÍNEZ-GRAULLERA et al., 2010) have also been proposed with better results than the square matrix array, but with a reduced impact in the audience, probably due to their complex manufacture.

Thus, in order to reduce the number of elements, 2D sparse arrays can also be used. However, besides the grating lobes and high side lobes levels, the direct signal between transmitter and receiver (due to the 2D layout) results in many artifacts throughout the image, reducing the quality of images and defects detection. To overcome this effect, a baseline can be used by subtracting the measured signals from a reference data recorded from the undamaged plate (MICHAELS; MICHAELS, 2007; LEVINE; MICHAELS, 2013), which is not always possible in practice.

3.9 COMMENTS

The use of arrays allows the inspection of the entire structure without the necessity of moving the transducers. The number of elements, the distance between them, the excitation delay, the weight (apodization) and other parameters can be changed in order to achieve the desirable radiation pattern. The coarray and DTFT properties are useful in arrays design and post-processing of the acquired data set. The radiation pattern control is important because its characteristics as main lobe width, side lobes levels, and grating lobes are directly associated with the quality of the images obtained with the array: resolution, contrast and image artifacts, as explored in chapter 4.

4 SYNTHETIC APERTURE IMAGES

In order to obtain an ultrasonic image, transducers, electronic system for transmission, reception and acquisition, as well as processing and image visualization systems are needed. The transducers work in pulse-echo and/or transmit-receive modes, generating a propagating wave in the media of interest and converting the echo signals in electrical signals, which are transferred to a computer and post-processed. By the knowledge of the propagation direction, the time of flight, and media properties, it is possible to locate reflectors and, sometimes, extract information about their sizes and shapes.

Arrays are widely used in NDT due to characteristics as beam control (beam focusing and steering, lateral resolution, apodization) and speed of test (DRINKWATER; WILCOX, 2006; YU; GIURGIUTIU, 2008). Thus, an image of a plane or volume of interest can be obtained without the necessity of moving the transducers (GÓMEZ-ULLATE, 2007).

When all array elements, or part of them, are excited simultaneously, a transmit/receive channel dedicated to each element is needed, which can reduce the time of data acquisition and process significantly. On the other hand, it increases the complexity and the cost of the system. This setup is called phased arrays (PA). PA systems allow the focusing of each point (x, z) of interest in transmission or reception and the imaging procedure from the echo signals depends on the applied focusing law.

An alternative to PAs is the use of synthetic aperture (SA) techniques, in which one or a few transmit/receive channels are multiplexed, and the data is post-processed to obtain the image (YLITALO; ERMERT, 1994). It is based on the technique of synthetic aperture radar (SAR), in which an aircraft captures several images, which are post-processed to increase the resolution, yielding a final image with a resolution equivalent to that of an antenna having the same dimensions of the aircraft displacement during the acquisitions (SHERWIN; RUINA; RAWCLIFFE, 1962). In this technique the hardware complexity is reduced, without the necessity of reducing the number of elements of the aperture. Other characteristics are: dynamic focusing in transmission and reception and the need of post-processing.

As in general the dynamics of the structure (NDT applications) is relatively slow, this type of signal acquisition and post-processing is adequate, as it is not necessary to have too many images per second. The two-way array radiation pattern is identical to the obtained with PA. However, the influence of SNR in its performance is different because in PA all elements are used in transmission while in SA only one element is used at a time.

Conventional ultrasonic images using arrays and SA techniques are obtained by the delay-

and-sum (DAS) operation on the amplitude time-domain signals. At a defect position, all delayed signals should sum in phase, resulting in a high value (positive or negative). Where there is not a defect, the amplitudes would sum randomly and lower values are expected. It has the advantage that it generates the maximum lateral resolution available at each image point.

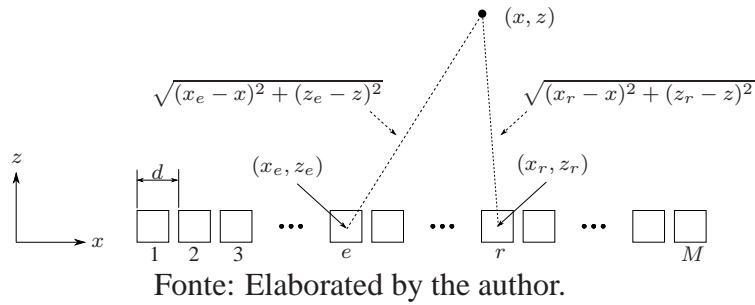
Considering a linear array of M elements and pitch d , as illustrated in Figure 21, and amplitude time-domain data $v_{er}(t)$ from all emitter e and receiver r combinations, the amplitude image value at point (x, z) can be obtained by the Total Focusing Method (TFM) (HOLMES; DRINKWATER; WILCOX, 2005):

$$I_{\text{amp}}(x, z) = \frac{1}{M^2} \sum_{e=1}^M \sum_{r=1}^M w_{er} v_{er}(\tau_{er}(x, z)), \quad (57)$$

where w_{er} is the apodization coefficient and $\tau_{er}(x, z)$ is the time of flight between the transmitter e , the point (x, z) and the receiver r , which is given by:

$$\tau_{er}(x, z) = \frac{\sqrt{(x_e - x)^2 + (z_e - z)^2} + \sqrt{(x_r - x)^2 + (z_r - z)^2}}{c_g}. \quad (58)$$

Figure 21 – Linear array with M elements, pitch d and coordinate system.



Since wideband signals are used in transmission, the group velocity (c_g) should be considered. This value is theoretically obtained from Figure 5. In practice, in the beamforming process, low-dispersive signals or dispersion compensated signals are used, which means that the group velocity is approximately equal to the phase velocity ($c_g \approx c$).

There are different SA techniques: SAFT (Synthetic Aperture Focusing Technique), which uses only the pulse-echo signals (THOMSON, 1984; KARAMAN; LI; O'DONNELL, 1995); 2R-SAFT, that considers the pulse-echo and the transmit-receive signals between two neighboring elements (MARTIN et al., 2008); and TFM (Total Focusing Method), which uses all M^2 possible emitter-receivers combinations (HOLMES; DRINKWATER; WILCOX, 2005), that is described in (57).

4.1 POINT SPREAD FUNCTION

Point Spread Function (PSF) is the image of a point reflector, i.e. it is observed how a point reflector at a certain position is visualized by the array with the proposed technique. The advantage is that contrast and resolution can be analyzed from the image. The disadvantage is that it represents just the reflector at a given region of the image.

A PSF modelling for a reflector in an aluminum plate at $x = 0$ and $z = 25$ cm was simulated in MATLAB. The signals/arrays characteristics for each simulation are described in Table 1, considering for all of them 4-cycles Gaussian envelope RF signals at 360 kHz, as illustrated in Figure 22 and point elements. A random noise with Gaussian distribution is added to the signals, resulting in a SNR of 10 dB. For each propagation mode, the velocities values were extracted from Figures 3, 4 and 5.

Table 1 – PSFs configuratons.

Configuration	M	pitch	Apodization	Mode	Dispersion compensation
<i>I</i>	16	$\lambda/2$	Triangular	S0	No
<i>II</i>	32*	$\lambda/2$	Triangular	S0	No
<i>III</i>	16	λ	Triangular	S0	No
<i>IV</i>	16	4λ	Triangular	S0	No
<i>V</i>	16	$\lambda/2$	Uniform	S0	No
<i>VI</i>	16	$\lambda/2$	Blackman	S0	No
<i>VII</i>	16	$\lambda/2$	Triangular	S0	Yes
<i>VIII</i>	16	$\lambda/2$	Triangular	A0	No
<i>IX</i>	16	$\lambda/2$	Triangular	A0	Yes

* Although it is associated with greater number of signals than the other configurations (4 times), the dynamic range used was the same for the comparison between the results.

Source: Elaborated by the author.

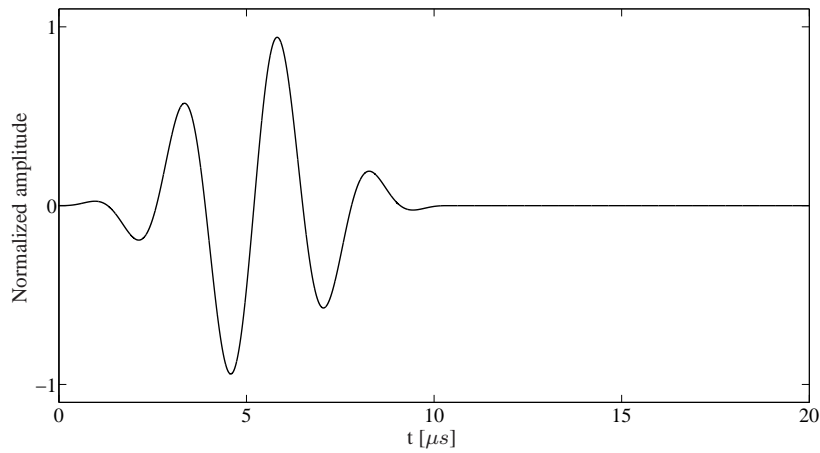
The amplitude image for configuration *I* is presented in Figures 23a and 23c. If only $v_{er}(t)$ is considered in (57), the image reproduces the oscillatory signal characteristics. By considering also the quadrature signal $\hat{v}_{er}(t)$, the envelope of the amplitude image, for example, can be obtained by:

$$I_{\text{amp-envelope}}(x, z) = \frac{1}{M^2} \left\{ \left[\sum_{e=1}^M \sum_{r=1}^M w_{er} v_{er}(\tau_{er}(x, z)) \right]^2 + \left[\sum_{e=1}^M \sum_{r=1}^M w_{er} \hat{v}_{er}(\tau_{er}(x, z)) \right]^2 \right\}^{1/2}, \quad (59)$$

where $\hat{v}_{er}(t)$ is the Hilbert transform of $v_{er}(t)$. The obtained image using the envelope is illustrated in Figures 23b and 23d. Another option to obtain the envelope is to take the image modulus and use a spatial filter, but the filter parameters are variables which can change image quality.

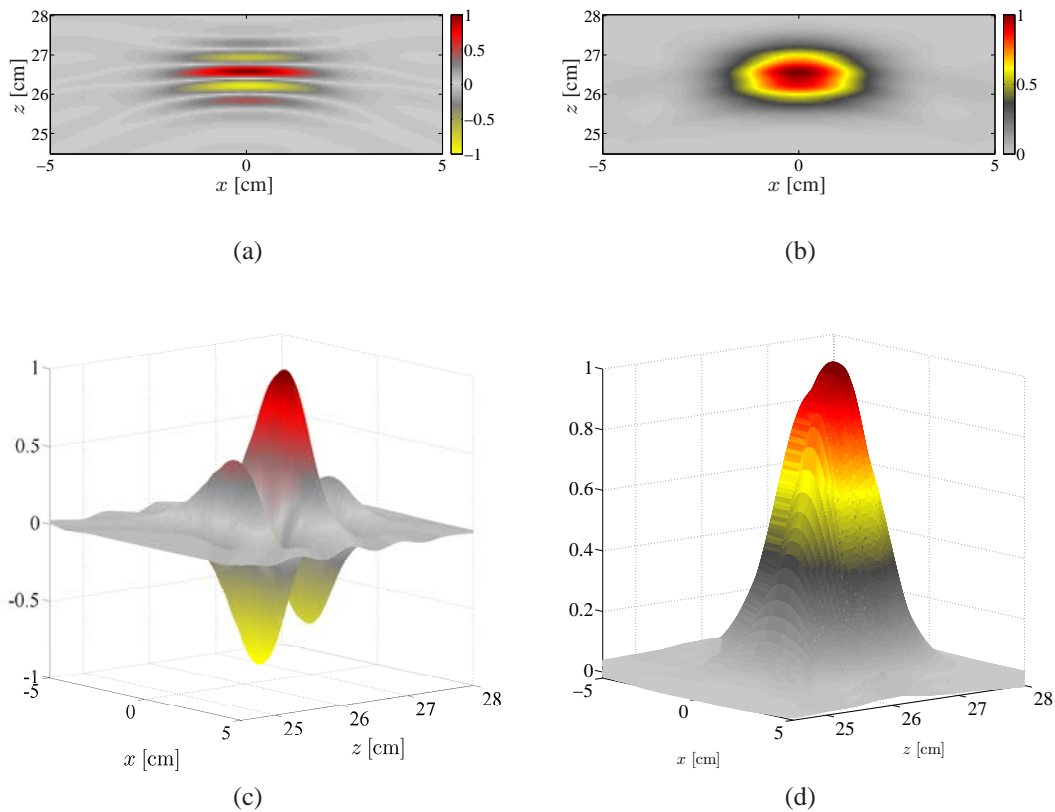
In this work, all images are illustrated in their envelope format, obtained with the in-phase

Figure 22 – Simulated 360 kHz 4-cycles amplitude signal with a Gaussian envelope without noise.



Source: Elaborated by the author.

Figure 23 – PSFs for configuration *I* described in Table 1: (a) Normalized RF amplitude image, (b) envelope amplitude image, and 3D view of (c) RF and (d) envelope images. Linear scales.



Source: Elaborated by the author.

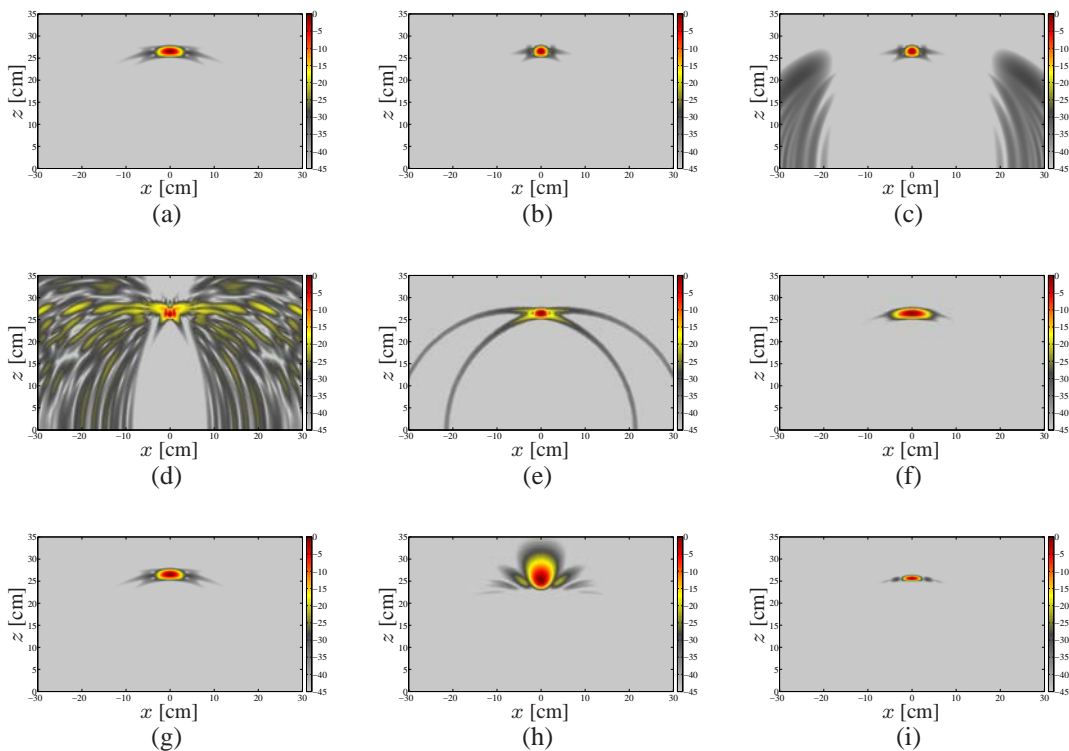
and quadrature signals, except those of Figures 23a and 23c. And also except for those related to Figure 23, all images referred as amplitude images are obtained using (59).

The excitation signal format, illustrated in Figure 22, can be observed in Figures 23a and 23c, by considering a line along z direction at $x = 0$ cm, starting at the reflector position (0, 25) cm. The same occurs with the signal envelope in Figures 23b and 23d. Then, even a point reflector is represented by a finite area in the image after beamforming, due to array and excitation signal characteristics, which means that there are resolution limitations.

Lateral resolution is limited by the main lobe width, which in turn depends on the aperture size respect to the wavelength and the apodization (JENSEN et al., 2006). Axial resolution is limited by the pulse duration and propagation velocity, i.e. depends on the wavelength and the number of cycles. For the simulated cases, 4-cycles signals with central frequency of 360 kHz were considered. The S0 mode wavelength is equal to 1.50 cm and the A0 mode 0.75 cm. The reflector size (in the image) in this direction is then determined by the number of cycles multiplied by $\lambda/2$: 3.00 cm for S0 mode and 1.50 cm for A0 mode.

The obtained images for all configurations are illustrated in Figure 24, with dynamic range defined here as $[20\log_{10}(1/M_s), 0]$, approximately $[-45, 0]$ in dB, where M_s is the number of signals used for imaging, which is equal to M^2 for the TFM method.

Figure 24 – PSFs for configurations described in Table 1 (a) *I* - standard configuration (16 elements, $\lambda/2$ -pitch, triangular apodization, S0 mode without dispersion compensation), and results after changes in parameters: (b) *II* - 32 elements, (c) *III* - λ -pitch, (d) *IV* - 4λ -pitch, (e) *V* - uniform apodization, (f) *VI* - Blackman apodization, (g) *VII* - S0 mode with dispersion compensation, (h) *VIII* - A0 mode without dispersion compensation and (i) *IX* - A0 mode with dispersion compensation. Scales in dB.



Source: Elaborated by the author.

By comparing configurations *I* to *II*, which are illustrated in Figures 24a and 24b, it is possible to observe that the higher is the number of elements, for the same pitch value, smaller is the reflector representation size in x direction and, consequently, higher is the lateral resolution, which was expected due to the increase of the aperture size (reducing the main lobe width). Figure 24c presents the result for configuration *III*, which was obtained by an array with the same aperture size, but doubled pitch (higher than $\lambda/2$). Thus, the same reflector size is observed, but also image artifacts due to grating lobes are presented. By increasing even more the pitch value, the lateral resolution is improved (increasing the aperture size). In contrast, more image artifacts are observed, due to grating lobes, as illustrated in Figure 24d.

The effects of apodization can be observed in Figures 24a, 24e and 24f, which simulates configurations *I*, *V* and *VI*, respectively. As expected, the uniform apodization is related to narrower main lobe width and higher side lobes levels. The Blackman apodization is associated with low side lobes levels, but the high main lobe width results in a large defect representation. The triangular one results in intermediate values between all compared cases.

Figure 24g illustrates the result of the dispersion compensation for the S_0 mode, which presents low dispersive characteristic at the simulated band of frequencies. By comparing it with Figure 24a, there are no significant improvements after dispersion compensation. However the A_0 mode presents high dispersion and without the dispersion compensation the reflector representation shape is changed, as illustrated in Figure 24h, due to dispersion in the propagated time-domain signal, previously observed in Figure 6. The higher is the propagated distance, more significant is the dispersion effects, especially in a practical case, where there are also other reflections simultaneously, which difficult the interpretation of the results compared to the real case, as presented in chapter 6.

By compensating the dispersion, its effects are reduced, as can be observed in Figure 24i. Besides the correction in the reflector representation shape, its size is also changed in z direction, which is not related to dispersion, but to the lower A_0 wavelength respect to the S_0 one, as commented before.

4.2 COMMENTS

This chapter introduced the ultrasonic image concept by the synthetic aperture technique, presenting all the equations needed to beamforming from the amplitude time-domain signals related to the echo data. Point spread functions were simulated for different configurations to observe the compromise between radiation pattern, presented in chapter 3, and reflector representation in an image. By changing the radiation pattern (number of elements, pitch, apodization) the main and side lobes are also modified, as well as the presence of grating lobes, which are related to lateral resolution (reflector size), contrast (difference between main and side lobes

levels) and image artifacts. The effect of dispersion compensation for low and high dispersive signals, for S0 and A0 modes, respectively, was also illustrated. In the first case the dispersion compensation does not result in significant improvements, but in the last case the compensation is necessary for correct reflector representation, which is presented in a practical case in chapter 6. The choice of parameters values to be used, such as the apodization function, the number of elements and pitch, and the use or not of dispersion compensation technique, depends on the trade-off between quality of the image and cost of the system. For example: the greater is the number of elements, larger is the aperture size, resulting in a more directive array, which is related to better lateral resolution. However, the cost and complexity of the system increases, because the number of multiplexer channels, as well as memory to store the waveforms, must be expanded.

5 PROPOSED TECHNIQUES

Coherence imaging and image compounding methods are powerful techniques since they extract different information from the data set to improve image quality without increasing the cost and complexity of the system.

Conventional SA images are obtained by the DAS operation on the amplitude time-domain signals, but the individual signals can present low SNR, resulting in a limitation in detecting reflectors or objects that are far from the array. In addition to this, the use of the phase of the signals, which carries important information (OPPENHEIM; LIM, 1981), can result in more accurate indication of reflectors or can be used as a coherence factor to improve the quality of images.

The study of the coherence of the energy balance at each point of the image to improve the beamforming process was proposed by Hollman, Rigby and O'Donnell (1999) and employed in adaptive beamforming process by Asl and Mahloojifar (2009). The introduction of the analysis of the phase in the beamforming can be based on many descriptors with different degrees of computational complexity but with similar results as the polarity and the variance of the distribution of phases (CAMACHO; PARRILLA; FRITSCH, 2009), or the spectral analysis of the phase distribution (MARTÍNEZ-GRAULLERA et al., 2011), showing a high degree of robustness to noise, side and grating lobes.

Traditionally, the coherence images are used as weighting factors, that are multiplied by amplitude images, resulting in contrast and dynamic range improvements, and reduction of image artifacts due to side and grating lobes. Although there are significant improvements, the quality of images can still be limited by main lobe width (resolution), high side and grating lobes levels (contrast and image artifacts) and Lamb mode sensitivity. Each mode is more or less sensitive to specific types of defects, like notches, delamination and surface defects. Alleyne and Cawley (1992a) studied some interactions of Lamb waves with defects and the results show that the sensitivity of individual Lamb modes to a particular defect is dependent on defect geometry, frequency-thickness product, mode type (symmetric or antisymmetric) and mode order. For example, the S0 mode exhibits reasonable sensitivity to defects anywhere in the thickness, while the A0 mode is more sensitive to surface cracks or corrosion (SU; YE; LU, 2006). Then an image compounding technique to consider the Lamb mode diversity is proposed.

Michaels and Michaels (2007) presented a fusion technique to detect damage in plates by taking the minimum value of all images for a given pixel. The minimum value can result in non-detection of a reflector if it is not represented in at least one image. By the use of the

maximum of all images, artifacts in some of them would be considered reflectors in the final image. Davies and Cawley (2007) obtained a compounded image by summing all images.

An intermediate result related to the selection of the minimum and maximum of two or more images is proposed by Higuti et al. (2010), using a coherence image to select the maximum or the minimum of the amplitude images obtained with two arrays with different apodizations. The selection is done by applying a 70% threshold to a coherence image, pixel by pixel, and if the pixel intensity is above threshold, it is considered a reflector, and the maximum between the images is taken. If it is below threshold, the minimum is selected.

The threshold is not used only in fusion techniques. Holmes, Drinkwater and Wilcox (2005) defined a -6 dB threshold value respect to the maximum image value, to create a parameter to measure array performance. Michaels et al. (2014) also considered a -6 dB threshold, which was used to indicate the presence of defects. Yu and Giurgiutiu (2008) used an 80% threshold that was applied to an amplitude image, resulting in a binary image. This is then multiplied by the original amplitude image to reduce side lobes influence and background noise.

Therefore, a threshold can be applied to the image pixels (amplitude or coherence images), which can be used to indicate the presence of a reflector, as well as to create a weighting image. If the image pixel intensity is above threshold, there is a probability that it is related to a reflector. The threshold level is a parameter that controls the sensitivity of the methods, but its value is in general defined in a subjective way, for example as a certain percentage of the maximum, and can depend on the application and experimental conditions. The improper choice of threshold value can result in wrong interpretations of the object under inspection. A high threshold value would increase contrast of some reflectors, but reflectors that generate small signals, due to intrinsic characteristics of the defect, or to attenuation or diffraction in the propagation path, as well as low SNR, could be discarded. A low threshold can result in many artifacts in the two-level image, because small amplitude pixels due to noise can be above threshold and consequently contrast is decreased.

Then, two techniques are proposed in this thesis: (i) the instantaneous phase (IP) image and (ii) the Lamb mode diversity compounding technique. The first uses the IP of the signals to obtain an SA image, instead of using the amplitude of the signals in the DAS technique. The resulting IP image is very similar to the ones obtained with coherence factors (CAMACHO; PARRILLA; FRITSCH, 2009; MARTÍNEZ-GRAULLERA et al., 2011; CAMACHO; FRITSCH, 2011). The main contribution of the proposed method is the definition of an objective threshold level that is applied to the IP image, based on a statistical analysis of noise and the number of signals used in beamforming. The thresholded IP image can then be used to directly indicate the presence of a reflector, to create a weighting factor for amplitude images, and as a selection parameter to use in method (ii), which in turn is an image compounding technique to consider the different interaction between propagation modes and defects.

5.1 INSTANTANEOUS PHASE IMAGE

The IP image is obtained by replacing the signal $v_{er}(t)$ by its instantaneous phase $\varphi_{er}(t)$ in (57):

$$I_{\varphi}(x, z) = \frac{1}{M^2} \sum_{e=1}^M \sum_{r=1}^M \varphi_{er}(\tau_{er}(x, z)). \quad (60)$$

The instantaneous phase of $v_{er}(t)$ is given by (OPPENHEIM; SCHAFER; BUCK, 1999):

$$\varphi_{er}(t) = \arctan \left\{ \frac{\hat{v}_{er}(t)}{v_{er}(t)} \right\}. \quad (61)$$

Although (60) and further equations are defined only with the in-phase signals, in this work the IP images are also related to the envelope format, obtained with the in-phase and quadrature signals, which are obtained replacing $v_{er}(t)$ by $\varphi_{er}(t)$ and $\hat{v}_{er}(t)$ by $\hat{\varphi}_{er}(t)$ (the instantaneous phase of $\hat{v}_{er}(t)$) in (59). Then, the IP image obtained with the in-phase and quadrature signals is:

$$I_{\varphi\text{-envelope}}(x, z) = \frac{1}{M^2} \left\{ \left[\sum_{e=1}^M \sum_{r=1}^M \varphi_{er}(\tau_{er}(x, z)) \right]^2 + \left[\sum_{e=1}^M \sum_{r=1}^M \hat{\varphi}_{er}(\tau_{er}(x, z)) \right]^2 \right\}^{1/2}. \quad (62)$$

5.1.1 Analysis of the instantaneous phase image

By considering the propagation of a harmonic acoustic pressure pulsed wave, the signal at the receiver point is:

$$v(t) = s(t) + n(t), \quad (63)$$

where $s(t)$ contains the reflected signals from defects and interfaces without noise, and $n(t)$ is an additive white Gaussian noise (AWGN), physically independent of the signal and therefore uncorrelated with it. The measured signal $s(t)$ without noise is in general bandlimited and can be written in envelope-and-phase form as:

$$s(t) = \Re \{ S(t) e^{j\phi(t)} \}, \quad (64)$$

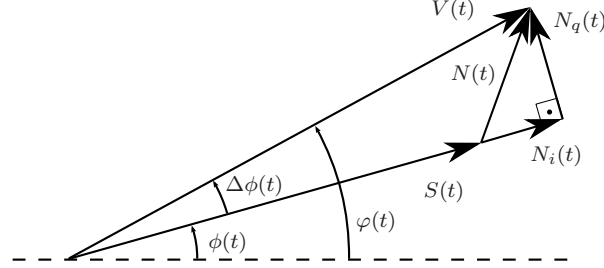
where $\Re \{ \cdot \}$ is the real operator, $S(t)$ is the envelope and $\phi(t)$ is the instantaneous phase of $s(t)$.

In the presence of a reflector and considering the in-phase/quadrature description of the noise $n(t)$ respect to $s(t)$, (63) can be represented by the phasor diagram of Figure 25, where $N(t)$ is the envelope of $n(t)$, and written as:

$$\begin{aligned} v(t) &= \Re \{ [S(t) + N_i(t)] e^{j\phi(t)} + N_q(t) e^{j(\phi(t) + \pi/2)} \} \\ &= \Re \{ V(t) e^{j\varphi(t)} \}, \end{aligned} \quad (65)$$

where $N_i(t)$ is the in-phase and $N_q(t)$ is the quadrature components of $n(t)$ respect to $s(t)$. These components are jointly stationary, so they are independent and Gaussian, like $n(t)$.

Figure 25 – Phasor diagram of $v(t)$.



Source: (CARLSON; CRILLY, 2009).

The envelope of $v(t)$ is:

$$V(t) = \sqrt{[S(t) + N_i(t)]^2 + [N_q(t)]^2}, \quad (66)$$

and the instantaneous phase of $v(t)$ is:

$$\varphi(t) = \phi(t) + \Delta\phi(t), \quad (67)$$

where

$$\Delta\phi(t) = \arctan \left\{ \frac{N_q(t)}{S(t) + N_i(t)} \right\}. \quad (68)$$

The instantaneous phase of $s(t)$ is:

$$\phi(t) = \phi(t, R) = \omega t - \vec{k} \cdot \vec{R} + \phi_0, \quad (69)$$

where ϕ_0 is the initial phase.

By replacing (69) in (67), the instantaneous phase of $v(t)$ is:

$$\varphi(t) = \varphi(t, R) = \omega t - \vec{k} \cdot \vec{R} + \phi_0 + \Delta\phi(t). \quad (70)$$

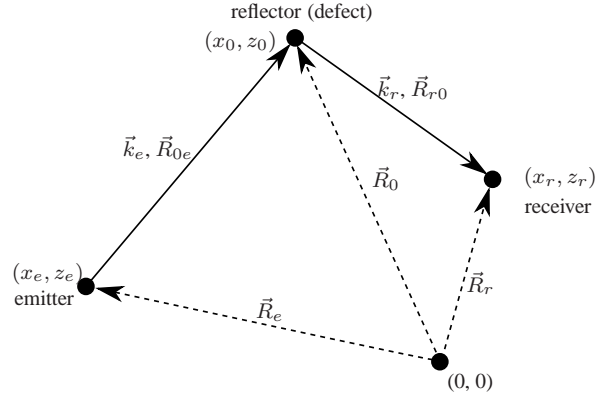
Supposing that the wave propagates the path from the transmitter at (x_e, z_e) to the reflector at (x_0, z_0) and back to the receiver at (x_r, z_r) , as illustrated in Figure 26, the instantaneous phase measured at the receiver can be written as:

$$\begin{aligned} \varphi_{er}(t, R) &= \omega t - \vec{k}_e \cdot (\vec{R}_0 - \vec{R}_e) - \vec{k}_r \cdot (\vec{R}_r - \vec{R}_0) \\ &\quad + \phi_{0,er} + \Delta\phi_{er}(t) \\ &= \omega t - \vec{k}_e \cdot \vec{R}_{0e} - \vec{k}_r \cdot \vec{R}_{r0} + \phi_{0,er} + \Delta\phi_{er}(t) \\ &= \omega t - k_e R_{0e} - k_r R_{r0} + \phi_{0,er} + \Delta\phi_{er}(t), \end{aligned} \quad (71)$$

as \vec{k}_e is parallel to $\vec{R}_{0e} = \vec{R}_0 - \vec{R}_e$ and \vec{k}_r is parallel to $\vec{R}_{r0} = \vec{R}_r - \vec{R}_0$, as schematically depicted

in Figure 26.

Figure 26 – Position and propagation vectors of a pressure wavefront generated in the point (x_e, z_e) , reflected in (x_0, z_0) and measured in (x_r, z_r) .



Source: Elaborated by the author.

By considering an isotropic propagating medium with no dispersion (or considering the data set after dispersion compensation), the group velocity is equal to the phase velocity ($c_g = c$), $k_e = k_r = k$, and $k = \omega/c = \omega/c_g$. Then (71) becomes:

$$\begin{aligned} \varphi_{er}(t, R) &= \omega t - k(R_{0e} + R_{r0}) + \phi_{0,er} + \Delta\phi_{er}(t) \\ &= \omega t - \omega \frac{(R_{0e} + R_{r0})}{c_g} + \phi_{0,er} + \Delta\phi_{er}(t) \\ &= \omega t - \omega\tau_{er}(x, z) + \phi_{0,er} + \Delta\phi_{er}(t), \end{aligned} \quad (72)$$

where $\tau_{er}(x, z) = (R_{0e} + R_{r0})/c_g$. For each image point (x, z) , the signal is summed at $t = \tau_{er}(x, z)$ for each emitter-receiver combination, which is represented in (60), and then (72) results in:

$$\varphi_{er}(\tau_{er}(x_0, z_0), R) = \phi_{0,er} + \Delta\phi_{er}(\tau_{er}(x_0, z_0)). \quad (73)$$

If the same function is used to excite all transmitters, then $\phi_{0,er} = \phi_0$ for all M^2 transmitter-receiver combinations. Consequently, by replacing (73) in (60), the IP image at the reflector point is:

$$I_\varphi(x_0, z_0) = \phi_0 + I_{\Delta\phi}(x_0, z_0), \quad (74)$$

where

$$I_{\Delta\phi}(x, z) = \frac{1}{M^2} \sum_{e=1}^M \sum_{r=1}^M \Delta\phi_{er}(\tau_{er}(x, z)). \quad (75)$$

When there is not a defect at (x_0, z_0) , the measured signal consists only of noise $n(t)$, with instantaneous phase $\phi_n(t)$, which has uniform distribution over 2π rad (CARLSON; CRILLY, 2009). In this case the IP image is:

$$I_\varphi(x_0, z_0) = I_{\text{noise}}(x_0, z_0), \quad (76)$$

where

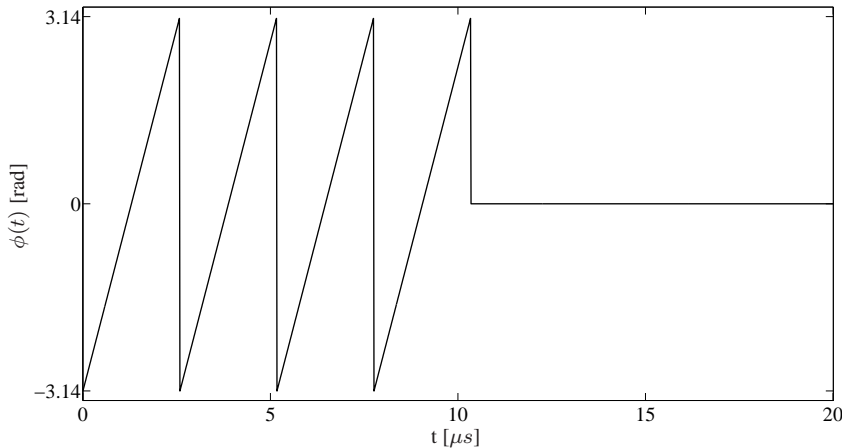
$$I_{\text{noise}}(x, z) = \frac{1}{M^2} \sum_{e=1}^M \sum_{r=1}^M \phi_n(\tau_{er}(x, z)). \quad (77)$$

Thereby, the IP image can be written as:

$$I_{\varphi}(x, z) = \begin{cases} \phi_0 + I_{\Delta\phi}(x, z), & \text{if there is a reflector} \\ I_{\text{noise}}(x, z), & \text{otherwise} \end{cases}. \quad (78)$$

As observed in Figures 23a and 23c, the excitation signal shape can be observed in the amplitude image by considering a line along z direction at $x = 0$ cm, starting at the reflector position. A similar result is observed in the IP image, obtaining by using (60). The instantaneous phase of the signal illustrated in Figure 22 can be observed in Figure 27 and the IP PSF obtained using this information (60) is illustrated in Figure 28. Then the instantaneous phase of the excitation signal is contained in a line of the image along z direction at $x = 0$ cm, starting at the reflector position, whose pixel value would be equal to the initial phase $\phi_0 = -\pi$ rad. However, independently of this value, the reflector is represented by a finite area with pixels values between $\pm\pi$ rad. By considering the envelope format, the reflector region pixels values are between 0 and π rad.

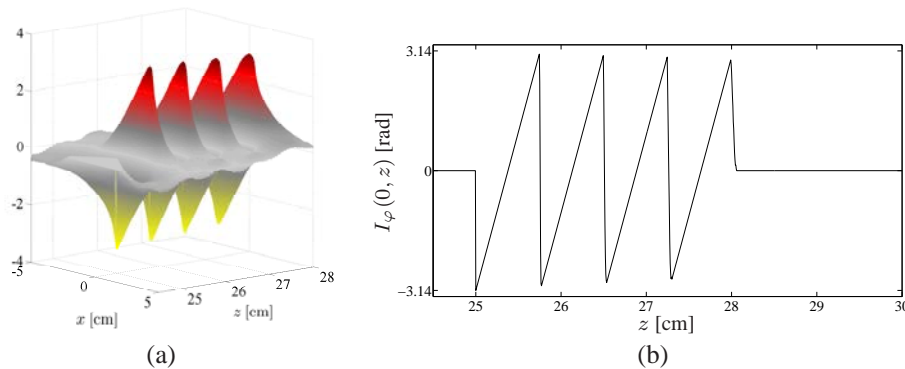
Figure 27 – Instantaneous phase of a simulated 360 kHz 4-cycles amplitude signal with a Gaussian envelope without noise.



Source: Elaborated by the author.

The term $I_{\Delta\phi}(x, z)$ in (78) is related to the average of $\Delta\phi(t)$, which according to (68), depends on noise $n(t)$. In order to determine if the pixels are related to a reflector or noise, the SNR should be considered.

Figure 28 – IP PSF for configuration *I* described in Table 1: (a) 3D view of RF IP image and (b) axial view at $x = 0$ cm. Linear scales in rad.



Source: Elaborated by the author.

5.1.2 Signal-to-noise ratio analysis

By considering $\text{SNR} \gg 1$, $S(t) \gg N_i(t)$ and $S(t) \gg N_q(t)$ most of the time, the small-argument approximation for the inverse tangent function in (68) can be used, resulting in:

$$\Delta\phi(t) \approx \frac{N_q(t)}{S(t)}. \quad (79)$$

Since the signal is summed in phase and the noise is randomly summed for all M^2 signals in (75), in the presence of a reflector at (x_0, z_0) , $\Delta\phi(t) \approx 0$, and the following approximation is valid:

$$I_\varphi(x_0, z_0) \approx \phi_0, \quad \text{if } \text{SNR} \gg 1, \quad (80)$$

and the image will have a region with pixels varying from 0 to π rad in the reflector vicinity.

For $\text{SNR} \ll 1$, the phasor diagram is changed, as shown in Figure 29 and the instantaneous phase of $v(t)$ is:

$$\varphi(t) = \phi_n(t) + \Delta\phi_s(t), \quad (81)$$

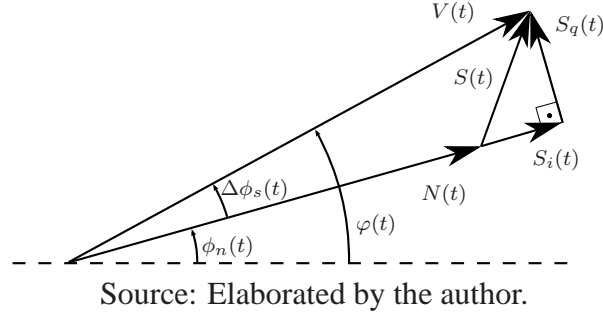
where

$$\Delta\phi_s(t) = \arctan \left\{ \frac{S_q(t)}{N(t) + S_i(t)} \right\}, \quad (82)$$

and $S_i(t)$ and $S_q(t)$ are the in-phase and quadrature components of $s(t)$ respect to $n(t)$, respectively.

Since $N(t) \gg S_i(t)$ and $N(t) \gg S_q(t)$ most of the time, again the small-argument approximation for the inverse tangent function can be used and (82) is approximately:

$$\Delta\phi_s(t) \approx \frac{S_q(t)}{N(t)}. \quad (83)$$

Figure 29 – Phasor diagram of $v(t)$ for $\text{SNR} \ll 1$.

Equation (74) is rewritten as:

$$I_\varphi(x, z) = I_{\text{noise}}(x, z) + I_{\Delta\phi_s}(x, z), \quad (84)$$

where $I_{\Delta\phi_s}(x, z)$ is obtained by replacing $\Delta\phi(t)$ by $\Delta\phi_s(t)$ in (75).

Therefore, if there is a reflector at (x_0, z_0) , the IP image at this point can be approximated by:

$$I_\varphi(x_0, z_0) \approx \begin{cases} \phi_0, & \text{if } \text{SNR} \gg 1 \\ I_{\text{noise}}(x_0, z_0) + I_{\Delta\phi_s}(x_0, z_0), & \text{if } \text{SNR} \ll 1 \end{cases}, \quad (85)$$

and if there is not a reflector at (x_0, z_0) :

$$I_\varphi(x_0, z_0) = I_{\text{noise}}(x_0, z_0). \quad (86)$$

As commented, the reflector is visualized as a set of pixels varying between 0 and π rad (plus noise), starting at the reflector position, even for a point reflector. From the analysis of the IP image and with a prior knowledge of noise, a discrimination between reflector and noise can be done for each image pixel, by the use of a threshold, as presented in next section.

5.1.3 Threshold based on the instantaneous phase image

If X_1, X_2, \dots, X_{M_s} are sample values obtained from M_s independent observations of a random variable X having mean m_X and variance σ_X^2 , the sum $Z = X_1 + X_2 + \dots + X_{M_s}$ has mean $\mu = Z/M_s$ and variance $M_s\sigma_X^2$ (CARLSON; CRILLY, 2009). Furthermore, from Chebyshev's inequality, the probability that μ differs from m_X by less than some positive amount ϵ is lower-bounded by:

$$P(|\mu - m_X| \leq \epsilon) \geq 1 - \frac{\sigma_X^2}{M_s\epsilon^2}. \quad (87)$$

In the absence of a reflector, $I_\varphi(x, z) = I_{\text{noise}}(x, z)$. The noise component, described in (77) is related to an average of ϕ_n , which is a random variable with uniform distribution between $-\pi$ rad and π rad, expected value equal to zero and standard deviation $\sigma_0 = \pi/\sqrt{3}$ rad. By

replacing these values in Chebyshev's inequality, $m_X = 0$, $\mu = I_\varphi(x, z)$, $\sigma_X^2 = \sigma_0^2$ and $M_s = M^2$, which is the number of signals used for imaging, (87) is rewritten as:

$$P(|I_\varphi(x, z)| \leq \epsilon) \geq 1 - P_E, \quad (88)$$

where

$$P_E = \frac{\sigma_0^2}{M_s \epsilon^2} \quad (89)$$

is the probability of error, or of false indication of a reflector.

At this point the threshold ϵ is defined. The pixel value is considered due to, or part of, a reflector, if $|I_\varphi(x, z)|$ (or its envelope, in practice) is above threshold, and noise if it is below. In the absence of a reflector $I_\varphi(x, z) = I_{\text{noise}}(x, z)$, with probability of $P_E \times 100\%$ to be considered a reflector (false indication).

One could arbitrarily choose a value for P_E equal to 0.01, 0.05, 0.10, 0.20, for example, but this value should depend on the number of signals used in beamforming, leading to a well-defined criterion for the determination of the threshold. The greater is the number of signals used for imaging, more μ tends to m_X and smaller is the value of P_E . On the other hand, for smaller values of M_s , the value of P_E increases.

Since the variance is a measure of the dispersion of a set of data points around their mean value, and the image is obtained from the average of M_s values, P_E is defined as a function of the variance of the mean σ_0^2/M_s . Furthermore, low values of P_E are desired for arrays with any number of elements. By considering arrays with 8 to 128 elements, for example, the number of signals used in beamforming can go from 64 to 16384. Due to this large range, a logarithmic dependence on M_s is proposed:

$$P_E \triangleq \frac{\sigma_0^2}{M_s} \log_{10} M_s. \quad (90)$$

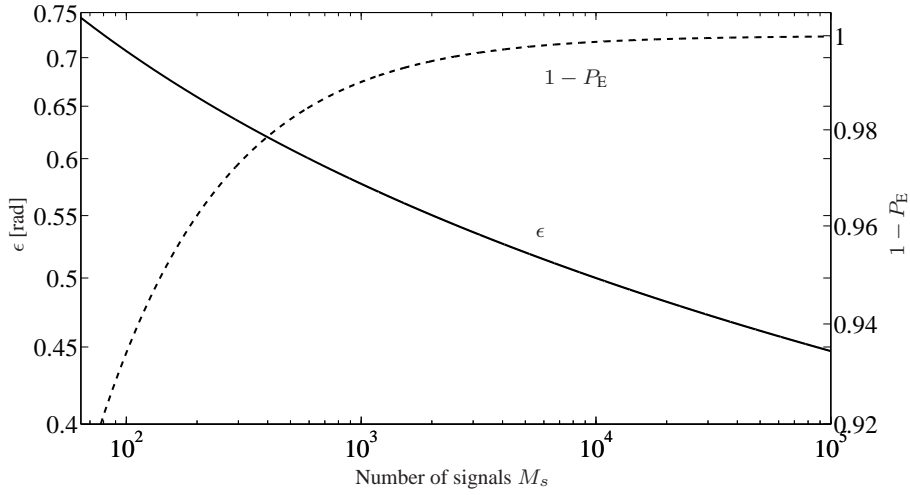
If P_E was only equal σ_0^2/M_s , by comparing to (89), the threshold would be equal to 1 rad for any M_s value, but a threshold based on the number of signals is expected. So, by comparing (90) to (89), the threshold is defined by:

$$\epsilon \triangleq \frac{1}{\sqrt{\log_{10} M_s}}. \quad (91)$$

Therefore, the proposed threshold value depends only on the number of signals used in beamforming, without previous knowledge of the media, such as attenuation characteristics.

Values of ϵ and $(1 - P_E)$ as a function of the number of signals M_s (from 64 to 10^5), are shown in Figure 30, by using $\sigma_0 = \pi/\sqrt{3}$ rad. As expected, the smaller is the number of signals, smaller is the value of $(1 - P_E)$ and higher is the threshold value ϵ that the image pixel must exceed in order to be considered a reflector, since there is greater influence of noise.

Figure 30 – Values of ϵ (solid line, left vertical axis) and $(1 - P_E)$ (dashed line, right vertical axis) as functions of the number of signals M_s .



Source: Elaborated by the author.

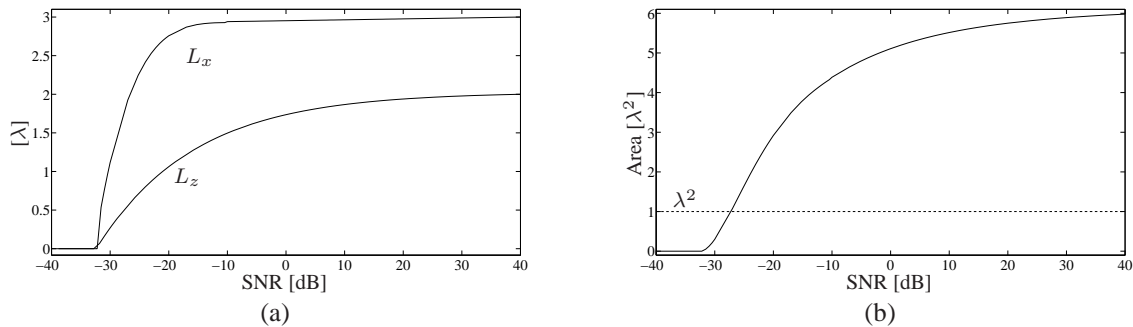
For $\text{SNR} \gg 1$, a reflector is detected if the condition $|I_\varphi(x, z)| > \epsilon$ is satisfied. If the signal of Figure 22 is used in transmission, values between 0 and π rad are expected in the vicinity of the reflector, and values close to zero otherwise. In the worst case of a two-elements array, $M_s = 4$ and $\epsilon = 1.29$ rad, which is less than π rad, so the proposed threshold is always valid, since some pixels related to the reflector will be greater than the threshold value.

The critical situation occurs when $\text{SNR} \ll 1$, since $I_\varphi(x, z)$ depends on $I_{\text{noise}}(x, z)$ and $I_{\Delta\phi_s}(x, z)$, which in turn depends on the noise magnitude and the quadrature component of the signal respect to noise, that is not easy to predict. Then, an empirical analysis of the influence of SNR on the proposed threshold was conducted.

PSF images of a reflector 25 cm away from an array with $M = 16$ elements ($M_s = 256$) and $\lambda/2$ -pitch at 360 kHz in an aluminum plate and S0 mode ($\lambda = 1.5$ cm) were simulated. AWGN is added to the excitation signal of Figure 22, resulting in SNRs from -40 dB to 40 dB. The threshold, in this case, is $\epsilon = 0.6482$ rad, which is applied to the IP image, resulting in two-level images, whose pixels assume 1 if they are above threshold and 0 otherwise. As observed in Figure 23, even a point reflector is represented by a finite set of pixels that exceed threshold. The reflector representations in the thresholded IP images are related to a finite area which can be used to evaluate defect detection. By the simulated results, width L_x , length L_z and area $L_x \times L_z$ were obtained as a function of SNR (for this particular array and excitation function) and presented in Figure 31, in units of wavelength. If the area is at least λ^2 , then these pixels will be considered part or due to a reflector.

As shown in Figure 31a, the reflector representation dimensions reach constants values for high SNRs. The lateral size L_x , whose value depends on the aperture size and frequency, presents a rapid decrease for SNR below -20 dB. The axial size L_z shows a smaller slope with

Figure 31 – Obtained (a) width L_x and length L_z , and (b) area of the reflector representation as functions of SNR. The threshold of the minimum reflector area (λ^2) is presented in dashed line.



Source: Elaborated by the author.

SNR, and depends on the excitation signal and transducer characteristics (in the simulations, the excitation signal is the transmitted signal, for simplicity). The estimated area, that is illustrated in Figure 31b, is equal to λ^2 for SNR = -27 dB, which is then considered the minimum SNR of operation for this array and excitation function.

As tested by the author, by decreasing the number of elements and maintaining all other parameters unchanged, as pitch and frequency, the minimum SNR of operation is increased, as expected. For an eight-elements array, the point reflector is detected for SNR greater than -15 dB.

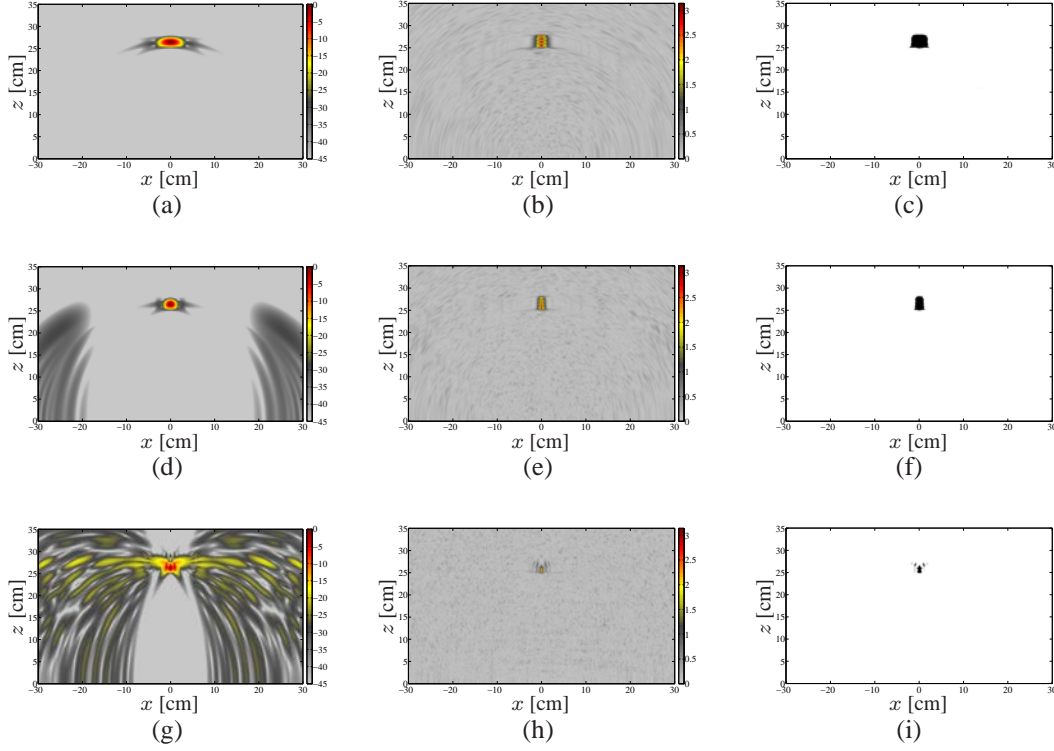
In practice, even if the SNR of each transmit-receive pair is low, the averaging effect of beamforming results in SNR improvement (HOLMES; DRINKWATER; WILCOX, 2005). The SNR for each signal can be improved before beamforming by averaging in acquisition, resulting in an SNR improvement in proportion to the square root of the number of averages.

Since the interaction between the wave and the reflectors, as well as their sizes and shapes, have not been considered, the estimator does not give information about the reflector characteristics. However, the thresholded IP image gives a statistical indication that the pixels with 1's values are related to the presence of reflectors in the inspected medium. This information can be used by the user who is analyzing the image to search for defects in image compounding techniques (HIGUTI et al., 2010) or as a weighting factor (CAMACHO; PARRILLA; FRITSCH, 2009; MARTÍNEZ-GRAULLERA et al., 2011).

PSF configurations *I*, *III* and *IV* were simulated for the same conditions of the used to obtain the results of Figure 24 (SNR = 10 dB). Different SNR values were also considered for configuration *I*. The proposed threshold ($\epsilon = 0.6444$) was applied to the IP images and the results are illustrated in Figures 32 and 33. By comparing configurations *I*, *III* and *IV*, the higher is the pitch value, smaller is the size of the reflector in the image and higher is the resolution. In contrast, more image artifacts are presented in amplitude images. From the IP images it is possible to observe that the grating lobes artifacts are significantly reduced and after

the threshold only the reflector region is considered.

Figure 32 – Amplitude (first column, in dB scale), IP (second column, in linear scale in radians) and thresholded IP images (third column, zero or one) considering SNR = 10 dB for configurations described in Table 1: (a), (b), (c) *I* ($\lambda/2$ -pitch), (d), (e), (f) *III* (λ -pitch) and (g), (h), (i) *IV* (4λ -pitch).



Source: Elaborated by the author.

By considering different SNR values, as expected from Figure 31, the size of the reflector in the image decreases with SNR, but it is identified without artifacts in the thresholded IP images. If a percentage of the maximum of amplitude image was considered as threshold value for reflector indication, artifacts due to grating lobes in Figure 32g and due to small SNR in Figure 33g could be considered as reflectors, depending on the chosen value.

5.1.4 Instantaneous phase weighting factor

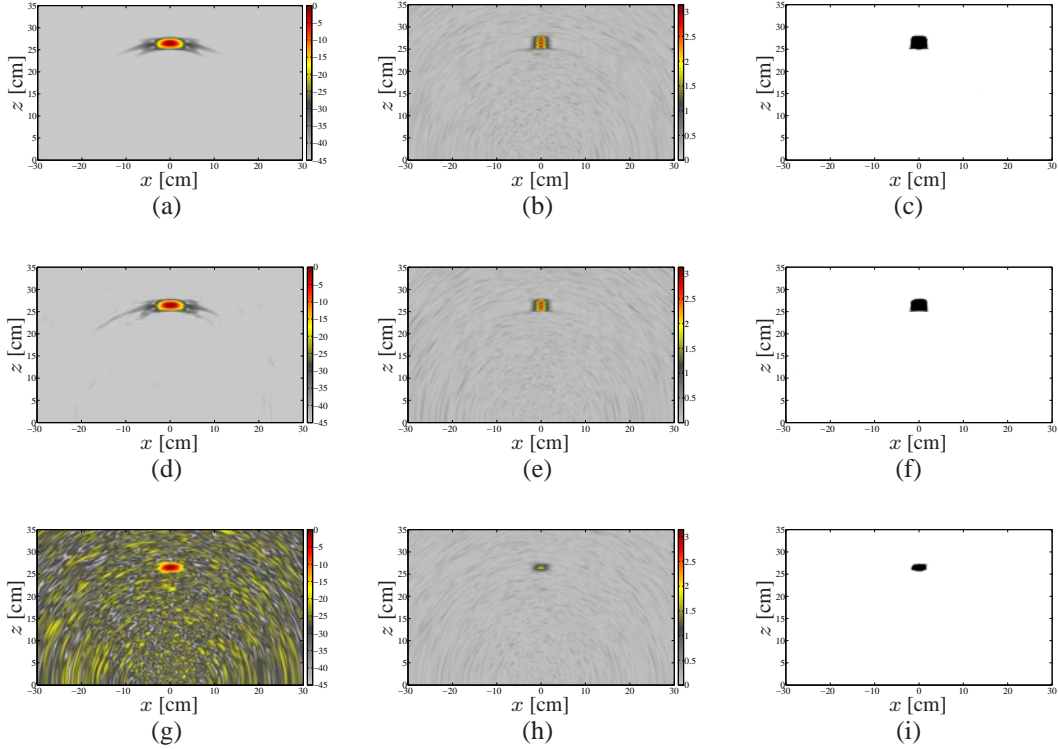
Among the alternatives proposed in literature, the Sign Coherence Factor (SCF) descriptor has shown best results. The SCF factor can be computed as (CAMACHO; PARRILLA; FRITSCH, 2009)

$$I_{\text{SCF}}(x, z) = 1 - \sigma, \quad (92)$$

where

$$\sigma^2 = 1 - \left[\frac{1}{M^2} \sum_{e=1}^M \sum_{r=1}^M b_{er}(\tau_{er}(x, z)) \right]^2, \quad (93)$$

Figure 33 – Amplitude (first column, in dB scale), IP (second column, in linear scale in radians) and thresholded IP (third column, zero or one) PSFs images for configuration *I* considering SNR equal to (a), (b), (c) 10 dB, (d), (e), (f) 0 dB and (g), (h), (i) -25 dB.



Source: Elaborated by the author.

and $b_{er}(t)$ is the polarity signal of the aperture data:

$$b_{er}(t) = \begin{cases} -1, & \text{if } v_{er}(t) < 0 \\ 1, & \text{if } v_{er}(t) \geq 0 \end{cases}. \quad (94)$$

σ is the standard deviation of the polarity $b_{er}(t)$ of the aperture data. The SCF measures the coincidence in algebraic sign of the received signals. Signals are defined as fully coherent if all of them have the same polarity ($I_{SCF}(x, z) = 1$). In other cases the value of $I_{SCF}(x, z)$ is in the range $[0, 1]$.

Other coherence factor is the CFM (Coherence Factor Map), which contains a measurement of signal phase distribution combined at each pixel. The CFM factor is given by (MARTÍNEZ-GRAULLERA et al., 2011):

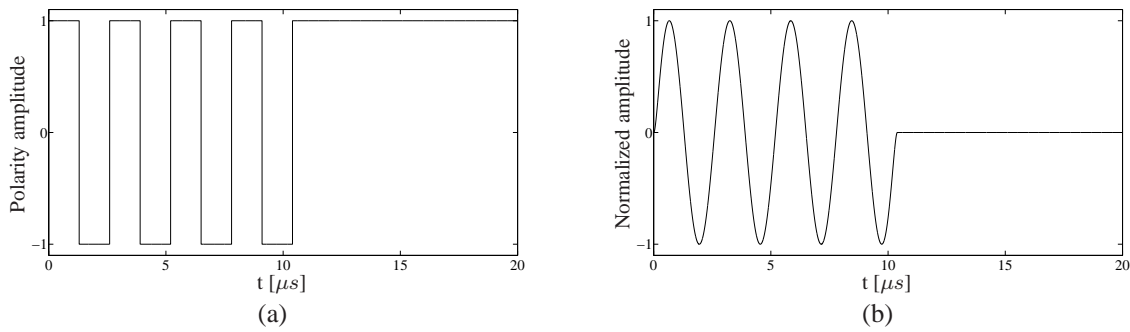
$$I_{CFM}(x, z) = \frac{1}{M^2} \left[\sum_{e=1}^M \sum_{r=1}^M \frac{v_{er}(\tau_{er}(x, z))}{V_{er}(\tau_{er}(x, z))} \right]^2, \quad (95)$$

where $V_{er}(t)$ is:

$$V_{er}(t) = \sqrt{v_{er}^2(t) + \hat{v}_{er}^2(t)}. \quad (96)$$

In practice this method normalizes the signal, sample by sample, which is used to replace $v(t)$ in (57). The main difference between the methods is the signal that is summed in beamforming. If the signal of Figure 22 is used as drive function, the IP image is related to the sum of the instantaneous phase of the signals, as illustrated in Figure 27. Likewise, the SCF is related to the sum of the polarity signals, as illustrated in Figure 34a, and the CFM to the sample normalized signal, as illustrated in Figure 34b. Direct (IP image) or indirectly (SCF and CFM), all methods are not using the amplitude information, but replacing it by the phase.

Figure 34 – (a) Polarity and (b) normalized (sample by sample) signals of a simulated 360 kHz 4-cycles amplitude signal with a Gaussian envelope without noise.



Source: Elaborated by the author.

At a defect position, all delayed signals should sum in phase, resulting in a high value (positive or negative) in the phase image. Where there is not a defect, the phases would sum randomly and lower values are expected. But the expected values and the distinction between reflector and noise have not been done by the authors (CAMACHO; PARRILLA; FRITSCH, 2009; MARTÍNEZ-GRAULLERA et al., 2011). The SCF factor is expected to be better than the CFM ones respect to artifacts reduction, since the first is powered by two in (93), attenuating the artifacts twice (in dB), and the last does not have any post-processing after beamforming.

Using the reflector indication, by considering the threshold ϵ , proposed in subsection 5.1.3, a weighting factor is created assuming 1 to the pixels where there is a reflector and P_E in other case. In the absence of a reflector it could be assumed 0, creating a high contrast image. However if a reflector is not well detected, due to its reflection coefficient, it would not be represented. By using a value in the range $]0, 1[$, where there is not a reflector, the intensity is reduced, improving the reflectors contrast, but not discarding the presence of a weak reflector.

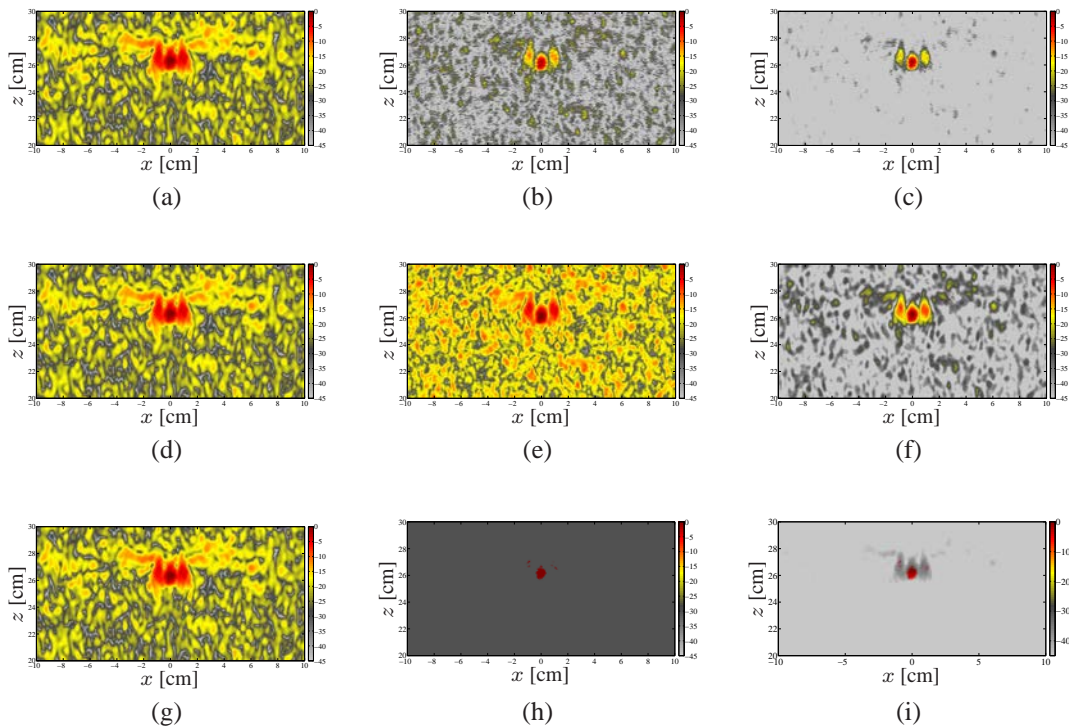
Therefore the instantaneous phase weighting factor is defined in this thesis as:

$$\text{IPWF}(x, z) = \begin{cases} 1, & \text{if } |I_\varphi(x, z)| \geq \epsilon \\ P_E, & \text{if } |I_\varphi(x, z)| < \epsilon \end{cases}, \quad (97)$$

and the final image is obtained by the multiplication of the amplitude image by the proposed weighting factor (IPWF), pixel by pixel.

PSF configuration *IV* was simulated with excitation signal of Figure 22, considering SNR equal to -20 dB, presenting significant grating lobes and low SNR. In this case, $P_E = 0.031$ (-30.2 dB). The grating lobes and noise artifacts are presented in the whole image, as can be observed in the amplitude image, which is illustrated in Figure 35a. The artifacts are more attenuated in SCF image than in CFM one, as expected. But both still present artifacts in the whole images. The IPWF has a two-level nature (1 or P_E), attenuating 30.2 dB the artifacts. Then the final image using the IPWF, illustrated in Figure 35i, has less artifacts in all image, mainly close to defect, improving contrast and resolution, respect to SCF and CFM, which are illustrated in Figures 35c and 35f, respectively.

Figure 35 – Amplitude image (first column), coherence factor (second column) and amplitude weighted image (third column) considering SNR equal to -20 dB for PSF configuration *IV*: (a), (b), (c) SCF, (d), (e), (f) CFM and (g), (h), (i) IPWF. Scales in dB.



Source: Elaborated by the author.

5.2 LAMB MODE DIVERSITY COMPOUNDING TECHNIQUE

In the case of plate-like structures, Lamb waves can propagate and different propagation modes can be coupled to the structure. Each mode is more or less sensitive to specific types of defects and has its own dispersion characteristic. Due to the different interactions of each propagation mode to defects, the images of a plate obtained by using different propagation modes are different to each other respect to contrast, resolution, image artifacts and dead zone.

One mode can produce images with better resolution and other with less artifacts, for example. Then, an image compounding technique is proposed to consider the Lamb mode diversity.

The method proposed is based on the procedure presented by Higuti et al. (2010). In that work, the images obtained from two different arrays (spatial diversity), which generated the fundamental S0 mode with low dispersion in an aluminum plate, and different apodizations are combined to generate the final image. There was improvement in contrast and resolution when compared to the use of only one array, but the use of two arrays increases the system complexity in terms of transducers and electronics. Furthermore, the selection parameter was empirically chosen: a 70% threshold value was applied to the coherence images, for each setup (different arrays and apodizations), and the pixels above the threshold value were considered part of a defect. The compounded image was obtained from the maximum of input images. Otherwise the minimum was taken.

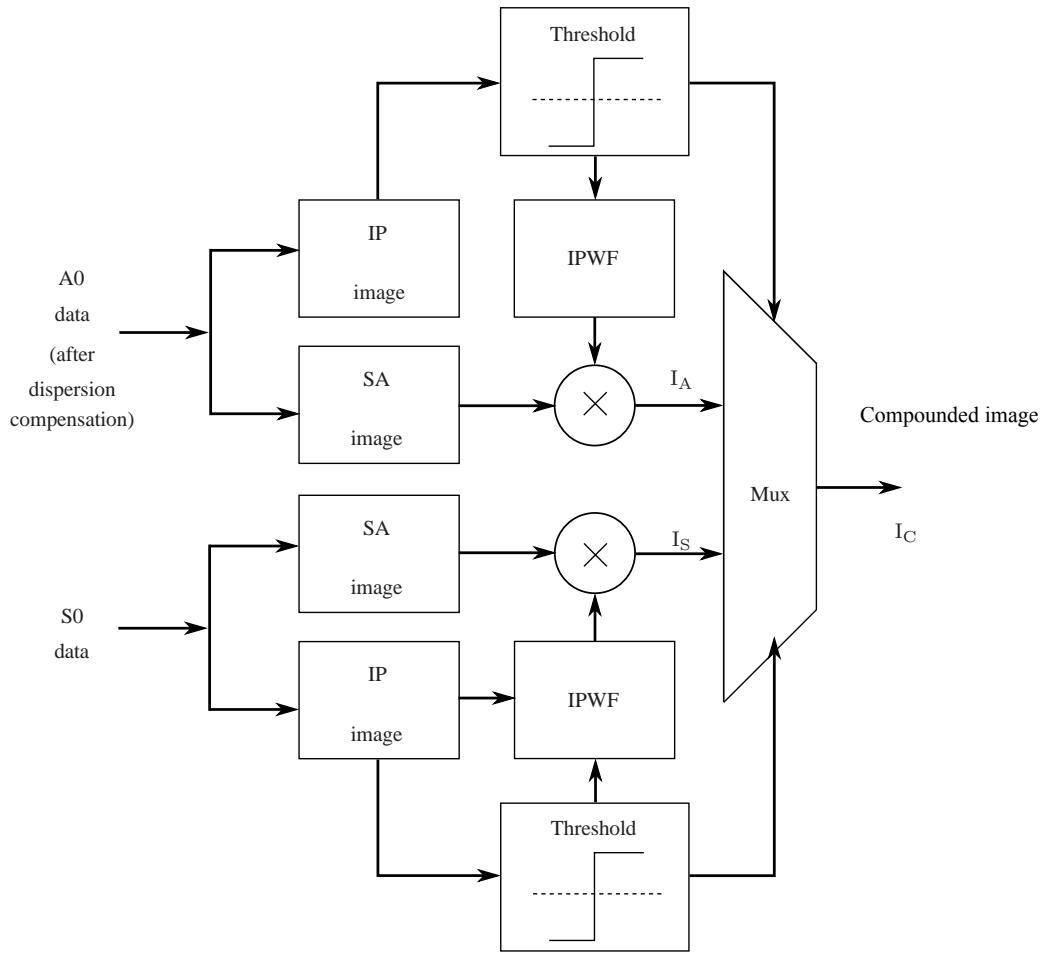
In the technique proposed in this thesis, the different interactions between each propagation mode and the defects are considered. The technique selects the information from the images obtained from two propagation modes generated by the same array. In addition to the use of just one array, compared with (HIGUTI et al., 2010), the selection parameter to be used is not empirical, but the threshold proposed in subsection 5.1.3. The block diagram of the method considering the A0 and S0 modes is shown in Figure 36.

For each mode (A0 and S0), two images are obtained: one SA image and one IP image, which is also used to obtain the IPWF. Each SA image presents different resolution and contrast due to specific interaction responses between each Lamb mode and the type of defect (ALLEYNE; CAWLEY, 1992a).

Before the multiplexer section (Mux), each SA image is multiplied by its respective IPWF, producing images I_A and I_S for the A0 and S0 modes, respectively. The A0 and S0 IP images are also used to indicate the presence of a defect, by considering the proposed threshold ϵ . The following rule is proposed, for each pixel:

- if both IP images are above their respective thresholds, it means that both modes detected the defect, and the compounded image I_C is obtained from: $I_C = \max \{I_A, I_S\}$. This procedure tends to preserve the best mode response;
- if both IP images are below their respective thresholds, it means that neither mode detected a defect, and the compounded image is obtained from: $I_C = \min \{I_A, I_S\}$. Then, contrast would be increased;
- if only the A0 IP image is above its threshold, it means that only this mode detected a defect, and the compounded image assumes the value: $I_C = I_A$;
- if only the S0 IP image is above its threshold, it means that only this mode detected a

Figure 36 – Block diagram of the proposed Lamb mode diversity compounding technique.



Source: Elaborated by the author.

defect, and the compounded image assumes the value: $I_C = I_S$.

This image compounding technique, which employs a kind of logical OR operator, tends to preserve the best response of each mode and reduce artifacts, improving contrast and resolution.

5.3 COMMENTS

The instantaneous phase image is used in conjunction with the proposed threshold level, producing a two-level image, which can be a valuable information for defect detection. The threshold level depends only on the number of signals used in beamforming. By increasing this value, the probability of occurrence of false indication of a defect decreases. The thresholded IP image is used as reflector indication, which is used in the image compounding technique to consider the Lamb diversity and to create a weighting factor for the amplitude images (IPWF). PSF configurations were simulated showing that the technique is very robust to grating lobes and noise, achieving better results when compared to other coherence factors, like SCF and

CFM. The proposed method using the instantaneous phase is less sensitive to amplitude losses in the echo signals than amplitude images, obtaining improvements in reflectors detectability for larger distances without previous knowledge of the media, such as attenuation characteristics, as shown in chapter 6. The Lamb mode diversity compounding technique combines the images obtained with different propagation modes and the compounded image should present better contrast, resolution and less image artifacts when compared to each individual single mode image. The proposed techniques were tested in an aluminum plate with artificial defects and the results are presented in the next chapter.

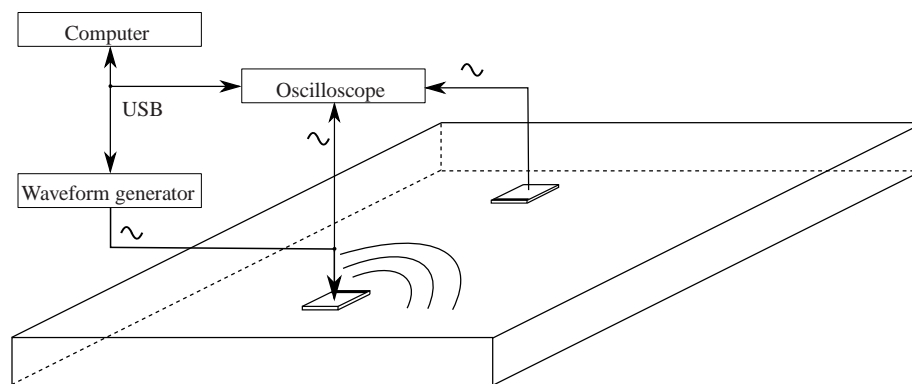
6 EXPERIMENTAL RESULTS

Some experiments were conducted with PZT ceramics to generate and acquire Lamb waves in an aluminum plate. Frequency response of the plate-piezoceramics system was obtained with two ceramics attached to the plate in transmit-receive mode. Artificial defects were produced in the plate and a 16-elements linear array was mounted. Conventional beamforming and the proposed methods were applied to observe the effect of dispersion, its compensation, and to evaluate the proposed techniques. The instantaneous phase images were compared to the amplitude ones to observe the sensitivity to amplitude losses. Different coherence factors were applied and compared to each other respect to contrast and image artifacts. Lamb mode diversity was also considered to improve image quality and defects detection. Empirical threshold values were used in the images and compared to the proposed one in chapter 5. This chapter presents the experimental setup, the obtained results and comments.

6.1 EXPERIMENTAL SETUP

All experiments were conducted using a 1 mm thickness isotropic aluminum plate ($1\text{ m} \times 1.24\text{ m}$). To obtain the frequency response of the plate-piezoceramics system, 2 piezoelectric ceramics were attached to the plate in transmit-receive mode, as illustrated in Figure 37. They were attached distant from each other 20 cm in the center of the plate, in order to avoid edges reflections, to simulate an infinite plate.

Figure 37 – Frequency response setup.

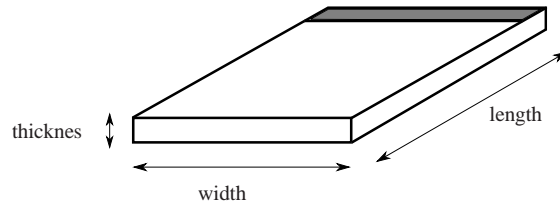


Source: Elaborated by the author.

The piezoceramics are PZT elements (Ferroperm PZ26) polarized in the thickness direction with dimensions $7\text{ mm} \times 7\text{ mm} \times 0.5\text{ mm}$, as illustrated in Figure 38. There is a $1\text{ mm} \times 7\text{ mm}$ area on the top surface that is electrically connected to the bottom surface to enable welding of

cables. Therefore, the active dimensions of the ceramic are 7 mm × 6 mm × 0.5 mm. Each ceramic was bonded to the plate with araldite adhesive.

Figure 38 – Ceramic: thicknes, width and length.

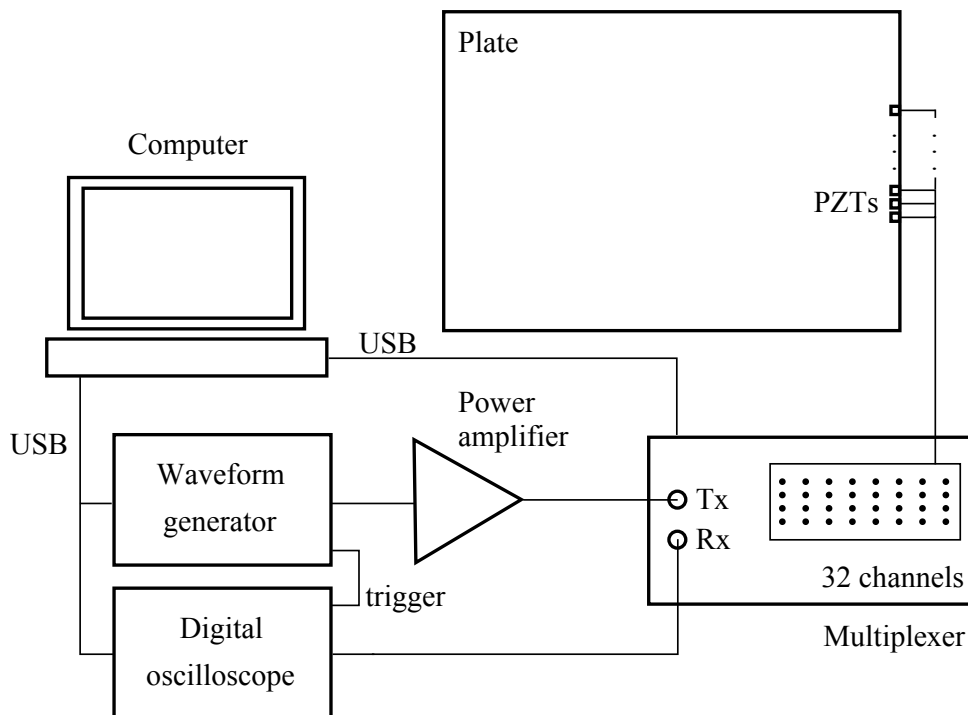


Source: Elaborated by the author.

The PZTs were excited by a waveform generator (Tektronix AFG3101, 14 bits resolution) and a power amplifier (ENI240L, 40W) with a 120 V peak-to-peak 4 cycles Gaussian envelope RF signal, as illustrated in Figure 22. Data acquisition was done using a digital oscilloscope (Agilent MSO7014B, 10 bits resolution in average mode), using average of 16 signals for each recorded waveform.

A linear array consisting of 16 piezoelectric elements with 9 mm pitch was mounted at the border of the aluminum plate. A 32 channels multiplexer was used to obtain all transmit-receive combinations employed in the beamforming techniques. The block diagram of the experimental setup can be observed in Figure 39 and some photos in Figure 40.

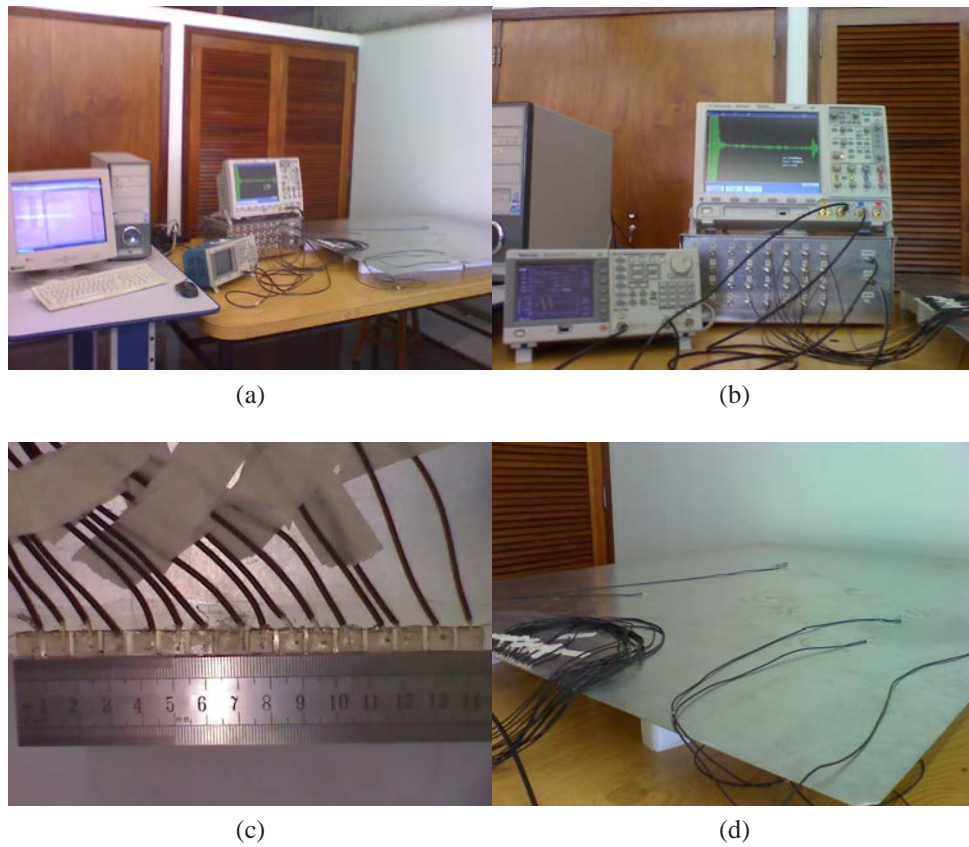
Figure 39 – Block diagram of the experimental setup.



Source: Elaborated by the author.

The plate with artificial defects can be seen in Figure 41. The central coordinates (x, z) of the defects with their geometries, dimensions (diameter for circular and area for square defects)

Figure 40 – (a) Experimental setup, (b) waveform generator, digital oscilloscope and multiplexer, (c) array and (d) aluminum plate.



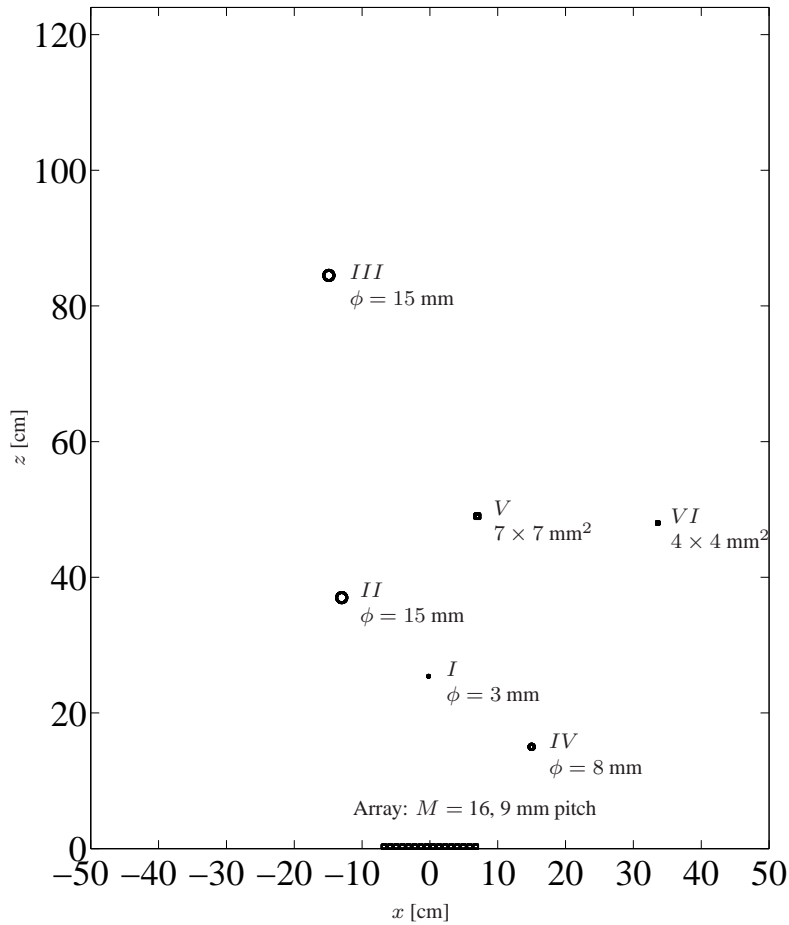
Source: Elaborated by the author.

and types are presented in Table 2. There is a through hole (defect *I*) and the surface defects are thin piezoceramics (0.5 mm thickness) bonded to the plate, except defect *IV*, which is a bolt whose head is bonded to the plate (head: 8 mm diameter x 5 mm height, screw: 4 mm diameter x 20 mm length). The surface defects simulate a perturbation on the plate surface, changing the acoustic impedance at that point and generating reflections, which could also occur if there was a metal loss or corrosion (KONSTANTINIDIS; DRINKWATER; WILCOX, 2006). This approach for simulating surface defects is a common laboratory procedure, because their positions can easily be changed, without making permanent damages to the structure.

Table 2 – Artificial defects produced in the aluminum plate.

Defect	x [cm]	z [cm]	Dimension	Geometry	Type
<i>I</i>	-0.2	25.4	3.0 mm	circular	hole
<i>II</i>	-13.0	37.0	15.0 mm	circular	surface
<i>III</i>	-14.9	84.5	15.0 mm	circular	surface
<i>IV</i>	15.0	14.5	8.0 mm	circular	surface
<i>V</i>	7.0	49.0	49.0 mm ²	square	surface
<i>VI</i>	33	48.0	16.0 mm ²	square	surface

Source: Elaborated by the author.

Figure 41 – Aluminum plate with defects. The center of the array is at $(x, z) = (0, 0)$.

Source: Elaborated by the author.

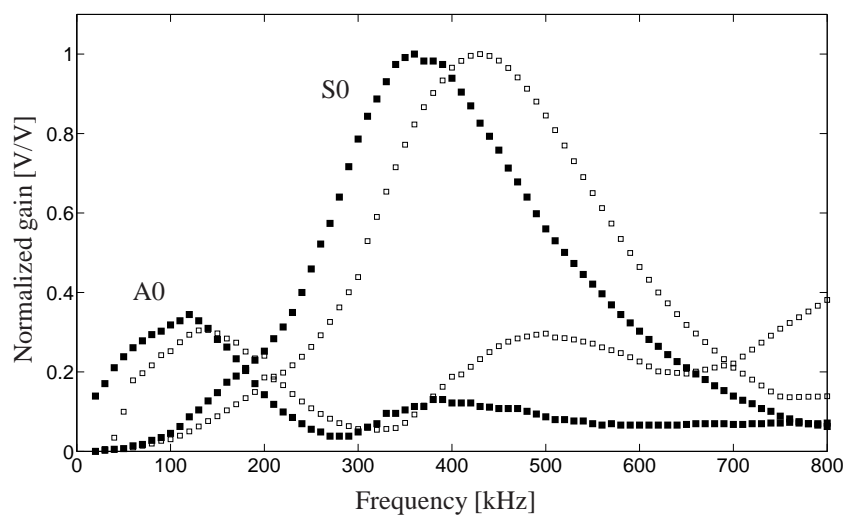
A region of the plate was defined for imaging: $-50 \leq x \leq 50$ and $0 \leq z \leq 100$ [cm] with 1 mm resolution in both directions. The plate end at $z = 124$ cm was not shown because there was no defect close to it. The plate ends generate strong specular reflections which would reduce contrast, but the images can also be obtained by regions, excluding or including the edges. The triangular apodization was considered in all images, using $w_{er} = 1$ in the beamforming (according to (57) and (59)). In all images the actual defects positions and sizes are represented along with their respective identifications (*I* to *VI*).

6.2 FREQUENCY RESPONSE

Each transducer can generate many propagation modes, which depends on its geometry and dimensions, the structure properties, the frequency of excitation and other parameters (SANTONI et al., 2007; YU; GIURGITIU, 2009). Experimental and simulated frequency responses of the

plate-piezoceramics system can be visualized in Figure 42. The simulation was done in *PZFlex*. Despite having the same behaviour, simulated and experimental responses have some differences, such as at resonance frequencies and A0 gain behaviour at higher frequencies. These differences are due to some non-idealities, such as ceramic-plate coupling/bonding and cable welding, for example, which are not considered in the simulations. Despite these differences, the dispersion characteristics as propagation velocity and signal shape are very similar.

Figure 42 – Frequency response using two piezoceramics in transmit-receive mode separated by 20 cm in a 1 mm thickness aluminum plate: *PZFlex* simulation (\square) and experimental results (\blacksquare).



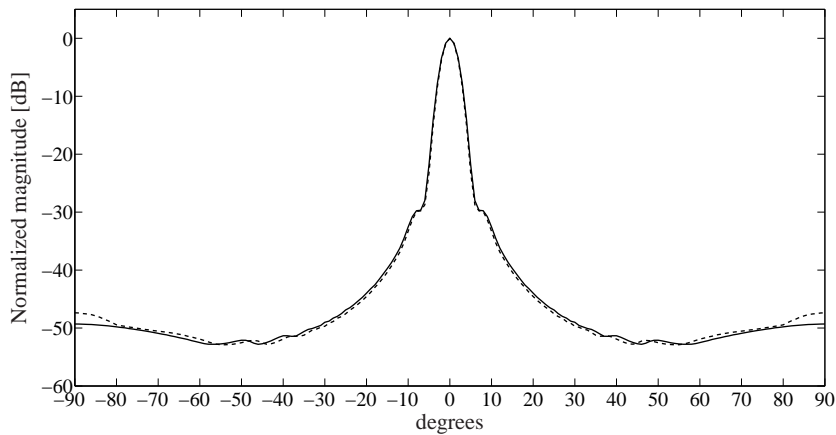
Source: Elaborated by the author.

Therefore, using these transducers, from 20 kHz to 800 kHz, only the fundamental symmetric and antisymmetric modes can be coupled. The S0 amplitude is much greater with respect to the A0 response at 360 kHz (430 kHz in simulation). At lower frequencies, around 100 kHz, the A0 mode response is higher. Consequently, the same array can be used to couple the A0 and S0 modes at the frequencies of 100 kHz and 360 kHz, respectively. The array is excited with tone bursts in order to obtain the best A0 and S0 responses for the transducer-structure employed. Other excitations could be used, such as chirp signals followed by post processing (MICHAELS et al., 2011, 2013), which could accelerate the process of data acquisition and signal processing in practical applications.

The wavelengths for the A0 and S0 modes are 16.5 mm and 15.9 mm, respectively. The half-wavelength is 7.95 mm in the worst case, which is less than the pitch used in the array (9 mm or 0.57λ). However, there are no serious consequences in terms of grating lobes, because they would be significant only for pitches close to λ or higher. Furthermore, the finite size of the individual elements and the wideband operation helps to reduce this effect. The simulated radiation pattern of the array operating at the A0 and S0 frequencies with a 4-cycles Gaussian burst obtained in MATLAB are shown in Figure 43. For the S0 mode there is a -47 dB grating

lobe level, which is relatively small and is related to the dynamic range used in the images.

Figure 43 – Radiation pattern of the array for the A0 (solid line) and S0 (dashed line) modes as a function of angle in degrees.



Source: Elaborated by the author.

6.3 DISPERSION COMPENSATION

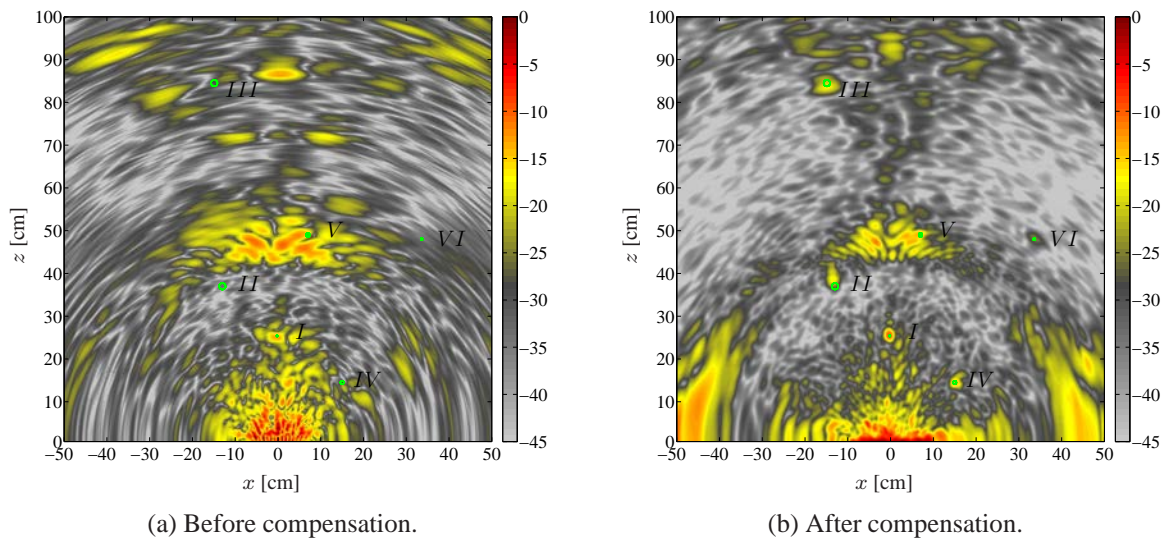
The S0 mode presents low dispersive characteristic with no significant improvements after dispersion compensation. Consequently, the dispersion compensation technique is applied only to the A0 mode. Figure 44 illustrates the results of A0 amplitude images before and after dispersion compensation obtained by using (59). Without dispersion compensation there are more artifacts and the defects do not appear at their correct locations. In the image obtained after dispersion compensation, on the other hand, defects *I*, *II*, *III*, *IV* and *VI* can be identified.

Beyond the representations of the defects, artifacts, strong reflections from the lateral plate ends and dead zone can also be observed, as illustrated in Figure 45. The dead zone is the region with high intensity artifacts close to the array, which is caused by the mechanical coupling between the elements. Figure 46 illustrates the echo signals received by one array element. The time of flight of the direct propagation and multiple reflections between the elements is short when compared to the echoes coming from defects. Therefore it reduces defect contrasts, for example for defect *I*, and can mask defects located close to the array, as defect *IV*.

6.4 AMPLITUDE AND INSTANTANEOUS PHASE IMAGES

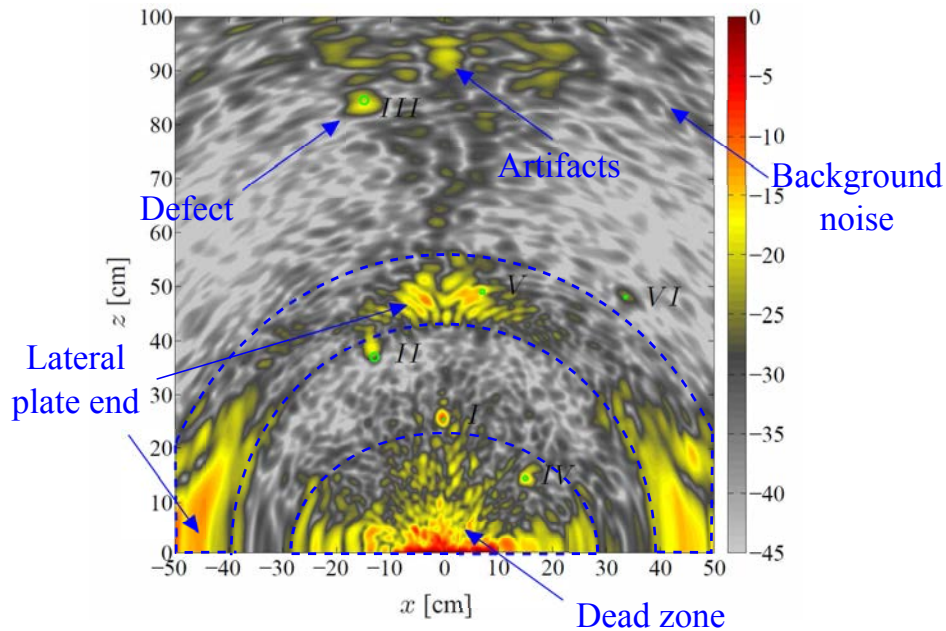
Figure 47 presents the A0 and S0 amplitude and IP images, obtained by using (59) and (62), respectively. The A0 IP image was also obtained from the dispersion compensated signals. Although both modes present similar wavelengths, defects are represented by different sizes

Figure 44 – A0 amplitude images: (a) before and (b) after dispersion compensation. Actual defects positions and sizes are indicated in green. Scales in dB.



Source: Elaborated by the author.

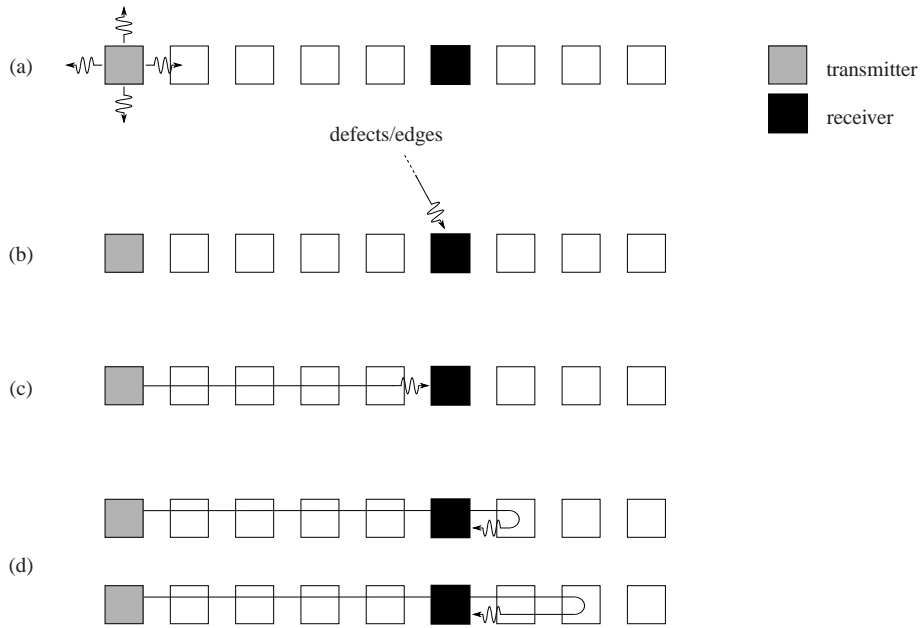
Figure 45 – A0 amplitude image after dispersion compensation with indications of dead zone, lateral plate ends reflections, defects, artifacts and background noise. Actual defects positions and sizes are indicated in green.



Source: Elaborated by the author.

and intensities in the A0 and S0 images. The defects represented in Figure 47a are smaller than the observed in Figure 47b, except for defect III, which means that A0 mode presents better resolution than S0 one for this case. On the other hand, defects I, II, V and VI are represented with higher intensities with S0 mode. In particular, defect IV, which is a bolt whose head is bonded to the plate, produces reverberations for the S0 mode. This behaviour is

Figure 46 – Echo signals received by one array element: (a) transmission, (b) echoes related to defects and edges, (c) direct propagation and (d) multiple reflections between the elements.



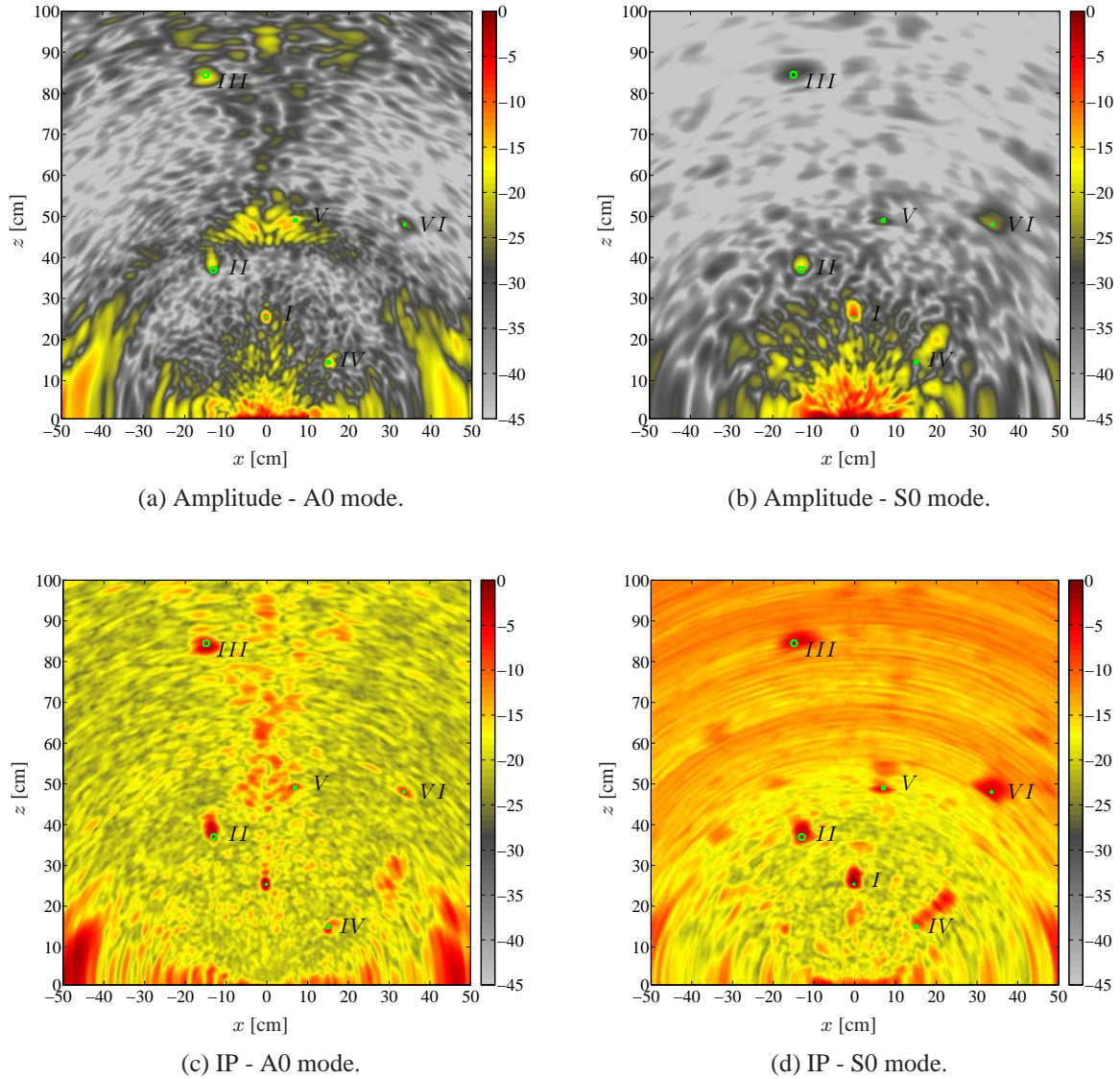
Source: Elaborated by the author.

not so significant for the other surface defects because they are thin piezoceramics.

In addition to defects sizes, each mode image results in different dead zones and artifacts due to the different interaction between each propagation mode and defects/edges of the plate. The dead zone is more pronounced in the S_0 amplitude image when compared to the A_0 image. The lateral plate end echoes, represented by the region between the semicircles with radius 40 cm and 50 cm, is more pronounced for the A_0 mode, which can mask some defects, for example defect V in Figure 47a. Due to these differences, the Lamb mode diversity compounding technique was proposed, which explores the characteristics of each mode (interaction with defects) to obtain an improved image.

The defects are more clearly identified in the IP images with higher intensities. On the other hand, the background noise is also higher than in the amplitude image, reducing the contrast and this is the reason why they are not used as final images, but can be used to give an indication of the presence of a defect. The axial view for $x = -13.9$ cm passing by defects II and III of the amplitude and IP images for S_0 mode are presented in Figure 48, for comparison. In this case, both images are normalized for defect II and are presented in dB. As commented, the defect contrast in the IP image is not better than the obtained in the amplitude one. For example, by considering the line passing by defect III in Figure 48, the difference between defect peak intensity (at $z \approx 85$ cm) and mean noise intensity close to it is lower in IP image than in amplitude one. On the other hand, the peak value is higher, which means that it is less influenced by signals amplitude losses than the amplitude image, allowing to detect defects that are more distant from the array. The amplitude losses in the echo signals can be originated

Figure 47 – Amplitude images for (a) A0 and (b) S0 modes; and IP images for (c) A0 and (d) S0 modes. Actual defects positions and sizes are indicated in green. Scales in dB for amplitude images and linear in radians for IP images.

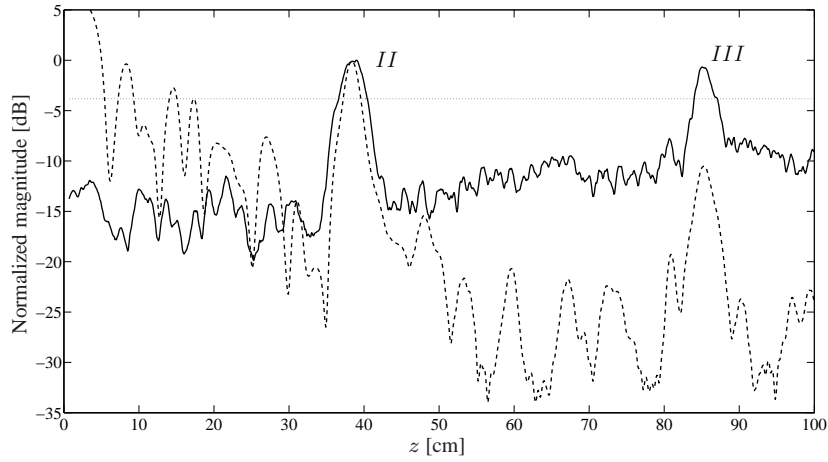


Source: Elaborated by the author.

mainly by two effects: diffraction of the acoustic beam and attenuation in the propagation path.

In Figure 48, if the threshold (dotted horizontal line) is applied to the IP image, both reflectors are detected. On the other hand, by observing the amplitude image result, there is not a suitable constant threshold level that could be used to detect all defects without producing a lot of image artifacts close to the array. Logarithmic or exponential functions could be used as threshold in order to detect all defects along the propagated distance, but attenuation information as well as other parameters should be known and could depend on the interpretation of the operator who is analyzing the images. The proposed threshold depends only on one parameter, the number of signals used for imaging, which in turn depends on the system (number of

Figure 48 – Axial view for $x = -13.9$ cm passing by defects *II* and *III* of the amplitude (dashed line) and instantaneous phase (solid line) images. Threshold ϵ value in dotted line.



Source: Elaborated by the author.

elements of the array) and the beamforming method (TFM).

6.5 COHERENCE FACTORS

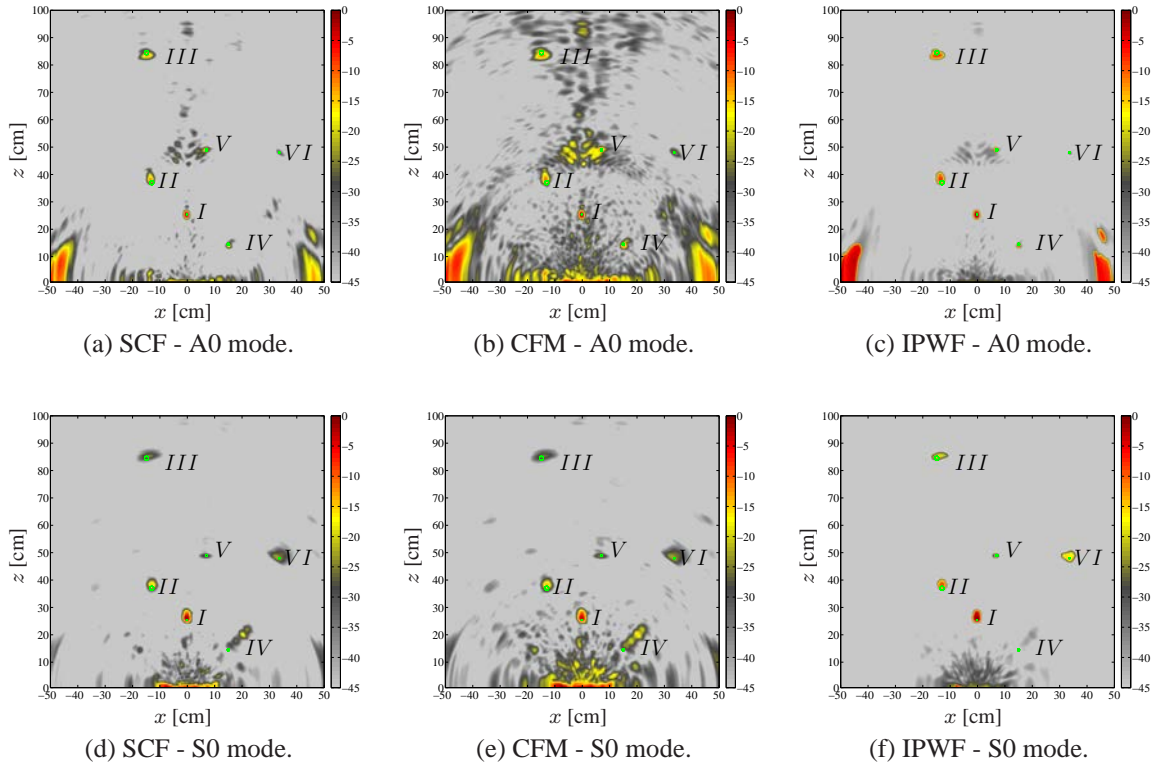
The amplitude images present some characteristics as: large dead zone, limited resolution and the presence of artifacts due to side lobes and small SNR. Figure 49 illustrates the result of the multiplication of the amplitude images by the coherence factors: SCF, CFM and IPWF, described in subsection 5.1.3, and Table 3 presents the defects contrasts¹ for each case, considering a square centered at the center of the defects, using the proposed threshold for both modes.

As expected, the multiplication procedure improves contrast significantly. For the A0 mode, defect *I* contrast, for example, was improved by 23.3 dB, 11.1 dB and 25.7 dB with SCF, CFM and IPWF, respectively. For the S0 mode, defect *I* contrast was improved by 22.7 dB, 15.3 dB and 23.0 dB with SCF, CFM and IPWF, respectively.

In addition to the contrast improvement, the coherence factors also reduce image artifacts, side lobes effects and dead zone. As already observed in the simulation of Figure 35 and now in Figures 49a, 49b, 49d and 49e, the artifacts are more attenuated in the SCF image than in the CFM one, but both still present artifacts in all images, mainly due to the lateral plate end reflections for the A0 mode and at dead zone for the S0 mode. The obtained images using the IPWF, illustrated in Figures 49c and 49f present less artifacts in the whole image, improving

¹The contrasts were calculated by the difference (in dB) between the average of the image values in the region where the IP image is above threshold (ϵ) and the average in the region where the IP image is below threshold: $\text{Contrast} = \text{mean}\{I(\text{where } I_\varphi \geq \epsilon)\} - \text{mean}\{I(\text{where } I_\varphi < \epsilon)\}$, where I is the image of interest (I_{amp} , $I_{\text{amp}} \times I_{\text{SCF}}$, $I_{\text{amp}} \times I_{\text{CFM}}$, $I_{\text{amp}} \times I_{\text{IPWF}}$).

Figure 49 – Amplitude images multiplied by the coherence factors: (a) SCF, (b) CFM and (c) IPWF for A0 mode; and (d) SCF, (e) CFM and (f) IPWF for S0 mode. Actual defects positions and sizes are indicated in green. Scales in dB .



Source: Elaborated by the author.

Table 3 – Defects contrasts before and after the multiplication of the amplitude images by the coherence factors. Values in dB.

Image ↓, Defect →	<i>I</i>	<i>II</i>	<i>III</i>	<i>IV</i>	<i>V</i>	<i>VI</i>
$I_{\text{amp-A0}}$	12.5	7.9	13.9	11.7	5.2	11.0
$I_{\text{amp-A0}} \times I_{\text{SCF-A0}}$	35.8	23.9	34.1	25.3	15.3	24.3
$I_{\text{amp-A0}} \times I_{\text{CFM-A0}}$	23.6	15.5	23.8	18.3	10.2	17.0
$I_{\text{amp-A0}} \times \text{IPWF}_{\text{A0}}$	38.2	21.0	36.5	23.9	19.1	12.5
$I_{\text{amp-S0}}$	15.5	13.5	9.9	0.8	7.5	8.2
$I_{\text{amp-S0}} \times I_{\text{SCF-S0}}$	38.2	29.2	17.7	1.4	17.0	18.4
$I_{\text{amp-S0}} \times I_{\text{CFM-S0}}$	30.8	23.9	18.5	1.1	14.5	18.0
$I_{\text{amp-S0}} \times \text{IPWF}_{\text{S0}}$	38.5	39.2	28.4	0.8	20.2	23.8

Source: Elaborated by the author.

contrast respect to the images obtained with the SCF and CFM factors, which can be observed quantitatively in Table 3. The high intensity pixels close to defect *IV* representation in the SCF and CFM images for the S0 mode are related to the reverberations and not to the defect, which is also not well represented.

6.6 LAMB MODE DIVERSITY

The A0 mode is more sensitive to surface defects than the S0 mode, which can be noted by the contrasts for defects *III*, *IV* and *VI* in table 3. For defects *II* and *V* the artifacts due to the lateral plate end mask the results.

Defects *I* to *VI* before and after the multiplication of the amplitude images by the IPWF are shown in detail in Figures 50. Although the contrast was significantly improved and image artifacts were reduced, defect *IV* is not represented in the S0 image after the multiplication procedure, and defect *VI* have weak indication in the A0 image, as can be observed in Figures 50p and 50v, respectively, with intensities similar to the dead zone. Artifacts close to the lateral plate end and close to some defects, as defects *II* and *V* for A0 mode, and close to the array elements position are also presented, but at different positions when comparing both images. These different characteristics are explored in the image compounding technique.

The resulting compounded image, using the proposed threshold for both modes is shown in Figure 51, while defects *I* to *VI* before and after the image compounding procedure are shown in detail in Figures 52. For defects *II* and *V*, there are strong lateral plate end reflections, resulting in artifacts close to the defect in the A0 mode image. In the same image, defect *VI* is represented with low intensity. In these case, the compounded image preserves most information from the S0 image, reducing artifacts and improving contrast. Defect *IV* was not detected by the S0 mode and the compounded image preserves most information from the A0 image. Dead zone and image artifacts intensity were reduced, improving reflectors intensities and, consequently, improving contrast when compared to each single mode image. Lateral plate end reflections and some elements can still be seen because they generate specular coherent reflections.

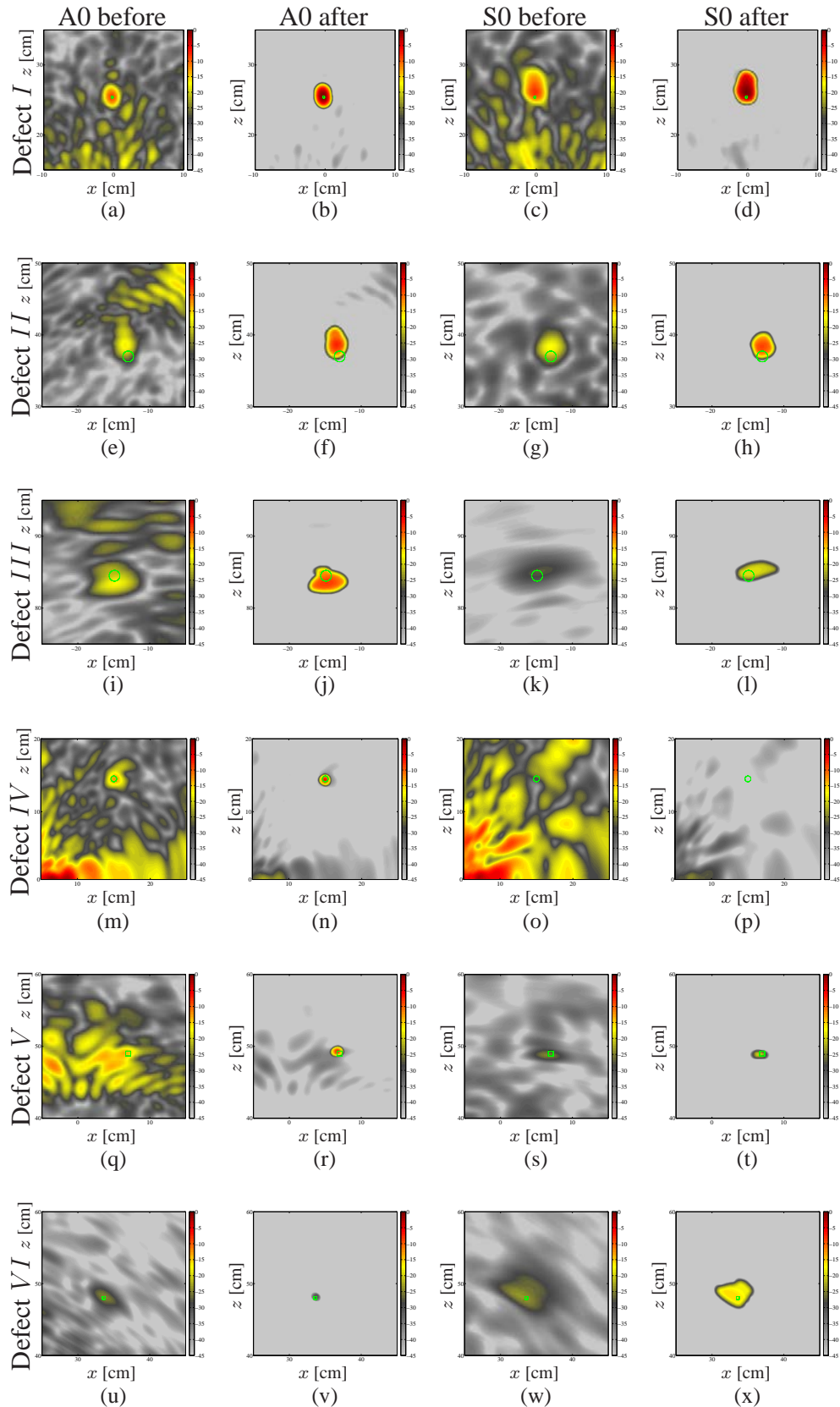
Table 4 presents the defects contrasts before and after the image compounding technique. Comparing Tables 3 and 4, it is possible to observe that the contrast improvement is a result of the image compounding technique and the multiplication of the amplitude by the IPWF images, with more contribution from the second. The most important contributions from the Lamb mode diversity is the significant artifacts reduction and the detection of all defects, which was not achieved with only a single mode operation (as weak detection of defect *VI* for A0 mode and non-detection of defect *IV* for S0 mode).

Table 4 – Defects contrasts before and after the image compounding technique. Values in dB.

Image ↓, Defect →	<i>I</i>	<i>II</i>	<i>III</i>	<i>IV</i>	<i>V</i>	<i>VI</i>
$I_{\text{amp-A0}} \times \text{IPWF}_{\text{A0}}$	38.2	21.0	36.5	23.9	19.1	12.5
$I_{\text{amp-S0}} \times \text{IPWF}_{\text{A0}}$	38.5	39.2	28.4	0.8	20.2	23.8
$I_{\text{compounded}}$	38.9	46.8	39.4	29.1	25.7	27.5

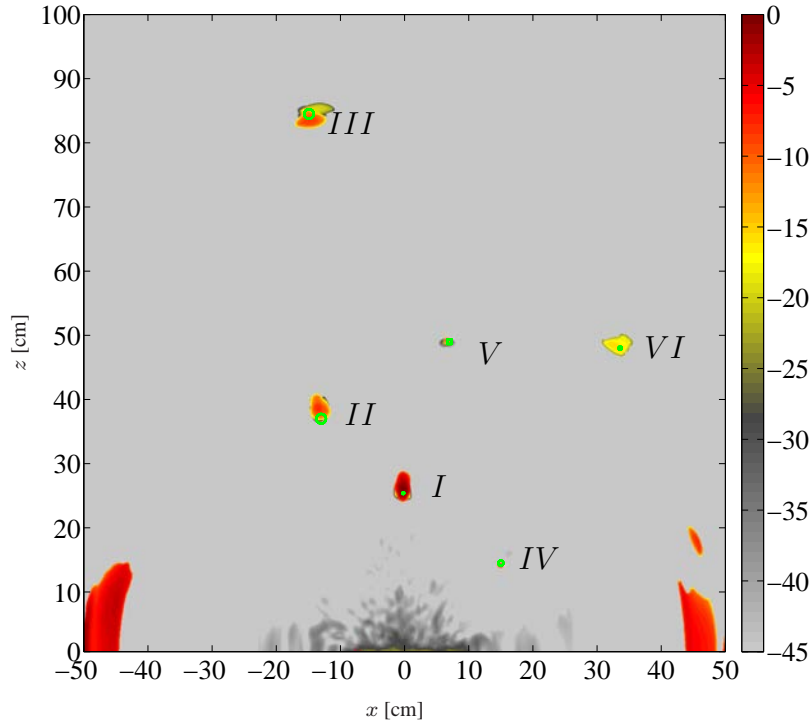
Source: Elaborated by the author.

Figure 50 – A0 mode before (first column) and after (second column) and S0 mode before (third column) and after (fourth column) the multiplication of the amplitude images by the IPWF for: (a), (b), (c), (d) defect *I*, (e), (f), (g), (h) defect *II*, (i), (j), (k), (l) defect *III*, (m), (n), (o), (p) defect *IV*, (q), (r), (s), (t) defect *V* and (u), (v), (w), (x) defect *VI*. Actual defects positions and sizes are indicated in green. Scales in dB .



Source: Elaborated by the author.

Figure 51 – Compounded image. Actual defects positions and sizes are indicated in green. Scale in dB.



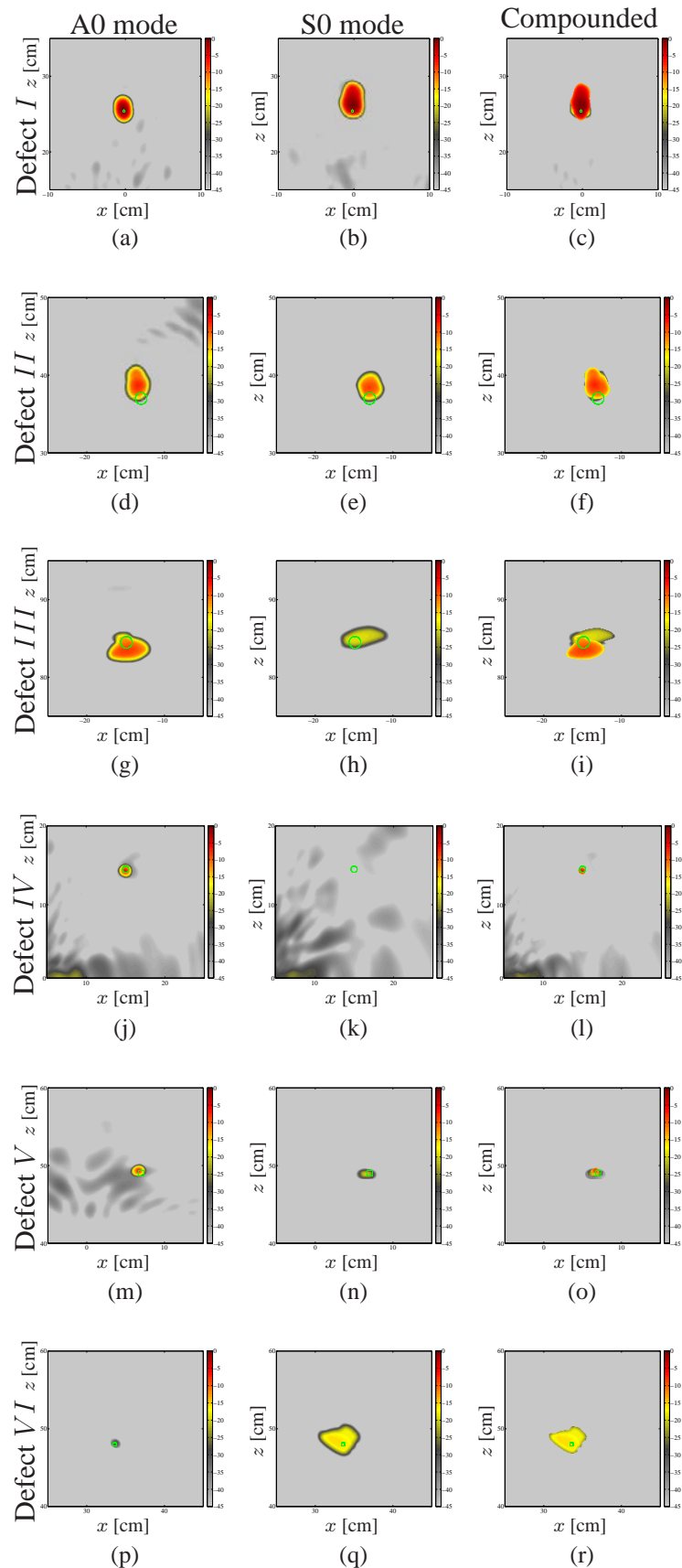
Source: Elaborated by the author.

6.7 THRESHOLD

The thresholded images, that indicate when the IP images are above and below threshold, are shown in Figures 53a and 53d: if the IP image is above threshold, the image assumes the value 1, otherwise, it is 0. The amplitude image can also be thresholded for producing a defect indicator. Using a 50% threshold, no defect is detected and due to the high intensity of dead zone, only some artifacts close to the array are above the threshold, as presented in Figures 53b and 53e, which would result in wrong interpretation respect to defects indication. By applying a threshold equal 50% of the maximum of the IP image, the two-level phase images are illustrated in Figures 53c and 53f. Dead zone and image artifacts are significantly reduced, and the results are very similar to the obtained with the proposed threshold. For the S0 mode, defect *IV* was not detected in none image (just some artifacts due to reverberation in Figure 53f), which is a result of the interaction between this mode and this defect.

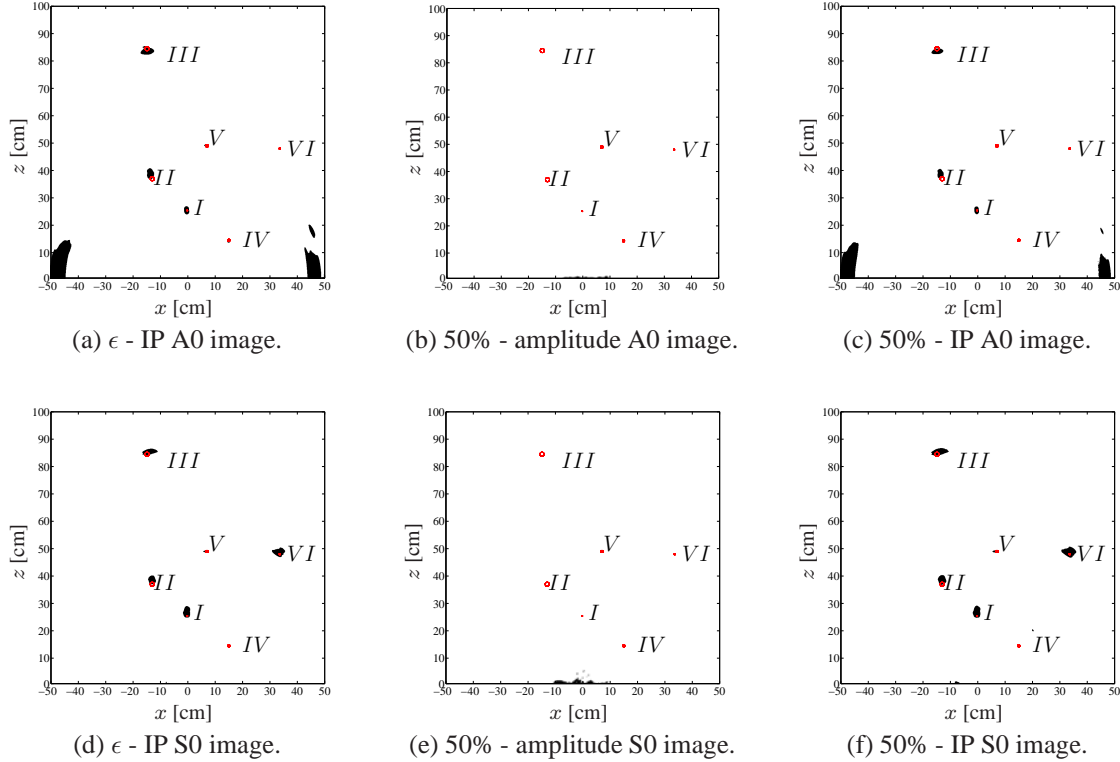
Other threshold values were also considered. For example, by applying a 10% threshold to the amplitude images, defects *I* and *II* are detected, dead zone is increased and some artifacts are considered as defects (false indications). As a consequence, the thresholded amplitude images do not result in a reliable defect indication, especially for a small number of signals, as in the case of this example. Different values were also applied to the IP images. As expected,

Figure 52 – A0 mode (first column,) S0 mode (second column) and compounded image (third column) for: (a), (b), (c) defect *I*, (d), (e), (f) defect *II*, (g), (h), (i) defect *III*, (j), (k), (l) defect *IV*, (m), (n), (o) defect *V* and (p), (q), (r) defect *VI*. Actual defects positions and sizes are indicated in green. Scales in dB .



Source: Elaborated by the author.

Figure 53 – Thresholded images for A0 mode: (a) IP image - ϵ , (b) amplitude image - 50% and (c) IP image - 50%; and for S0 mode: (d) IP image - ϵ , (e) amplitude image - 50% and (f) IP image - 50%. Actual defects positions and sizes are indicated in red.



Source: Elaborated by the author.

by increasing the threshold value, some defects detectability is reduced (non-detection of some defects). By reducing the threshold value, many artifacts are considered as defects.

6.8 COMMENTS

All experimental results of this work were presented in this chapter. An isotropic plate (aluminum) was used and a 16-elements linear array was mounted over it. The conventional beamforming technique introduced in chapter 4 and the proposed methods presented in chapter 5 were applied to the experimental setup. For the A0 mode at the frequency-thickness product of operation, the dispersion compensation method shown in chapter 2 should be used for correct defect detection. Each mode produces different defects, dead zones and image artifacts representations. In addition to the Lamb mode diversity, the multiplication of amplitude images by the proposed coherence factor reduces dead zone and improves contrasts significantly, being a good practice to improve the quality of images. By evaluating the phase information from the IP images, the compounding technique selects, pixel by pixel, the best contribution coming from each mode image and, as a result, dead zone and image artifacts are reduced and contrast are improved, enhancing damage detection. The proposed method using the instantaneous

phase is less sensitive to amplitude losses in the echo signals than amplitude images, obtaining improvements in reflectors detectability for larger distances without previous knowledge of the media, such as attenuation characteristics. Since the threshold level is a parameter that controls the sensitivity of the image compounding method, the smaller is the number of parameters, especially those which can depend on the operator interpretations, more robust is the technique. The proposed threshold depends only on the number of signals used in beamforming.

7 FINAL REMARKS AND FUTURE WORK

7.1 DISCUSSIONS

This thesis was the first one developed on ultrasonic NDT of plate-like structures using piezoelectric array transducers and ultrasonic images at the Ultrasound Laboratory (UNESP - Ilha Solteira). So, basic studies were conducted in three areas, as described in chapters 2, 3 and 4: (i) Lamb waves - propagation modes, dispersion curves (numerical solutions), cutoff frequencies and dispersion compensation; (ii) arrays - parameters as number of elements, pitch, apodization, excitation delay, finite dimensions of the elements of the array and pulsed excitation, that change the radiation pattern respect to beam focusing and steering, main lobe width, side lobes levels and presence of grating lobes, which are directly related to image resolution, contrast and artifacts; (iii) ultrasonic imaging - synthetic aperture (SA) technique to obtain the image from the signals of all combinations of emitter-receiver of the array, point spread function (PSF) to simulate and evaluate the array and the image algorithm, and relation between array radiation pattern and image quality.

The use of SA techniques using the total focusing method (TFM) has the advantage that it generates the maximum lateral resolution available at each imaging point, producing high-quality images. However, because the individual signals can present low signal-to-noise ratio (SNR), there is a limitation in detecting reflectors or objects that are far from the array. Furthermore, there are several artifacts in the images of plates due to low SNR and different propagation modes, that can exist simultaneously. Each mode presents a particular propagation velocity, dispersion characteristic and interaction with defects, that should be considered. Other limitation is the significant dead zone, that can hide some defects and reduce the effective dynamic range, as result of the multiple reflections between the elements of the array, for the case of guided waves coupled by PZT ceramics.

From the same data set used in TFM, coherence images and image compounding techniques were studied and implemented to improve these characteristics. Two contributions of this work are: (i) a method for defect detection based on the instantaneous phase of the aperture data, exploring the coherence information; and (ii) an image compounding technique to combine the images obtained from different propagation modes, which are sensitive to different types of defects.

The coherence of the signals is already explored by conventional SA techniques. At a defect position, all delayed signals should sum in phase, resulting in a high value (positive or

negative). Where there is not a defect, the amplitudes would sum randomly and lower values are expected. On the other hand, if there is not a defect, for a given transmit-receive pair, an echo due to reflections from defects, or the border of the plate coming from other directions, can arrive at the same time, increasing the magnitude of the sum. A high noise level can also lead to similar results. Then, techniques to improve the quality of the images based on this property are generally called coherence methods. Coherence images have been used only as weighting factors, multiplied by the amplitude images to reduce side and grating lobes influence, artifacts, and improve contrast (CAMACHO; PARRILLA; FRITSCH, 2009; MARTÍNEZ-GRAULLERA et al., 2011). But they contain more information that can be used to further improve defects detection and image quality, as explored in this work.

For image compounding techniques, there are different procedures to combine images that carry different information, such as adding all images (DAVIES; CAWLEY, 2007), taking the maximum or the minimum of them (MICHAELS; MICHAELS, 2007), pixel by pixel, applying logical AND or OR operators and intermediate selection using binary images to indicate the presence or not of a defect and then select the maximum or minimum value (HIGUTI et al., 2010). For the last case, a threshold with certain percentage of the maximum of the amplitude or coherence image was used to indicate the presence of a defect. If the pixel intensity is above threshold, then it is considered part of a defect. A problem is the choice of the threshold value, which has been done empirically. The threshold value controls the sensitivity of the technique and then must be properly designed, since it influences directly in the quality of the results. Then, a threshold definition is proposed in this work and applied to an image compounding technique, which explores the Lamb mode diversity.

Although the focus of this work was the study and implementation of NDT techniques of plate-like structures using piezoelectric array transducers and guided acoustic waves, the proposed method for defect detection was also tested in a problem involving bulk wave, as can be seen in the paper published at IEEE Transactions on Ultrasonics, Ferroelectrics and Frequency Control, entitled “Instantaneous phase threshold for reflectors indication in ultrasonic images”. A medical phantom was examined using a commercial array transducer of 64 elements at 2.6 MHz. The proposed method using the phase resulted in improvements in reflector detectability for larger distances without previous knowledge of attenuation characteristics of the propagation medium. There was also significant reduction in false indication of reflectors.

The focus of the experimental tests was to validate the proposed methods. Thereby a simple case of an isotropic aluminum plate has been considered. There is an interest in inspecting realistic and more complex structures (isotropic and anisotropic), which can present variable thickness, stiffeners, bolts, etc.

7.2 CONCLUSIONS

In this work the instantaneous phase image is proposed as a coherence image, by replacing the amplitude data by its instantaneous phase in SA beamforming. This image is very similar to the ones obtained by the other coherence methods, such as the Sign Coherence Factor (SCF) (CAMACHO; PARRILLA; FRITSCH, 2009) and the Coherence Factor Map (CFM) (MARTÍNEZ-GRAULLERA et al., 2011). The main contribution of the proposed method is the definition of a threshold level that is applied to the IP image, based on a statistical analysis of noise and the number of signals used in beamforming. The thresholded IP image can then be used to directly indicate the presence of a reflector, to create a weighting factor for amplitude images, or as a selection parameter in image compounding techniques.

The instantaneous phase weighting factor is created with a discrete nature: 1 to the pixels where there is a reflector, according to the analysis of IP image, and a finite value determined by the probability of error (P_E) in other case (value in the range]0, 1[), different from the other coherence factors, which are directly used as weighting factor. PSF simulations and the experimental images of the aluminum plate with defects have shown that the technique is very robust to grating lobes and noise, achieving better results respect to contrast improvement and image artifacts reduction when compared with SCF and CFM.

Empirical threshold values were also applied to the amplitude and the IP images. By increasing the threshold value, some defects detectability is reduced (non-detection of some defects). By reducing the threshold value, many artifacts are considered as defects. On the other hand, the proposed threshold detected all defects for the A0 and S0 modes, with exception of defect *IV* (bolt bonded to the plate) for the S0 mode, which is not due to the method, but to the interaction of this mode and this type of defect. Then, to improve defects detectability as well as image quality, a Lamb mode diversity compounding technique was also proposed.

The compounding procedure proposed in this thesis is based on Higuti et al. (2010), which combined the images obtained from two different arrays (spatial diversity) with different apodizations. In this work, Lamb mode diversity is explored. The method selects the information from the images obtained with two propagation modes (A0 and S0) generated by the same array. In addition to the use of only one array, compared with (HIGUTI et al., 2010), the selection parameter to be used in the reference image is not empirical, but the threshold proposed in subsection 5.1.3. The A0 and S0 modes present different interaction with different types of defects, resulting in different representations in the obtained images respect to contrast, resolution and image artifacts. For the A0 mode at the frequency-thickness product of operation, the dispersion compensation method should be used for correct defect detection. By the use of the proposed threshold to indicate the presence or not of a defect, the selection depends on the system parameters (in this case only on the number of signals used in the beamforming), and not on interpretations of the operator who is analyzing the image or based on empirical parameters.

By evaluating the phase information from the IP images, the compounding technique selects, pixel by pixel, the best contribution coming from each mode image and, as a result, dead zone and image artifacts are reduced and contrasts are improved, enhancing damage detection. In addition to the Lamb mode diversity, the multiplication of the amplitude images by the proposed coherence factor reduces dead zone and improves contrasts significantly, being a good practice to improve the quality of images.

7.3 CONTRIBUTIONS

The contributions of this work are:

- A new coherence image obtained by the use of the instantaneous phase of the signals;
- A threshold definition based on a statistical analysis of the instantaneous phase image, which can be used to directly indicate the presence of a reflector, to create a weighting factor for amplitude images, or as a selection parameter in image compounding techniques;
- An image compounding technique to explore the Lamb mode diversity. The compounding procedure is not new. The contribution is the information that is combined and the reference image used as selection criteria.

7.4 PUBLICATIONS

As result of this work some papers were published in journals and conference proceedings.

Papers:

- PRADO, V. T.; HIGUTI, R. T.; KITANO, C.; MARTÍNEZ-GRAULLERA, O. Instantaneous phase threshold for reflectors indication in ultrasonic images. *IEEE Transactions on Ultrasonics, Ferroelectrics and Frequency Control*, New York, v. 61, n. 7, p. 1204-1215, 2014.
- PRADO, V. T.; HIGUTI, R. T.; KITANO, C.; MARTÍNEZ-GRAULLERA, O.; ADAMOWSKI, J. C. Lamb mode diversity imaging for non-destructive testing of plate-like structures. *NDT&E International*. London, v. 59, p. 86-95, 2013.
- PRADO, V. T.; HIGUTI, R. T.; KITANO, C.; MARTÍNEZ-GRAULLERA, O. Sparse arrays and image compounding techniques for non-destructive testing using guided acoustic waves. *Journal of Control, Automation and Electrical Systems*, Heidelberg, v. 24, p. 263-271, 2013.

Conferences:

- PRADO, V. T.; HIGUTI, R. T.; KITANO, C.; MARTÍNEZ-GRAULLERA, O.; GRANJA, S. C. G. The use of instantaneous phase for improving SAFT images. In: INTERNATIONAL CONGRESS ON ULTRASONICS - ICU, 8., 2013, Singapore. *Proceedings...* Singapore: Research Publishing, 2013. p. 458-463.
- PRADO, V. T.; HIGUTI, R. T.; KITANO, C.; MARTÍNEZ-GRAULLERA, O. The use of instantaneous phase for improving sparse arrays images. In: IEEE INTERNATIONAL ULTRASONICS SYMPOSIUM - IUS, 52., 2013, Prague. *Proceedings...* Prague: IEEE, 2013. p. 974-977.
- PRADO, V. T.; HIGUTI, R. T.; KITANO, C. Comparison between ultrasonic synthetic aperture imaging methods using the phase of signals for plate-like structures. In: INTERNATIONAL CONGRESS OF MECHANICAL ENGINEERING, 22., 2013, Ribeirão Preto. *Proceedings...* Rio de Janeiro: ABCM, 2013. p. 1-12.
- PRADO, V. T.; HIGUTI, R. T.; KITANO, C.; MARTÍNEZ-GRAULLERA, O.; ADAMOWSKI, J. C. Technique to combine images produced by different propagation modes of guided waves for damage detection and contrast improvement in plate-like structures. In: IEEE INTERNATIONAL ULTRASONICS SYMPOSIUM - IUS, 51., 2012, Dresden. *Proceedings...* Dresden: IEEE, 2012. p. 1441-1444.
- PRADO, V. T.; HIGUTI, R. T.; KITANO, C. Utilização do software PZFlex como ferramenta de auxílio para ensaios não-destrutivos por ultrassom de estruturas tipo placa. In: CONFERÊNCIA BRASILEIRA DE DINÂMICA, CONTROLE E APLICAÇÕES, 10., 2011, Águas de Lindóia. *Proceedings...* Rio de Janeiro: ABCM, 2011. p. 180-183.

7.5 FUTURE WORK

The following future research issues can be proposed:

1. Since the methods use the instantaneous phase of the signals, techniques to better estimate this parameter can be investigated or developed for low SNR conditions;
2. Phase/frequency modulation methods, as well as coded excitation, can be studied to improve the sensitivity of the proposed method to noise and make the defect detection criteria more robust;
3. The proposed method was evaluated only for isotropic materials. The application of the technique, as well as necessary adjustments, to anisotropic materials is a promising

topic to investigate since the quality of the images using anisotropic materials is limited (OSTACHOWICZ et al., 2009; SU et al., 2009; LI et al., 2013);

4. All studies in the laboratory were conducted considering plates with artificial defects. Then, it could be interesting to study and evaluate structures with complex geometries and real defects;
5. Defects representations obtained with the proposed method change with noise level, which is undesirable if one wishes to characterize the defect for a quantitative assessment of the structure condition. Therefore, methods for defects characterization can be studied by considering both information: amplitude and phase of the reflected signals.

REFERENCES

- ALLEYNE, D. N.; CAWLEY, P. The interaction of Lamb waves with defects. *IEEE Transactions on Ultrasonics, Ferroelectrics and Frequency Control*, New York, v. 39, n. 3, p. 381–397, 1992a.
- ALLEYNE, D. N.; CAWLEY, P. Optimization of Lamb wave inspection techniques. *NDT&E International*, London, v. 25, n. 1, p. 11–22, 1992b.
- ASL, B. M.; MAHLOOJIFAR, A. Minimum variance beamforming combined with adaptive coherence weighting applied to medical ultrasound imaging. *IEEE Transactions on Ultrasonics, Ferroelectrics and Frequency Control*, New York, v. 56, n. 9, p. 1923–1931, 2009.
- AUSTENG, A.; HOLM, S. Sparse 2D arrays for 3D phased array imaging design methods. *IEEE Transactions on Ultrasonics, Ferroelectrics and Frequency Control*, New York, v. 49, n. 8, p. 1073–1086, 2002.
- AUSTENG, A.; HOLM, S.; WEBER, P. K.; AAKVAAG, N.; IRANPOUR, K. 1D and 2D algorithmically optimized sparse arrays. In: *IEEE ULTRASONICS SYMPOSIUM*, 36., 1997, Toronto. *Proceedings...* Toronto: IEEE, 1997. v. 2, p. 1683–1686.
- BAVARO, V.; CALIANO, G.; PAPPALARDO, M. Element shape design of 2D CMUT arrays for reducing grating lobes. *IEEE Transactions on Ultrasonics, Ferroelectrics and Frequency Control*, New York, v. 55, n. 2, p. 308–318, 2008.
- BOLLER, C. Ways and options for aircraft structural health monitoring. *Smart Materials and Structures*, New York, v. 10, n. 3, p. 432–440, 2001.
- BROTHERHOOD, C. J.; DRINKWATER, B. W.; FREEMANTLE, R. J. An ultrasonic wheel-array sensor and its application to aerospace structures. *INSIGHT. Journal of the British Institute of NDT*, London, v. 45, n. 11, p. 729–34, 2003.
- BUREAU, J. M.; STEICHEN, W.; LEBAIL, G. A two-dimensional transducer array for real-time 3D medical ultrasound imaging. In: *IEEE ULTRASONICS SYMPOSIUM*, 37., 1998, Sendai. *Proceedings...* Sendai: IEEE, 1998. v. 2, p. 1545–1553.
- CAMACHO, J.; FRITSCH, C. Phase coherence imaging of grained materials. *IEEE Transactions on Ultrasonics, Ferroelectrics and Frequency Control*, New York, v. 58, n. 5, p. 1006–15, 2011.
- CAMACHO, J.; PARRILLA, M.; FRITSCH, C. Phase coherence imaging. *IEEE Transactions on Ultrasonics, Ferroelectrics and Frequency Control*, New York, v. 56, n. 5, p. 958–974, 2009.
- CARLSON, A. B.; CRILLY, P. B. *Communication systems*. [S.l.]: McGraw-Hill Higher Education, 2009. 924 p.

CAWLEY, P.; ALLEYNE, D. N. The use of Lamb waves for the long range inspection of large structures. *Ultrasonics*, Surrey, v. 34, n. 2, p. 287–290, 1996.

CHIMENTI, D. E. Guided wave in plates and their use in materials characterization. *Applied Mechanics Reviews*, New York, v. 50, n. 5, p. 247–284, 1997.

CLARKE, T.; CAWLEY, P.; WILCOX, P. D.; CROXFORD, A. J. Evaluation of the damage detection capability of a sparse-array guided-wave SHM system applied to a complex structure under varying thermal conditions. *IEEE Transactions on Ultrasonics, Ferroelectrics and Frequency Control*, New York, v. 56, n. 12, p. 2666–2678, 2009.

DAVIES, J.; CAWLEY, P. The application of synthetically focused imaging techniques for high resolution guided wave pipe inspection. In: REVIEW OF PROGRESS IN QUANTITATIVE NONDESTRUCTIVE EVALUATION, 34., 2007, Portland. *Proceedings...* Portland: AIP Publishing, 2007. v. 26, p. 681–688.

DIAMANTI, K.; SOUTIS, C.; HODGKINSON, J. M. Piezoelectric transducer arrangement for the inspection of large composite structures. *Composites Part A: Applied Science and Manufacturing*, Oxford, v. 38, n. 4, p. 1121–1130, 2007.

DRINKWATER, B. W.; WILCOX, P. D. Ultrasonic arrays for non-destructive evaluation: a review. *NDT&E International*, London, v. 39, n. 7, p. 525–541, 2006.

FARRAR, C. R.; WORDEN, K. An introduction to structural health monitoring. *Philosophical Transactions of the Royal Society A: Mathematical, Physical and Engineering Sciences*, London, v. 365, n. 1851, p. 303–315, 2007.

FENSTER, A.; DOWNEY, D. B. 3-D ultrasound imaging: a review. *IEEE Engineering in Medicine and Biology Magazine*, New York, v. 15, n. 6, p. 41–51, 1996.

FRIDMAN, P. A. Optimal array configuration search using genetic algorithms. In: APPLICATIONS OF DIGITAL IMAGE PROCESSING, 24., 2001, San Diego. *Proceedings...* San Diego: SPIE, 2001. v. 4472, p. 518–527.

GACHAGAN, A.; HAYWARD, G.; MCNAB, A.; REYNOLDS, P.; PIERCE, S.; PHILP, W.; CULSHAW, B. Generation and reception of ultrasonic guided waves in composite plates using conformable piezoelectric transmitters and optical-fiber detectors. *IEEE Transactions on Ultrasonics, Ferroelectrics and Frequency Control*, New York, v. 46, n. 1, p. 72–81, 1999.

GAO, G.; DENG, M.; LI, M.; PEI, J. Mode selection of lamb waves for the evaluation of solid plates with liquid loading. *Science China Physics, Mechanics & Astronomy*, Heidelberg, v. 57, n. 10, p. 8, 2014.

GEHLBACH, S. M.; ALVAREZ, R. E. Digital ultrasound imaging techniques using vector sampling and raster line reconstruction. *Ultrasonic Imaging*, Thousand Oaks, v. 3, n. 1, p. 83–107, 1981.

GHOSH, T.; KUNDU, T.; KARPUR, P. Efficient use of Lamb modes for detecting defects in large plates. *Ultrasonics*, Surrey, v. 36, n. 7, p. 791–801, 1998.

GIURGIUTIU, V. Tuned Lamb-wave excitation and detection with piezoelectric wafer active sensors for Structural Health Monitoring. *Journal of intelligent material systems and structures*, Lancaster, v. 16, n. 4, p. 291–305, 2005.

GÓMEZ-ULLATE, Y. *Estudio de sistemas ultrasónicos basados en multitransductores para la detección de defectos en estructuras tipo placa*. 2007. 178 f. Thesis (Doctorate in Mechanical and Manufacturing Engineering) - Escuela Técnica Superior de Ingenieros Industriales, Universidad Politécnica de Madrid, Madrid, 2007.

GRAFF, K. F. *Wave motions in solids*. [S.l.]: Dover Publications, 1975. 688 p.

GRONDEL, S.; PAGET, C.; DELEBARRE, C.; ASSAAD, J.; ; LEVIN, K. Design of optimal configuration for generating A0 Lamb mode in a composite plate using piezoceramic transducers. *Journal of the Acoustical Society of America*, Melville, v. 112, n. 1, p. 84–90, 2002.

GUO, N.; CAWLEY, P. Lamb wave reflection for the quick nondestructive evaluation of large composite laminates. *Materials Evaluation*, Evanston, v. 52, n. 3, p. 404–411, 1994.

GUO, Z.; ACHENBACH, J. D.; KRISHNASWAMY, S. EMAT generation and laser detection of single Lamb wave modes. *Ultrasonics*, Surrey, v. 35, n. 6, p. 423–429, 1997.

HARLEY, J. B.; MOURA, J. M. F. Decomposition of multipath Lamb waves with sparse wavenumber analysis for structural health monitoring. In: IEEE INTERNATIONAL ULTRASONICS SYMPOSIUM - IUS, 52., 2013, Prague. *Proceedings...* Prague: IEEE, 2013. p. 675–678.

HAUPT, R. L. Thinned arrays using genetic algorithms. *IEEE Transactions on Antennas and Propagation*, New York, v. 42, n. 7, p. 993–999, 1994.

HENDRICKS, W. J. The totally random versus the bin approach for random arrays. *IEEE Transactions on Antennas and Propagation*, New York, v. 39, n. 12, p. 1757–1762, 1991.

HIGUTI, R. T.; MARTÍNEZ-GRAULLERA, O.; MARTÍN, C. J.; OCTAVIO, A.; ELVIRA, L.; ESPINOSA, F. M. de. Damage characterization using guided-wave linear arrays and image compounding techniques. *IEEE Transactions on Ultrasonics, Ferroelectrics and Frequency Control*, New York, v. 57, n. 9, p. 1985–1995, 2010.

HOCTOR, R. T.; KASSAM, S. A. The unifying role of the coarray in aperture synthesis for coherent and incoherent imaging. *Proceedings of the IEEE*, New York, v. 78, n. 4, p. 735–752, 1990.

HOLLMAN, K.; RIGBY, K.; O'DONNELL, M. Coherence factor of speckle from a multi-row probe. In: IEEE ULTRASONICS SYMPOSIUM, 38., 1999, Caesars Tahoe . *Proceedings...* Caesars Tahoe: IEEE, 1999. v. 2, p. 1257–1260.

HOLM, S.; ELGETUN, B.; DAHL, G. Properties of the beampattern of weight- and layout-optimized sparse arrays. *IEEE Transactions on Ultrasonics, Ferroelectrics and Frequency Control*, New York, v. 44, n. 5, p. 983–991, 1997.

HOLMES, C.; DRINKWATER, B. W.; WILCOX, P. D. Post-processing of the full matrix of ultrasonic transmit-receive array data for non-destructive evaluation. *NDT&E International*, London, v. 38, n. 8, p. 701–711, 2005.

JENSEN, J. A.; NIKOLOV, S. I.; GAMMELMARK, K. L.; PEDERSEN, M. H. Synthetic aperture ultrasound imaging. *Ultrasonics*, Surrey, v. 44, n. 1, p. e5–e15, 2006.

KARAMAN, M.; LI, L. P.-C.; O'DONNELL, M. Synthetic aperture imaging for small scale systems. *IEEE Transactions on Ultrasonics, Ferroelectrics and Frequency Control*, New York, v. 42, n. 3, p. 429–442, 1995.

KINO, G. S. *Acoustic waves: devices, imaging, and analog signal processing*. [S.l.]: Prentice-Hall, 1987. 601 p.

KONSTANTINIDIS, G.; DRINKWATER, B. W.; WILCOX, P. D. The temperature stability of guided wave structural health monitoring systems. *Smart Materials and Structures*, New York, v. 15, n. 4, p. 967–976, 2006.

KONSTANTINIDIS, G.; WILCOX, P. D.; DRINKWATER, B. W. An investigation into the temperature stability of a guided wave Structural Health Monitoring system using permanently attached sensors. *IEEE Transactions on Ultrasonics, Ferroelectrics and Frequency Control*, New York, v. 7, n. 5, p. 905–912, 2007.

LAMB, H. On waves in an elastic plate. *Proceedings of the Royal Society of London. Series A.*, London, v. 93, n. 648, p. 114–128, 1917.

LEVINE, R. M.; MICHAELS, J. E. Model-based imaging of damage with Lamb waves via sparse reconstruction. *Journal of the Acoustical Society of America*, Melville, v. 133, n. 3, p. 1525–1534, 2013.

LEVINE, R. M.; MICHAELS, J. E. Block-sparse reconstruction and imaging for lamb wave structural health monitoring. *IEEE Transactions on Ultrasonics, Ferroelectrics and Frequency Control*, New York, v. 61, n. 6, p. 1006–1015, 2014.

LI, C.; PAIN, D.; DRINKWATER, B. W.; WILCOX, P. D. Imaging composite material using ultrasonic arrays. *NDT&E International*, London, v. 53, n. 1, p. 8–17, 2013.

LI, F.; PENG, H.; MENG, G. Quantitative damage image construction in plate structures using a circular PZT array and lamb waves. *Sensors and Actuators A: Physical*, London, v. 214, n. 1, p. 66–73, 2014.

LOCKWOOD, G. R.; FOSTER, F. S. Optimizing the radiation pattern of sparse periodic two-dimensional arrays. *IEEE Transactions on Ultrasonics, Ferroelectrics and Frequency Control*, New York, v. 43, n. 1, p. 15–19, 1996.

LOCKWOOD, G. R.; LI, P.-C.; O'DONNELL, M.; FOSTER, F. S. Optimizing the radiation pattern of sparse periodic linear arrays. *IEEE Transactions on Ultrasonics, Ferroelectrics and Frequency Control*, New York, v. 43, n. 1, p. 7–14, 1996.

LOWE, M. J. S.; ALLEYNE, D. N.; CAWLEY, P. Defect detection in pipes using guided waves. *Ultrasonics*, Surrey, v. 36, n. 1-5, p. 147–154, 1998.

MARTIN, C. J.; MARTÍNEZ, O.; ULLATE, L. G.; OCTAVIO, A. Reduction of grating lobes in SAFT images. In: IEEE INTERNATIONAL ULTRASONICS SYMPOSIUM - IUS, 47., 2008, Beijing. *Proceedings...* Beijing: IEEE, 2008. p. 721–724.

MARTÍNEZ-GRAULLERA, O.; MARTÍN-ARGUEDAS, C. J.; GODOY, G.; ULLATE, L. G. 2D array design based on Fermat spiral for ultrasound imaging. *Ultrasonics*, Surrey, v. 50, n. 2, p. 280–9, 2010.

- MARTÍNEZ-GRAULLERA, O.; ROMERO-LAORDEN, D.; MARTÍN-ARGUEDAS, C. J.; IBAÑEZ, A.; ULLATE, L. G. A new beamforming process based on the phase dispersion analysis. In: INTERNATIONAL CONGRESS ON ULTRASONICS - ICU, 7., 2011, Poland. *Proceedings...* Poland: AIP Publishing, 2011. v. 1433, p. 185–188.
- MARTÍNEZ, O.; AKHNAK, L. G. U. M.; ESPINOSA, F. M. de. A small 2D ultrasonic array for NDT applications. *NDT&E International*, London, v. 36, p. 57–63, 2003.
- MAYSENHOLDER, W. Analytical determination of the group velocity of an arbitrary Lamb wave from its phase velocity. *Acustica*, Stuttgart, v. 77, n. 4, p. 208, 1992.
- MICHAELS, J. E. Detection, localization and characterization of damage in plates with an in situ array of spatially distributed ultrasonic sensors. *Smart Materials and Structures*, New York, v. 17, n. 3, p. 15, 2008.
- MICHAELS, J. E.; DAWSON, A. J.; MICHAELS, T. E.; RUZZENE, M. Approaches to hybrid SHM and NDE of composite aerospace structures. In: HEALTH MONITORING OF STRUCTURAL AND BIOLOGICAL SYSTEMS, 14., 2014, San Diego. *Proceedings...* San Diego: SPIE, 2014. v. 9064, p. 9.
- MICHAELS, J. E.; LEE, S. J.; CROXFORD, A. J.; WILCOX, P. D. Chirp excitation of ultrasonic guided waves. *Ultrasonics*, Surrey, v. 53, n. 1, p. 265–270, 2013.
- MICHAELS, J. E.; LEE, S. J.; HALL, J. S.; MICHAELS, T. E. Multi-mode and multi-frequency guided wave imaging via chirp excitations. In: HEALTH MONITORING OF STRUCTURAL AND BIOLOGICAL SYSTEMS, 11., 2011, San Diego. *Proceedings...* San Diego: SPIE, 2011. v. 7984, p. 11.
- MICHAELS, J. E.; MICHAELS, T. E. Guided wave signal processing and image fusion for in situ damage localization in plates. *Wave Motion*, New York, v. 44, n. 6, p. 482–492, 2007.
- NIETHAMMER, M.; JACOBS, L. J.; QU, J.; JARZYNSKI, J. Time-frequency representations of Lamb waves. *Journal of the Acoustical Society of America*, Melville, v. 109, n. 5, p. 1841–1847, 2001.
- NORTON, S. J. Annular array imaging with full-aperture resolution. *Journal of the Acoustical Society of America*, Melville, v. 92, n. 6, p. 3202–3206, 1992.
- OPPENHEIM, A. V.; LIM, J. S. The importance of phase in signals. *Proceedings of the IEEE*, New York, v. 69, n. 5, p. 529 – 541, may 1981.
- OPPENHEIM, A. V.; SCHAFER, R. W.; BUCK, J. R. *Discrete-time signal processing*. New Jersey 1999. 870 p.
- OSTACHOWICZ, W.; KUDELA, P.; MALINOWSKI, P.; WANDOWSKI, T. Damage localisation in plate-like structures based on PZT sensors. *Mechanical Systems and Signal Processing*, London, v. 23, n. 6, p. 1805–1829, 2009.
- PUTKIS, O.; CROXFORD, A. J. Continuous baseline growth and monitoring for guided wave SHM. *Smart Materials and Structures*, New York, v. 22, n. 5, p. 10, 2013.
- QIANG, W.; SHENFANG, Y. Baseline-free imaging method based on new PZT sensor arrangements. *Journal of Intelligent Material Systems and Structures*, Lancaster, v. 20, n. 14, p. 1633–1673, 2009.

- RAYLEIGH, L. On waves propagated along the plane surfaces of an elastic solid. *Proc. London Math. Soc.*, London, v. 17, n. 1, p. 4–11, 1885.
- ROSE, J. L. *Ultrasonic waves in solid media*. [S.l.]: Cambridge University Press, 1999. 454 p.
- ROSE, J. L. Guided wave nuances for ultrasonic nondestructive evaluation. *IEEE Transactions on Ultrasonics, Ferroelectrics and Frequency Control*, New York, v. 47, n. 3, p. 575–583, 2000.
- RUSSELL, D. A.; TITLOW, J. P.; BEMMEN, Y.-J. Acoustic monopoles, dipoles, and quadrupoles: An experiment revisited. *American Journal of Physics*, St. Louis, v. 67, n. 8, p. 660–664, 1999.
- SANTONI, G. B.; YU, L.; XU, B.; GIURGITU, V. Lamb wave-mode tuning of piezoelectric wafer active sensors for structural health monitoring. *Transactions of the ASME*, New York, v. 129, n. 6, p. 752–762, 2007.
- SCHMITT, M.; OLFERT, S.; RAUTENBERG, J.; LINDNER, G.; HENNING, B.; REINDL, L. M. Multi reflection of Lamb wave emission in an acoustic waveguide sensor. *Sensors*, Basel, v. 13, n. 3, p. 2777–2785, 2013.
- SCHMITZ, V.; CHAKHLOV, S.; MULLER, W. Experiences with synthetic aperture focusing technique in the field. *Ultrasonics*, Surrey, v. 38, n. 1-8, p. 731–738, 2000.
- SCHWARTZ, J.; STEINBERG, B. D. Ultraparse, ultrawideband arrays. *IEEE Transactions on Ultrasonics, Ferroelectrics and Frequency Control*, New York, v. 45, n. 2, p. 376–393, 1998.
- SEO, C. H.; YEN, J. T. A 256 x 256 2-D array transducer with row-column addressing for 3-D rectilinear imaging. *IEEE Transactions on Ultrasonics, Ferroelectrics and Frequency Control*, New York, v. 56, n. 4, p. 837–847, 2009.
- SHARIF-KHODAEI, Z.; ALIABADI, M. H. Assessment of delay-and-sum algorithms for damage detection in aluminium and composite plates. *Smart Materials and Structures*, New York, v. 23, n. 7, p. 20, 2014.
- SHELKE, A.; KUNDU, T.; AMJAD, U.; HAHN, K.; GRILL, W. Mode-selective excitation and detection of ultrasonic guided waves for delamination detection in laminated aluminum plates. *IEEE Transactions on Ultrasonics, Ferroelectrics and Frequency Control*, New York, v. 58, n. 3, p. 567–577, 2011.
- SHERWIN, C. W.; RUINA, J. P.; RAWCLIFFE, R. D. Some early developments in synthetic aperture radar systems. *IRE Transactions on Military Electronics*, New York, v. MIL-6, n. 2, p. 111–115, april 1962.
- SKOLNIK, M. I.; NEMHAUSER, G.; SHERMAN, J. Dynamic programming applied to unequally spaced arrays. *IEEE Transactions on Antennas and Propagation*, New York, v. 12, n. 1, p. 35–43, 1964.
- STANKWITZ, H. C.; DALLAIRE, R. J.; FIENUP, J. R. Nonlinear apodization for sidelobe control in SAR imagery. *IEEE Transactions on Aerospace and Electronic Systems*, New York, v. 31, n. 1, p. 267–279, 1995.

STASZEWSKI, W. J.; MAHZAN, S.; TRAYNOR, R. Health monitoring of aerospace composite structures - active and passive approach. *Composites Science and Technology*, Barking, v. 69, n. 11-12, p. 1678–1685, 2009.

STEINBERG, B. D. *Principles of aperture and array system design: including random and adaptive arrays*. [S.l.]: Wiley, 1976. 356 p. (A Wiley-Interscience publication).

STEPINSKI, T.; AMBROZINSKI, L.; UHL, T. Designing 2D arrays for SHM of planar structures: a review. In: NONDESTRUCTIVE CHARACTERIZATION FOR COMPOSITE MATERIALS, AEROSPACE ENGINEERING, CIVIL INFRASTRUCTURE, AND HOMELAND SECURITY, 7., 2013, San Diego. *Proceedings...* San Diego: SPIE, 2013. v. 8694, p. 12.

SU, Z.; CHENG, L.; WANG, X.; YU, L.; ZHOU, C. Predicting delamination of composite laminates using an imaging approach. *Smart Materials and Structures*, New York, v. 18, n. 7, p. 8, 2009.

SU, Z.; YE, L. *Identification of Damage Using Lamb Waves: from fundamentals to applications*. [S.l.]: Springer London, 2009. 356 p.

SU, Z.; YE, L.; LU, Y. Guided Lamb waves for identification of damage in composite structures: a review. *Journal of Sound and Vibration*, London, v. 295, n. 3-5, p. 753–780, 2006.

TAMANO, S.; KOBAYASHI, T.; SANO, S.; HARA, K.; SAKANO, J.; AZUMA, T. 3D ultrasound imaging system using fresnel ring array & high voltage multiplexer IC. In: IEEE ULTRASONICS SYMPOSIUM, 43., 2004, Taipei. *Proceedings...* Taipei: IEEE, 2004. v. 1, p. 782–785.

THOMSON, R. N. Transverse and longitudinal resolution of the synthetic aperture focusing technique. *Ultrasonics*, Surrey, v. 22, n. 1, p. 9–15, 1984.

TSUDA, H.; TOYAMA, N.; URABE, K.; TAKATSUBO, J. Impact damage detection in CFRP using fiber Bragg gratings. *Smart Materials and Structures*, New York, v. 13, n. 4, p. 719–724, 2004.

ULLATE, L. G.; GODOY, G.; MARTÍNEZ, O.; SANCHEZ, T. Beam steering with segmented annular arrays. *IEEE Transactions on Ultrasonics, Ferroelectrics and Frequency Control*, New York, v. 53, n. 10, p. 1944–1954, 2006.

VALLE, C.; LITTLES JR., J. W. Flaw localization using the reassigned spectrogram on laser-generated and detected Lamb modes. *Ultrasonics*, Surrey, v. 39, n. 8, p. 535–542, 2002.

VELICHKO, A.; WILCOX, P. D. Guided wave arrays for high resolution inspection. *Journal of the Acoustical Society of America*, Melville, v. 123, n. 1, p. 186–196, 2008.

VIKTOROV, I. A. *Rayleigh and Lamb waves: physical theory and applications*. [S.l.]: Plenum Press, 1967. 154 p. (Ultrasonic Technology).

WEIDLINGER ASSOCIATES INC. *PZFlex - user manual*. Mountain View: [s. n.], 2009. 200 p.

WILCOX, P. D. A rapid signal processing technique to remove the effect of dispersion from guided wave signals. *IEEE Transactions on Ultrasonics, Ferroelectrics and Frequency Control*, New York, v. 50, n. 4, p. 419–427, 2003a.

- WILCOX, P. D. Omni-directional guided wave transducer arrays for the rapid inspection of large areas of plate structures. *IEEE Transactions on Ultrasonics, Ferroelectrics and Frequency Control*, New York, v. 50, n. 6, p. 699–709, 2003b.
- WILCOX, P. D.; CAWLEY, P. The effect of dispersion on long-range inspection using ultrasonic guided waves. *NDT&E International*, London, v. 39, n. 1, p. 1–9, 2001.
- WORDEN, K.; DULIEU-BARTON, J. M. An overview of intelligent fault detection in systems and structures. *Structural Health Monitoring*, London, v. 3, n. 1, p. 85–98, 2004.
- WU, J.; ZHU, Z. The propagation of Lamb waves in a plate bordered with layers of a liquid. *Journal of the Acoustical Society of America*, Melville, v. 91, n. 2, p. 861–867, 1992.
- XU, B.; YU, L.; GIURGIUTIU, V. Lamb wave dispersion compensation in piezoelectric wafer active sensor phased-array applications. In: HEALTH MONITORING OF STRUCTURAL AND BIOLOGICAL SYSTEMS, 9., 2009, San Diego. *Proceedings...* San Diego: SPIE, 2009. v. 7295, p. 12.
- YLITALO, J. T.; ERMERT, H. Ultrasound synthetic aperture imaging: monostatic approach. *IEEE Transactions on Ultrasonics, Ferroelectrics and Frequency Control*, New York, v. 41, n. 3, p. 333–339, 1994.
- YU, L.; GIURGIUTIU, V. Multi-mode damage detection methods with piezoelectric wafer active sensors. *Journal of Intelligent Material Systems and Structures*, Lancaster, v. 20, n. 11, p. 1329–1341, 2009.
- YU, L.; GIURGIUTIU, V. In situ 2-D piezoelectric wafer active sensors arrays for guided wave damage detection. *Ultrasonics*, Surrey, v. 48, n. 2, p. 117–134, 2008.
- ZHAO, X.; GAO, H.; ZHANG, G.; AYHAN, B.; YAN, F.; KWAN, C.; ROSE, J. L. Active health monitoring of an aircraft wing with embedded piezoelectric sensor/actuator network: I. defect detection, localization and growth monitoring. *Smart Materials and Structures*, New York, v. 16, n. 4, p. 1208, 2007.
- ZHOU, G.; SIM, L. M. Damage detection and assessment in fibre-reinforced composite structures with embedded fibre optic sensors - review. *Smart Materials and Structures*, New York, v. 11, n. 6, p. 925–939, 2002.